CHARACTERIZATION OF QUANTUM WELL INFRARED PHOTODETECTORS BY ANALYSIS OF NOISE SPECTRAL DENSITY

By

LISA KORE

A DISSERTATION PRESENTED TO THE GRADUATE SCHOOL
OF THE UNIVERSITY OF FLORIDA IN PARTIAL FULFILLMENT
OF THE REQUIREMENTS FOR THE DEGREE OF
DOCTOR OF PHILOSOPHY

UNIVERSITY OF FLORIDA

2003

This work is dedicated to all the women who faced the struggle, as well as those that continue to do so, so that the women that follow may spend their days seeking knowledge rather than recognition.

ACKNOWLEDGMENTS

I would like to extend my appreciation to the women in my life who supported me during the long haul, my graduate advisor, Gijs Bosman, who stuck with me through my leisurely journey, and most especially Nancy Coleman for always believing in me.

This research would not have been possible without the generously provided time and materials given by Dr. Sheng Li and his graduate students, and the other noise lab members.

I would also like to express my appreciation for the Graduate Minority Fellowship, the National Science Foundation Graduate Minority Fellowship, and the GE Fellowship that have allowed me to focus all of my energy on my education.

This material is based upon work supported under a National Science Foundation Graduate Fellowship. Any opinions, findings, conclusions or recommendations expressed in this publication are those of the author and do not necessarily reflect the views of the National Science Foundation.

TABLE OF CONTENTS

LIST OF TABLES

LIST OF FIGURES

Abstract of Dissertation Presented to the Graduate School
of the University of Florida in Partial Fulfillment of the
Requirements for the Degree of Doctor of Philosophy

CHARACTERIZATION OF QUANTUM WELL INFRARED PHOTODETECTORS
BY ANALYSIS OF NOISE SPECTRAL DENSITY

By

Lisa Kore

May 2003

Chair: Gijs Bosman
Major Department: Electrical and Computer Engineering

Three quantum well infrared photodetectors are characterized utilizing noise spectral density and current-voltage measurements taken at a variety of temperatures and biases. Though all devices were fabricated using the GaAs/InGaAs material system, each has a unique morphology. D1 had three different quantum wells per period and 20 periods. D2 had one type of quantum well and 10 periods. D3 had one type of quantum well, 5 periods, and asymmetric barriers.

Measurement temperatures for D1 ranged between 80 K and 180 K with bias values for each temperature between zero and 35 μA. For D2 and D3 measurement temperatures ranged between 80 K and 125 K with bias values for each temperature between zero and 10 mA.

Utilizing models for thermionic emission current and Fowler-Nordheim tunneling current the current-voltage characteristic of each device was compared with the theory.

The thermionic emission model did well for all devices at low bias. The tunneling model did well for all devices at high bias. In the middle range of biases D1 was underestimated by the models, D3 was overestimated by the models, and D2 was modeled well by a sum of the two models. In each case, the energy band diagram contained clues that could explain the behavior.

Noise spectral density data were obtained for D1 in the range of frequencies between 4 Hz and 1 kHz, for the other two devices in the range between 25 Hz and 100 kHz. Each device had excess low frequency noise that was *1/f*-like in nature. For D1 it was attributed to random telegraph signal noise and analyzed with the result of extracting both the electron mobility and the number of charge carriers. No other noise analysis was performed on D1 due to the frequency range.

D2 and D3 exhibited excess high frequency noise in addition to the excess low frequency noise. This led to noise analysis that included generation-recombination noise and mobility fluctuation noise. The former was accomplished using an existing model but was found to be unsuitable, unless modified, for D3. For D2 the model was predictive. The mobility fluctuation model for low frequency noise was applied to both devices with inconclusive results. For D2 the extracted Hooge parameter was low but reasonable. For D3 the extracted Hooge parameter could not be reconciled with the expected transport parameters. This is likely a result of not enough temperature data points for either device.

CHAPTER 1
INTRODUCTION

The impetus behind this research is to take a negative aspect of a device, noise, and produce useful information from it. Research on device noise can be utilized variously. One aspect is that of determining the performance characteristics, which are limited by the noise in the device, e.g., the smallest signal detectable. Another aspect is to use the noise characteristics to determine physical and/or transport parameters of the device; e.g., a lorentzian noise spectrum gives a characteristic time for a trap level (defect) in the device.

The motivation for quantum well infrared photodetector (QWIP) noise research has largely been its effect on detectivity. Little use has been made of noise in QWIPs to determine device transport parameters or physical behavior. This research includes the use of device noise to show the effect that a small number of defects have on device performance, the extraction of transport parameters, as well as developing some insight into the physics of QWIPs.

Noise

The study of noise is not a new phenomenon and has proven useful in both determining and confirming device physics for several types of semiconductor devices. As well, results from noise characterization have allowed optimization of device morphology, which reduces the effects of noise for that device, i.e., improves device performance.

Noise in semiconductors may be described by frequency dependence, current dependence, underlying physical cause, or the name of a researcher who has derived a theory to explain it. In at least one instance it is described by its time domain behavior. However noise is described, the fundamental principle is that it is generated by random events. This is particularly useful since an understanding of the physics of semiconductors has its basis in probability, random variables, and stochastic processes. The various types of noise that prove pertinent to this study will be introduced and elucidated in conjunction with the presentation of the data.

The extent to which noise affects device behavior is determined by a confluence of variables such as temperature, bias, energy configuration, and frequency of operation. The goal is usually to find the combination of factors that will reduce the noise to its physical limit and hope that the conditions are inexpensive and repeatable. One of the overriding negative aspects of QWIPs is the operating temperature. One goal of this research is to increase the understanding of QWIP behavior such that room temperature operation may be possible in the not too distant future.

Quantum Well Infrared Photodetectors

Quantum well infrared photodetectors (QWIPs) are a category of devices that detect various wavelengths in the infrared regime. They can be fabricated to a specific wavelength or to a range of wavelengths. GaAs and its ternary and quaternary compounds form a material system that provides extensive latitude in the design of QWIPs to meet the needs of a wide variety of applications. They operate individually or in a focal plane array. Their strengths lie in focal plane array applications [1].

QWIPs are heterostructure devices that utilize quantum confinement in one dimension to enable fabrication of various wavelength absorption. This is accomplished

by layering barriers and quantum wells in series, shown stylistically in Figure 1. The thickness and composition of the barriers determine factors such as dark current mechanism and magnitude and band gap offsets. The thickness, composition and doping of the wells determine available energy states and therefore absorption wavelength.

The two layers are distinguished by their different composition, with the barrier layer having a wider band gap than the well. In addition, the barriers are typically undoped while the wells are heavily doped. The conduction band and valence band offsets confine the electron gas in the growth direction thus creating a quantum well. The well has discrete energy levels available for occupation by electrons or holes. For the purposes of this research, only the conduction band and electrons will be considered since the devices studied are n-type.

Typically, the first energy level (ground state) in the quantum well is at some energy depth below the barrier conduction band but above the quantum well conduction band, and the second energy level is at or above the barrier conduction band. These configurations are bound-to-quasi-bound or bound-to-continuum, respectively. Figure 2 shows a stylistic representation of a bound-to-continuum QWIP. In a bound-to-quasi-bound configuration E_1 would be slightly lower than the barrier conduction band. In some instances a mini-band is formed between the well's ground state and the barrier conduction band, these are called bound-to-mini-band devices and is stylistically represented in Figure 3. Two devices used in this research are classified as bound-to-continuum the third is more like bound-to-mini-band though not 100 percent.

The difference in energy between the ground and first states (or continuum) dictates the energy of photons that will be absorbed by the device. The nature of the material

system allows for latitude in designing the target absorption wavelength. In addition, including more than one kind of well in a single device could target a range of wavelengths. By grouping the energy depths closely, absorption will be across a wide band of wavelengths instead of a narrow one.

QWIPs are usually operated in the photoconductive regime. A bias is applied to the device that creates an electric field that sweeps excited carriers to one contact. It is generally assumed that when one carrier exits through one contact, another carrier enters through the opposite contact; i.e., contacts are ohmic, with no time delay. This assumption will be followed in this work though there is some evidence to the contrary [2].

Carriers are generated thermally or photonically. Thermal generation is a direct consequence of lattice temperature, dictated by ambient temperature and local heating due to scattering events. Photonic generation is accomplished by directing photons of the requisite wavelength onto the device. For the case of n-type QWIPs, some light-bending scheme must be employed due to quantum selection rules whereby the light must be perpendicular to the plane of the quantum well in order to be absorbed [3].

Of the four parameters used to characterize the performance of optical detectors [4], QWIPs are evaluated primarily by responsivity and detectivity. Responsivity is a measure of useful radiation absorption and is typically presented as a function of bias. Detectivity is a measure of how noisy the device is.

The figure of merit used to compare photodetectors is detectivity, D^*, and is defined as the root-mean-square (RMS) signal-to-noise ratio in a 1 Hz bandwidth per unit RMS incident radiation per square root of detector area [4].

$$D^* = \frac{i_s}{i_n}\frac{\sqrt{A\Delta f}}{P} \tag{1.1}$$

where i_s is signal current, i_n is noise current, A is device area, Δf is bandwidth, and P is incident power. This work explores other figures of merit that may influence D^*, albeit indirectly.

The nearest competitor to QWIPs is mercury cadmium telluride (HCT) photodetectors. These are photoconductive devices that are not suitable for array applications as they are expensive and non-uniform across arrays. As early as 1988 QWIPs were shown to have a competitive D^* and the promise of focal plane array fabrication [5]. Kinch and Yariv [6] specifically compared the performance of QWIPs with HCT detectors. Admitting that the QWIPs tested were not optimized, they concluded that point-to-point comparison favored HCT detectors with D^* being three orders of magnitude better at both cut-off wavelengths tested. However, they did not speak to the cost differences or the ability of QWIPs to be made into uniform focal plane arrays. QWIP superiority in focal plane array applications is discussed by Levine et al. [7] and later in more detail by Andrews and Miller [8]. Some of the points raised include mature materials growth and processing technology, greater uniformity and larger substrate, monolithic integration, thermal stability, radiation hardness, and inherent high speed. Choi et al. [9] discussed the performance improvements seen in QWIPs. D^* for their device was only one order of magnitude lower than an HCT device at the same temperature. One of the previous negatives associated with QWIPs was that performance similar to an HCT device required operating at significantly lower temperatures.

In the main, the noise discussed in the literature has been that caused by dark current via its effect on D^*. The role that dark current plays on QWIP performance is

adversarial. Dark current is caused by mechanisms that are not controlled by incident radiation. Therefore, its effects are negative with respect to device performance. In other words, since what is being measured is the amount of incident radiation in a particular wavelength range, any random current that is not a direct consequence of that radiation is noise and may swamp the radiation generated signal. It is thus a good idea to determine the causes of the dark current so that their effects can be corrected in the readout circuitry and/or the causes can be alleviated by design.

Dark current is generated by one or more mechanisms. They include thermionic emission, sequential resonant tunneling, and phonon assisted tunneling [10, 11]. An obvious method of reducing the currents generated by thermionic emission is reduction of lattice temperature. This is primarily achieved by cooling the device during operation and is an added expense and a potential area of malfunction. Depending on temperature, thermionic emission may become a fundamental limit to device performance. At low enough temperatures to reduce thermionic emission, another mechanism takes over. Sequential resonant tunneling may be controlled by ensuring the barrier widths are thick enough to reduce the statistical probability of tunneling to near zero.

Improvements in dark current, and therefore responsivity, were achieved early on by increasing the thickness and height of the barriers. Early devices had a tunneling photocurrent. In other words, there were two energy states in the quantum well with the first excited state being far enough below the barrier conduction band that photo-excited carriers had to tunnel through the barrier tip developed due to bias. At temperatures below about 100 K, the dark current was found to be dominated by sequential tunneling. Above about 130 K thermionic emission dominated the dark current. From 100 K to 130

K phonon assisted tunneling contributed strongly as well [10]. Later, Levine et al. [7] also increased the barrier widths as a deterrent to the tunneling component of dark current. They achieved an order of magnitude decrease in tunneling current with about a 200 Å increase in barrier width (from ~300 Å to ~500 Å).

Another method used to reduce dark current was to push the first excited energy state of the quantum well into the continuum. This meant the photocurrent no longer had to tunnel through the barrier allowing the barrier widths to be increased further. That barrier width increase ensured a further decrease in dark current with a concurrent increase in detectivity [5].

Pelvé et al. [11] showed and modeled the dark current dependence on thermionic emission and tunneling. They found that thermionic emission dominated at low bias and higher temperatures and that tunneling dominated at high bias and lower temperatures.

Brennan and Wang [12] developed a two-dimensional model for dark currents. They modeled the currents due to thermionic emission as temperature dependent and determined that for contributions below about 10^{-14} A/cm^2 the device must be operated at or below 77 K. They modeled the tunneling current as electric field dependent and determined that for contributions below about 10^{-14} A/cm^2 the field should be at or below 30 kV/cm. Optimal operation is thus constrained in both temperature and bias.

A dark current model was developed by Andrews and Miller [8] that was compared with dark current measurements taken as a function of barrier width and electron density in the well. Qualitative agreement was obtained for the expectation of a decrease in dark current with an increase in barrier width and an increase in dark current with increased well doping. Some of the assumptions made may prove disheartening later such as

constant electric field, neglecting complications due to how the carriers are replenished in the wells and charge transfer at the emitter contact. In addition, a low figure was used for mobility, 1000 cm^2/Vs, and an arbitrary value for saturation velocity.

Williams et al. [13] added a component of defect assisted tunneling to the dark current that describes the underestimation of dark current at low bias and low temperature. In 1993, Liu et al. [14] evaluated several models and supported the model where emission current is only a portion of the total dark current which they felt was the most physically plausible. As can be seen, dark current and its effects on detectivity are fairly well characterized.

Synopsis

Chapter 2 begins with a description of the devices for which measurements were taken. Included are material parameters that were specified by the designers as well as whatever had to be determined from related material systems. Chapter 3 details the simulations that were carried out. These simulations allowed further insight into the electron transport picture as well as providing pertinent system parameters that could be used for subsequent analysis and evaluation. Chapter 4 details the current-voltage (IV) characteristics for each device under study. Comparisons are made between measured data and physical models gleaned from the literature with a favorable outcome.

Chapter 5 begins the foray into noise characterization for these devices by outlining types of noise and their manifestations. Then the measured noise data are presented with some preliminary observations about the possible information contained by the data. In chapter 6 the discussion focuses on a type of noise termed generation-recombination (GR) noise. Two types of coupling mechanisms are derived and then compared with the data with potentially conflicting results. Chapter 7 delves into a category of noise termed

flicker noise. The focus is on theory that deems the source to be mobility fluctuations. Two figures of merit are obtained that speak to how the noise compares with other devices and where the excess noise corner frequency is for these devices.

In chapter 8 some key device transport parameters are obtained from random telegraph signal (RTS) noise in one of the devices. Finally, chapter 9 contains conclusions drawn about the devices and the research performed on them as well as any comparisons able to be made among the devices. Included are some suggestions for future research.

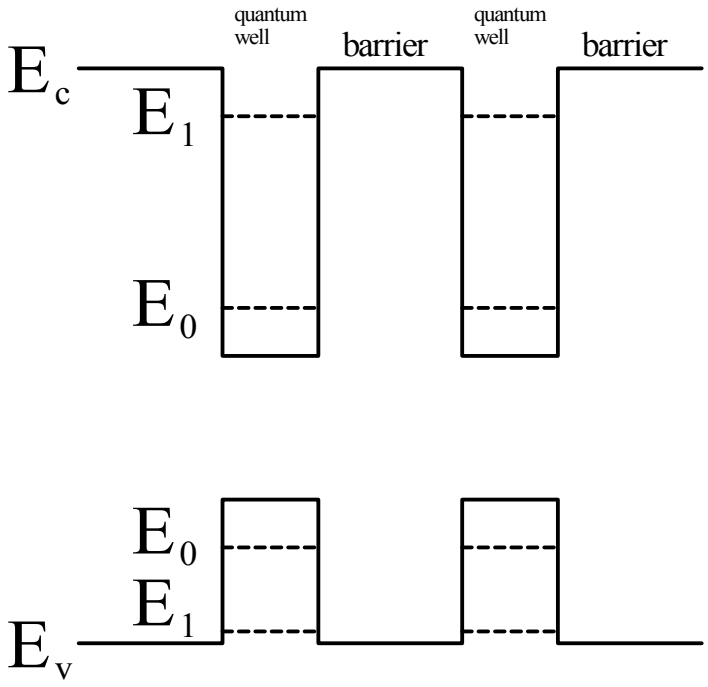

Figure 1 Stylized representation of a bound-to-bound QWIP, including the valence band.

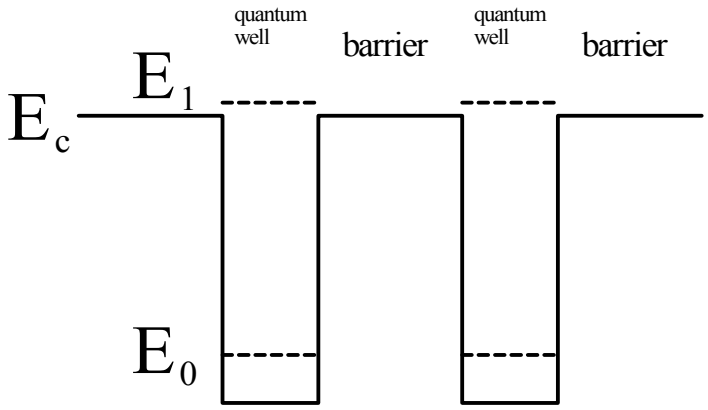

Figure 2 Stylized representation of a bound-to-continuum QWIP, conduction band only.

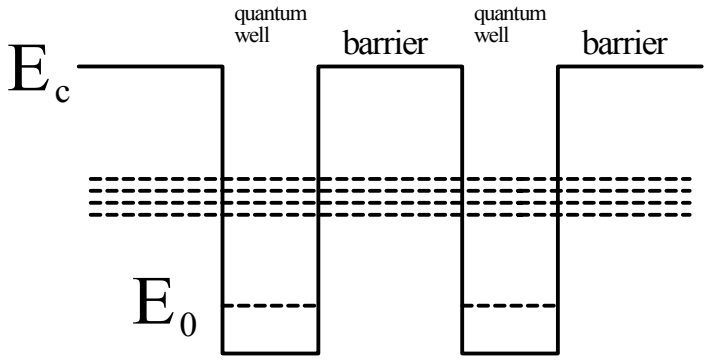

Figure 3 Stylized representation of a bound-to-mini-band QWIP, conduction band only.

CHAPTER 2
DEVICES

While all of the devices measured are QWIPs, their characteristics differentiate each one within the overall classification. Each was designed with different target specifications. The similarities allow generalization and the differences allow exploration of design related characteristics.

Descriptions

Device I

The first device measured [15], designated D1, is comprised of 20 periods with 3 independent quantum wells within each period separated by identical barriers. A single period of D1 is represented pictorially in Figure 4 with the energy relationships shown in Figure 5. The asymmetry of the device predicates care in description. The deepest well was arbitrarily labeled as well 1 (W1), the middle-depth well as well 2 (W2) and the shallowest well as well 3 (W3). Each quantum well is composed of $In_xGa_{1-x}As$ with x=0.2, x=0.15, and x=0.1 respectively for W1, W2, and W3. Each is doped N-type with silicon at 7×10^{17} cm^{-3}. The growth widths are 65 Å, 65 Å, and 75 Å, respectively for W1, W2, and W3. All of the barriers are composed of undoped $Al_{0.07}Ga_{0.93}As$ with a width of 450 Å. There are wide, highly doped GaAs contacts at either end of the stack. The total device length is 4.8 μm and the area is (216×216) μm^2. Table 1 shows the material parameters used for analysis and simulations for D1.

Device II

Device II (D2) consists of 10 periods of a single type of quantum well and barrier [16]. A single period of D2 is represented pictorially in Figure 6 with the energy relationships shown in Figure 7. The quantum wells are $In_{0.1}Ga_{0.9}As$ doped N-type with silicon at 8×10^{17} cm^{-3} and a growth width of 63 Å. The barriers are composed of undoped $Al_{0.1}Ga_{0.9}As$ at a width of 500 Å. The device area is (200×200) μm^2. This group of wells and barriers is actually grown as the middle portion of a three portion QWIP. Access to this device is via contacts grown between the three separate devices. These contacts are highly doped GaAs of at least 0.5 μm and are exposed using chemical etching. Table 2 shows the material parameters used for analysis and simulations for D2.

Device III

Device III (D3) consists of 5 periods of a single type of quantum well with asymmetric barriers [16]. A single period of D3 is represented pictorially in Figure 8 with the energy relationships shown in Figure 9. The quantum wells are $In_{0.15}Ga_{0.85}As$ doped N-type with silicon at 2×10^{18} cm^{-3} and are grown to 64 Å. This device is the portion of the above mentioned stack that is grown directly on the substrate. The device area is (200×200) μm^2. There are three sections to each barrier. The outer sections are composed of undoped $Al_{0.5}Ga_{0.5}As$ and are grown to 20 Å. In between these wide band-gap narrow width barriers is 460 Å of Al_xGa_{1-x} As in which the x value is linearly increased from x=0.13 to x=0.17. The side of each barrier closest to the substrate is x=0.13. Highly doped GaAs contacts of at least 0.6 μm bound each side of the device.

Table 3 shows the material parameters used for analysis and simulations for D3.

Table 1 Device I material parameters

	Barrier	Well 1	Well 2	Well 3
DEVICE I	$Al_xGa_{1-x}As$	$In_xGa_{1-x}As$		
x	0.07	0.2	0.15	0.1
m_n^*	0.0688	0.05452	0.05662	0.05873
χ (eV)	3.993	4.236	4.195	4.153
ε_r	12.7	13.23	13.14	13.06
E_g Γ (eV)	N/A	1.189	1.258	1.331
E_g L (eV)	N/A	1.489	1.558	1.631
E_g X (eV)	N/A	1.689	1.758	1.831
z (nm)	45	6.5	6.5	7.5
N_d (cm^{-3})	0	$7\cdot10^{17}$	$7\cdot10^{17}$	$7\cdot10^{17}$

Table 2 Device II material parameters

	Barrier	Well
DEVICE II	$Al_xGa_{1-x}As$	$In_xGa_{1-x}As$
x	0.1	0.1
m_n^*	0.0713	0.05873
χ (eV)	3.96	4.153
ε_r	12.62	13.06
E_g Γ (eV)	N/A	1.331
E_g L (eV)	N/A	1.631
E_g X (eV)	N/A	1.831
z (nm)	50	6.3
N_d (cm^{-3})	0	$8\cdot10^{17}$

Table 3 Device III material parameters

	Barrier 1	Barrier 2	Well
DEVICE III	$Al_xGa_{1-x}As$	$Al_xGa_{1-x}As$	$In_xGa_{1-x}As$
x	0.5	0.13-0.17	0.15
m_n^*	0.1045	0.07379-0.07711	0.05662
χ (eV)	3.57	3.927-3.883	4.195
ε_r	11.48	12.53-12.42	13.14
E_g Γ (eV)	N/A	N/A	1.258
E_g L (eV)	N/A	N/A	1.558
E_g X (eV)	N/A	N/A	1.758
z (nm)	2	46	6.4
N_d (cm^{-3})	0	0	$2\cdot10^{18}$

Experimental Set-up

The experimental design used for measurement of each device was the same and is depicted in Figure 10. Signal amplification for D1 was enhanced, as shown in Figure 11,

due to device and environmental conditions. The set-up consists of a nitrogen flow cryostat cooling system, metal-film resistor bias networks, one or two EG&G Brookdeal 5004 low-noise amplifier(s), lead-acid batteries, an HP4145A semiconductor parameter analyzer, one of two different dynamic signal analyzers, and one or two oscilloscopes.

Each device was mounted on the end of a cold finger. Thermally coated wire attached to the device allowed external electrical connection. The cold finger was enclosed to enable pump down to near vacuum conditions. Liquid nitrogen was then pressurized to drive the cold finger to the measurement temperature. A Lake Shore Cryotronics, Inc. DTC 500A temperature controller was used to enable control and measurement of the device temperature.

Once the desired temperature is achieved a DC current-voltage (IV) characteristic is obtained with the HP4145A semiconductor parameter analyzer (SCPA). The IV characteristic shows whether the device is viable and allows calculation of the dynamic resistance for that device at the measurement temperature. Then noise measurements are taken at negative bias currents ranging from zero to 10 mA for each temperature.

Bias was attained using lead acid batteries. There were two 14.3 V sources, one negative and one positive, to supply the low noise amplifier. The device bias was taken from the negative source and fed through various metal-film resistor networks to achieve the current biases for noise measurements.

An analog oscilloscope was used to ensure linearity of the amplification circuitry. For any device at any temperature or bias that random telegraph signal (RTS) was observed, an HP54645A digital oscilloscope was used to obtain data in the time domain, with 50 μs resolution in 50 s windows, for later evaluation.

Device I

The experimental set-up for D1 incorporated an enhanced amplification system within the copper box in place of the single low-noise amplifier. A block diagram representation is shown in Figure 11. The output of the first amplifier entered a 30 kHz cut-off low-pass filter which was resistor matched to a microwave attenuator whose output fed the second low-noise amplifier. Noise spectral density data were collected with an HP3582A spectrum analyzer. Analysis of the noise spectral density data was carried out for values between 4 Hz and 1 kHz. Noise spectral densities at higher frequencies could not be recorded due to limitations of the spectrum analyzer and the frequency response of the amplification/attenuation circuitry. In addition, the cold finger and its surrounding chamber were supported by a metal cage which may have caused high magnitude 60 Hz and harmonics interference. All data collection was computer controlled via GPIB protocol.

The device was negatively current biased at five different levels, 0, 1.5, 4.5, 13.5, and 35.5 μA for each of eight temperatures, 82.0, 91.7, 104.2, 121.2, 144.6, 179.8, 237.4 and 298 K.

Device II

Prior to measurements on D2 or D3, the metal cage was replaced by a wooden one to reduce the possible eddy current effects. The two stage amplification system was replaced with a single amplifier. Since there was no RTS observed in D2, no time-domain data were obtained. Noise data were gathered manually from an HP3561 spectrum analyzer and IV characteristics were gathered via computer with the SCPA.

High currents restricted the maximum measurement temperature to 120.8 K. The first four temperatures from D1 were targeted for D2 since comparison between devices

was a goal. Noise characteristics of D2 at the biases used for D1 indicated a need to change the bias values for D2. Therefore, D2 was negatively current biased at 11 different levels, 0, 35, 75, 150, 300, 475, 900, 1000, 2500, 4500, and 10^4 μA for each of four temperatures, 81.66, 91.3, 103.7, and 120.8 K.

Device III

Measurement conditions for D3 were the same as for D2 with the addition of RTS time domain data being collected via computer when observed. Again, high currents dictated that the maximum temperature be 120.8 K. The same bias networks and temperatures as those used for D2 were used for D3.

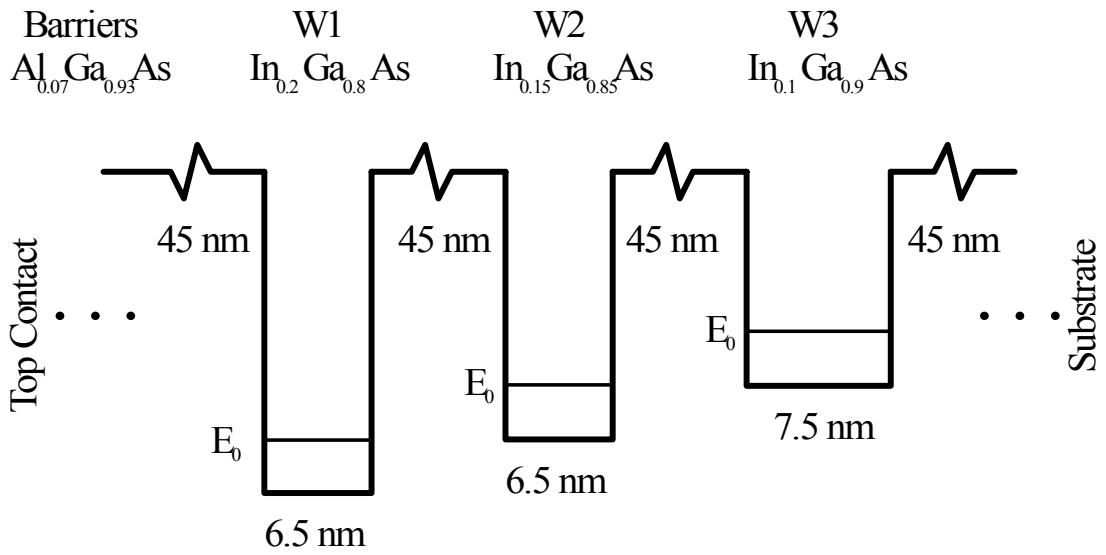

Figure 4 Design values of material and growth parameters for Device 1.

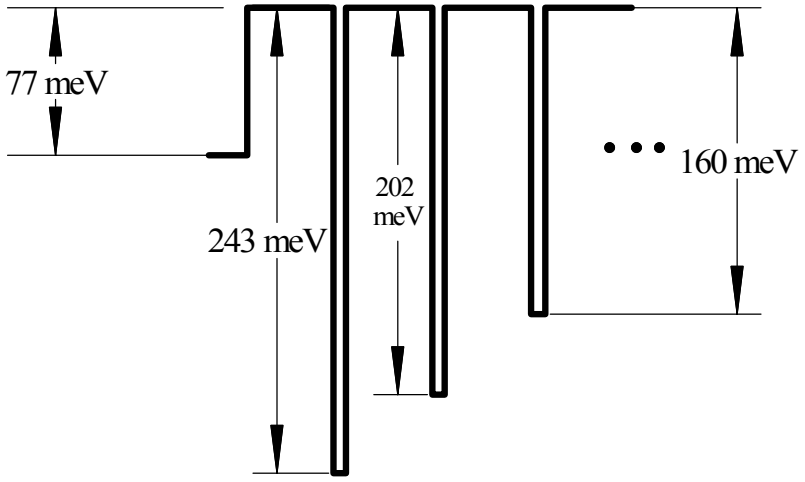

Figure 5 Conduction band edge energy relationships for Device 1.

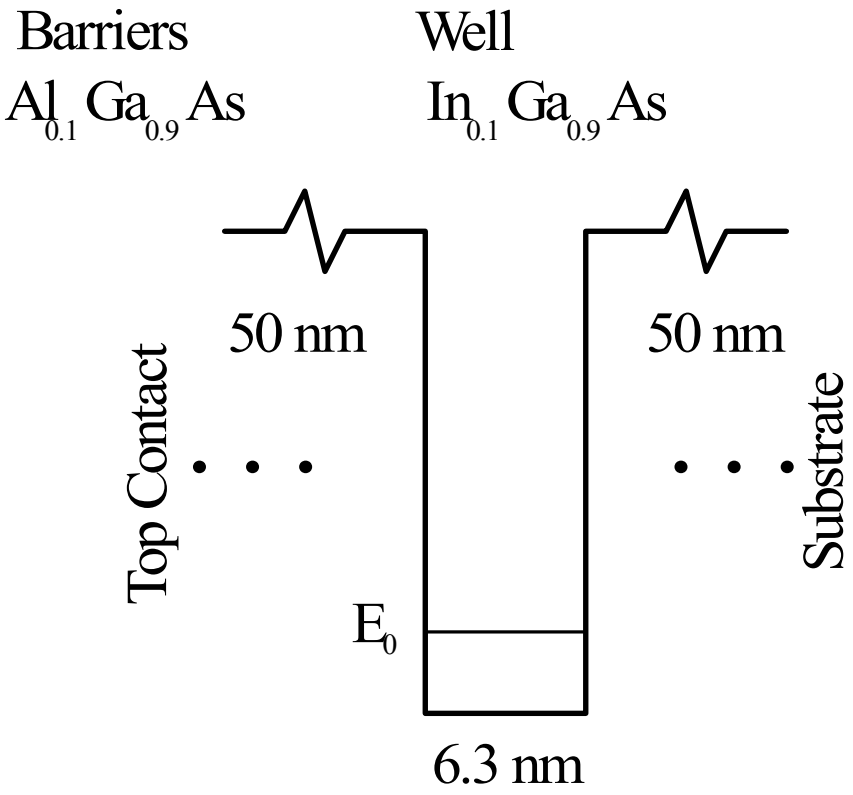

Figure 6 Design values of material and growth parameters for Device 2.

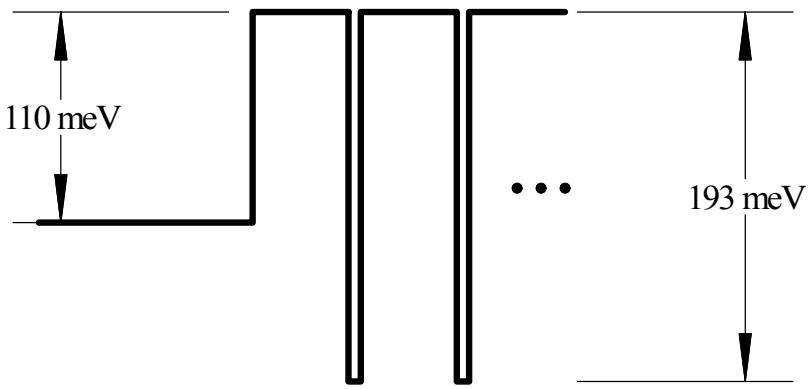

Figure 7 Conduction band edge energy relationships for Device 2.

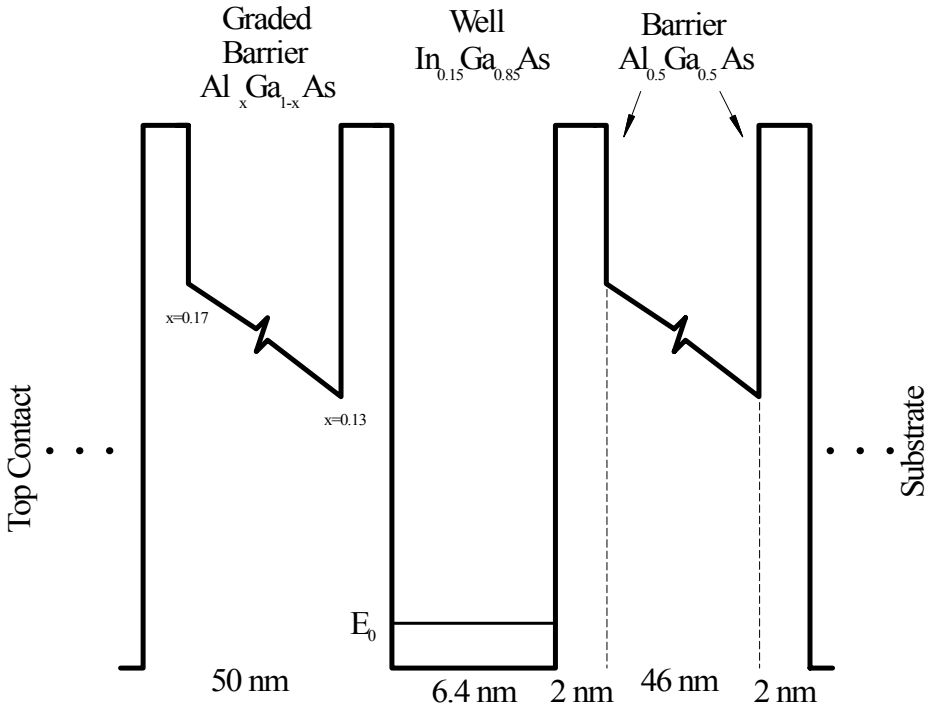

Figure 8 Design values of material and growth parameters for Device 3.

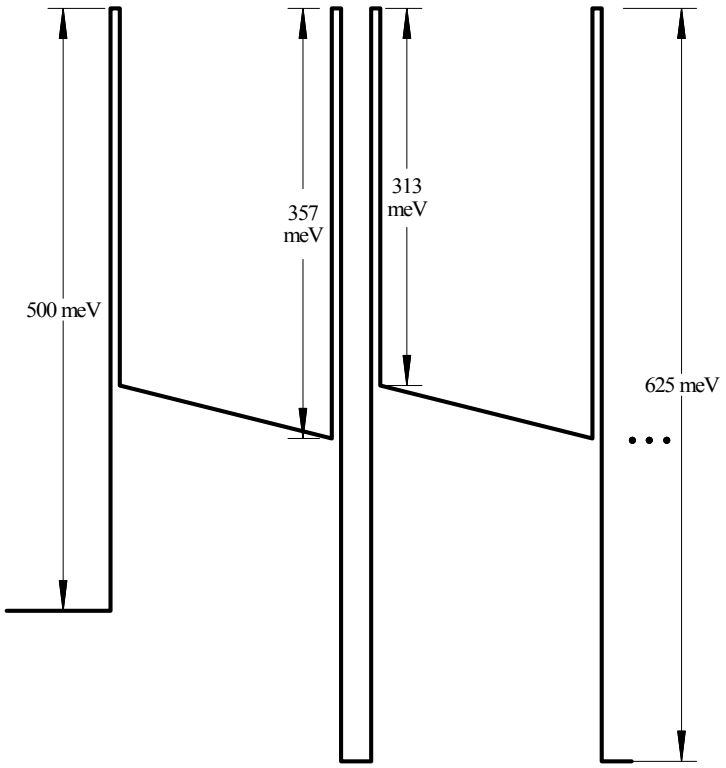

Figure 9 Conduction band edge energy relationships for Device 3.

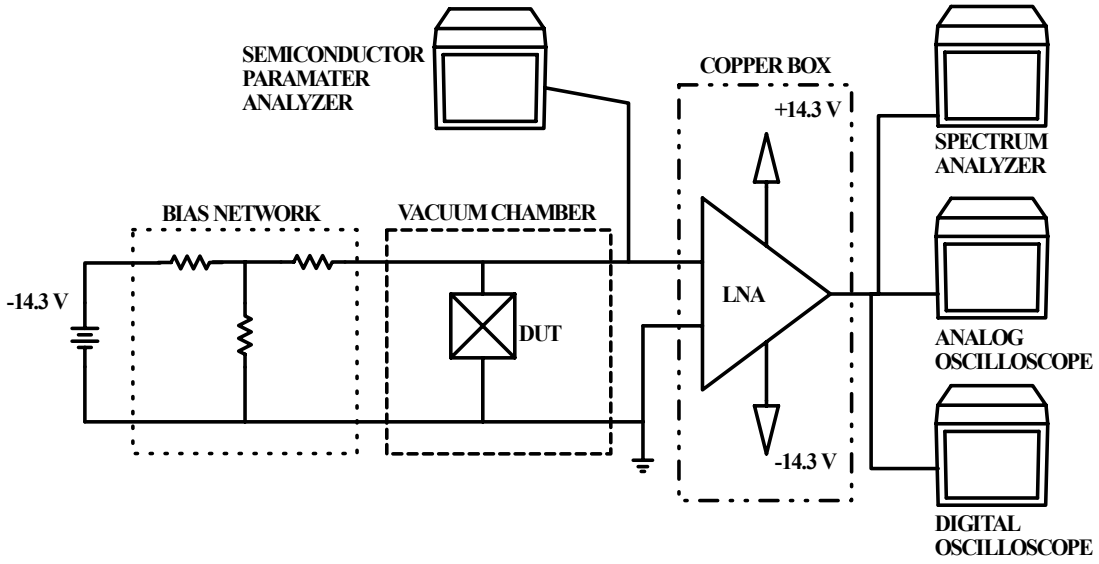

Figure 10 General experimental set-up.

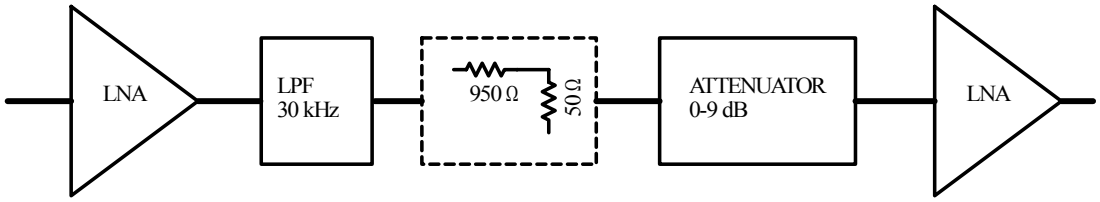

Figure 11 Block diagram of the amplification used with Device 1.

CHAPTER 3
SIMULATION

In order to obtain needed device parameters for analysis and theory verification, numerical simulations were performed for each device. Verification of the simulation results was obtained by comparison with the device designer's specifications, hereafter referred to as nominal values, and simulations. Two different simulations were run using common input data from the output of Fish1D, software available from Purdue University [17], which solves Poisson's equation for heterostructures in one dimension. Some modification of Fish1D was performed to increase the number of nodes allowed. Material parameters were collected primarily from two sources [18, 19].

Schroedinger Equation

Finite element analysis of the one dimensional Schroedinger equation was programmed in Matlab® for determination of the bound and quasi-bound states in each device. The program conceptually follows the presentation given in Silvester and Ferrari [20]. Input for the Schroedinger solver was obtained with Fish1D. Inputs to Fish1D are material parameters as a function of position and are given in tables in chapter 2 of this work. The material parameters for the barriers are resident within Fish1D so the only inputs required are the mole fraction of aluminum and the electron affinity.

The output of Fish1D is a single iteration solution of Poisson's equation in one dimension. It produces preliminary conduction band perturbations and the Fermi energy level for zero bias at the chosen temperature. In order to achieve a realistic energy picture, the nominal contact doping could not be used in the input to Fish1D. An

effective contact doping was found independently that ensured correct placement of the Fermi energy in Fish1D.

Computational limitations were such that the whole structure of D1 could not be simulated. Therefore simulations were performed on a single period of the device and on six periods of the device. For D2 and D3 simulations on a single period of each were performed in addition to simulations of the entire devices.

Transfer Matrix Method

Tunneling coefficients as a function of energy were determined for each device by programming transmission matrix equations in Matlab®. The transmission matrix method (TMM) followed is outlined in Datta [21]. To validate the program, the results obtained for tunneling through a square potential barrier were compared with two accepted analytical expressions. First, as presented in Morrison [22] for electrons with energies below the barrier height, the transmission coefficient is given by

$$T(E) = \frac{\beta^2}{\frac{1}{4}\left(1+\beta^2\right)^2 \sinh^2 \kappa L + \beta^2} \tag{3.1}$$

where E is the electron energy, β is the ratio of the wave number (k) to the decay constant (κ), and L is the width of the potential barrier. The second is

$$T(E) = \exp(\alpha d) \tag{3.2}$$

where d is the width of the potential barrier and α is given by

$$\alpha = -2\sqrt{\frac{2m_n^*\left(E_b - E\right)}{\hbar^2}} \tag{3.3}$$

where E_b is the barrier height, E is the electron energy, $\hbar$ is Planck's constant divided by 2π, and m_n^* is the electron effective mass in the barrier. The results are compared

graphically in Figure 12 and establishes that the transmission matrix method program is viable.

The conduction band and material parameters input to this program were the output of a single iteration of Fish1D as in the previous method. In addition, barrier lowering and bias variation were incorporated. The conduction band input was at thermal equilibrium with no bias applied. The Schottky barrier lowering is accounted for as a function of position using the following equation from van der Ziel [23],

$$\phi(x) = -\frac{q^2}{16\pi\varepsilon x} - q\mathscr{E}x \tag{3.4}$$

where ϕ is the amount of barrier lowering, x is position, ε is the permittivity of free space times the dielectric constant, q is elementary charge, and $\mathscr{E}$ is the applied electric field. The applied electric field is assumed to be a constant throughout the device and is calculated as

$$\mathscr{E} = \frac{V_a}{NL_b} \tag{3.5}$$

where V_a is the voltage applied, L_b is the barrier width, and N is the number of barriers. This assumes the wells have a high enough electron concentration, thus a low enough resistivity, so that there is almost no electric field within them.

Transmission probabilities calculated using the TMM are small in the energy neighborhood of the anticipated ground states in the quantum wells. This seems to be an anomaly but in fact it is easily explained. When an electron with kinetic energy that matches the expected ground state is injected at the contact, the probability of it transmitting through the first barrier is small. The barriers of these devices are designed specifically to prevent this behavior. The probability of transmission through each

successive barrier reduces the overall probability of transmission by a large factor. All that means is that the injected electron will not make it across the entire device. This is exactly as designed to reduce the dark current. In order to determine the ground state of the quantum wells with this method a different interpretation is necessary. To that end, the bound state energies are chosen based on their transmission probability being a local maximum. In general the local maximum is two to three orders of magnitude larger than the surrounding probabilities. Thus, as can be seen in Figure 13, even though the probability is small it is still significantly larger than its nearby energy neighbors and can be interpreted as an allowed energy state.

Results

Device I

The results of the Schroedinger solver for D1 are shown numerically in Table 4 and graphically in Figure 14. As can be seen there is some variation between simulation of a single period and multiple periods. For this device those variations are emphasized by the band bending due to the quantum well depth differences. In the multiple period device a wide triangular well is formed that spans from well 1 of a period to well 1 of an adjacent period. This enables the program, which finds only bound states, to find states above some of the barrier conduction band edges. The single period device has no such construct so the program finds only the well ground states.

Nominal values given by the device designer [15] are compared with values obtained with the Schroedinger method outlined above. That comparison is summarized in Table 5. A difference of less than 10% was obtained with the caveat that the second bound state for each well is approximated using the physical barrier height. This is an

underestimation of the next allowed energy state and would therefore overestimate the wavelength.

Table 4 D1 Schroedinger solution

SCHR	1 Period	6 Periods
DEVICE I	E_n (meV)	E_n (meV)
$E_{0,w1}$	82.93	76.67
$E_{0,w2}$	89.68	81.54
$E_{0,w3}$	77.86	84.15
$E_{1,w1}$	NF*	232.30
$E_{1,w2}$	NF*	216.12
$E_{1,w3}$	NF*	195.94

*NF=not found

$E_{c,contact}$ = 60.44 meV

Table 5 D1 Comparison with nominal, Schroedinger

SCHR	1 Period			6 Periods		
DEVICE I	λ_{calc} (μm)	λ_{nom} (μm)	% diff.	λ_{calc} (μm)	λ_{nom} (μm)	% diff.
Well 1*	7.608	8.2	7.78	7.968	8.2	2.92
Well 2*	9.777	9.7	0.79	9.214	9.7	5.28
Well 3*	12.467	11.8	5.66	11.092	11.8	6.38

* physical barrier height used for E_1

In contrast to the Schroedinger method program, the transfer matrix method program will find any allowed states up to the maximum energy chosen by the programmer. In general the maximum energy values are chosen to be above the maximum conduction band edge energy. Table 6 shows a summary of the output for D1 and Figure 15 shows the same information graphically. Notice that the energy reference is different for the two methods. There are significant differences between the single period simulation results and the six period simulation results. Again, this is attributed to conduction band edge differences in the multi-period device. The energy values obtained by simulating six periods will be taken as representative of the entire device since four full periods are unaffected by the contacts.

Table 6 D1 TMM solution

TMM	1 Period		6 Periods	
DEVICE I	E_n (meV)	Tx Prob.	E_n (meV)	Tx Prob.
$E_{0,w1}$	10.98	5.494E-65	19.39	8.96E-314
$E_{0,w2}$	12.34	2.116E-65	#	#
$E_{0,w3}$	20.28	2.944E-61	#	#
$E_{1,w1}$	183.39	6.833E-01	159.41	2.811E-29
$E_{1,w2}$	157.21	4.194E-07	147.05	3.443E-64
$E_{1,w3}$	NF*	NF*	129.24	4.094E-118

*NF=not found, # single ground state found for whole device
$E_{c,contact}$ = 0 eV

Comparison of the TMM program with nominal values is shown in Table 7. The results for the six period device simulation is well within 10% of the nominal values and the single period device simulation shows a large discrepancy as expected. Since no other data are available regarding previous simulations, the presumption of representation will be adopted.

Table 7 D1 Comparison with nominal, TMM

TMM	1 Period			6 Periods		
DEVICE I	λ_{calc} (μm)	λ_{nom} (μm)	% diff.	λ_{calc} (μm)	λ_{nom} (μm)	λ_{calc} (μm)
Well 1	7.192	8.2	14.01	8.855	8.2	7.99
Well 2	8.480	9.7	14.39	9.713	9.7	0.13
Well 3	N/A	11.8	N/A	11.288	11.8	4.54

Device II

Results of the Schroedinger method are given numerically in Table 8 and graphically in Figure 16. The minor difference between the single period and whole device simulation is likely due to the barrier band bending. In the single period device the barriers seen by the quantum well are different than those seen by the interior quantum wells of the whole device. In the latter, the square barrier seen by the majority of the quantum wells will dictate the ground state energy rather than the band bending at the contact barriers. In the former, the only barriers exhibit band bending so will affect the ground state energy.

Table 8 D2 Schroedinger solution

SCHR	1 Period	10 Periods
DEVICE II	E_n (meV)	E_n (meV)
E_0	72.17	75.71

$E_{c,contact}$ = 49.93 meV

In contrast with the other two devices, the single device simulation results for D2 compare more favorably with the nominal values [16] than the whole device simulation for both methods. The comparison of nominal values with the Schroedinger results is given in Table 9. The single period simulation results underestimate the energy transition while the whole device simulation results overestimate it. This may indicate that the device designer simulated a single period rather than the entire device.

Table 9 D2 Comparison with nominal, Schroedinger

SCHR	1 Period			10 Periods		
DEVICE II	λ_{calc} (μm)	λ_{nom} (μm)	% diff.	λ_{calc} (μm)	λ_{nom} (μm)	% diff.
E_1-E_0	10.287	9.7	6.05	8.467	9.7	14.56

Results of the TMM method are given numerically in Table 10 and graphically in Figure 17. A large difference is noted between the transmission probability for the ground state energy calculated for a single period and the whole device. As well, the energy values for all allowed energy states are around 6 meV higher for the whole device simulation and is likely due to the effects of the contact barrier band bending in the single period device. Again, the energy reference is different for each type of simulation.

Table 10 D2 TMM solution

TMM	1 Period		10 Periods	
DEVICE II	E_n (meV)	Tx Prob.	E_n (meV)	Tx Prob.
E_0	12.08	9.4636E-34	17.55	4.4071E-177
E_1	139.80	9.9828E-01	145.69	9.7723E-01
E_2	145.51	9.5946E-01	151.38	9.8614E-01

$E_{c,contact}$ = 0 eV

Comparing nominal values with those obtained with the TMM program finds good agreement for both the single period device simulation results and the whole device simulation results. Although the single period device simulation results are slightly better than those for the whole device simulation results both are less than 1% different. This lack of disparity is not unexpected since this device has an uncomplicated morphology.

Table 11 D2 Comparison with nominal, TMM

TMM	1 Period			10 Periods		
DEVICE II	λ_{calc} (μm)	λ_{nom} (μm)	% diff.	λ_{calc} (μm)	λ_{nom} (μm)	% diff.
E_1-E_0	9.708	9.7	0.09	9.676	9.7	0.24

Device III

Fish1D disallowed a linearly graded barrier representation so a step approximation was used in simulation. Results for the Schroedinger method are given numerically in Table 12 and graphically in Figure 18. Increasing discrepancy is noted with each successive bound state, between the single period and whole device simulation results using the Schroedinger method. This is not surprising since the device is complex and some interpretation is required concerning the bound state values. For example, in the multi-period device the states found in the quantum wells close to either contact are at a lower energy than those found in the heart of the device. This is a result of band bending near the contacts. In the single period device any states found are affected by the aforementioned band bending. Thus states found in the single period device are expected to be at a lower energy than those found in the heart of the multi-period device. The median energy value is chosen to represent the bound state in the multi-period device. In addition, bound or quasi-bound states are possible at locations external to the quantum well in D3.

Table 12 D3 Schroedinger solution

SCHR	1 Period	5 Periods
DEVICE III	E_n (meV)	E_n (meV)
E_0	52.17	54.67
E_1	240.85	244.25
E_2	275.26	286.33
E_3	285.00	301.62
E_4	296.10	314.67

$E_{c,contact}$ = 93.70 meV

The normalized wave function magnitude for each bound (or quasi-bound) state represented in Table 12 is shown in Figure 20 for the whole device simulation and in Figure 21 for the single period simulation. E_0 and E_1 in both graphs are both well confined to the quantum well region. The remainder of the states shown have a larger probability outside the quantum well but still have an allowed state within it. These states are targeted to provide photo-excited electrons that will easily contribute to current.

Comparing results obtained by the Schroedinger solver and the nominal values given by the device designer reveals large discrepancies in the two methods. This may be accounted for by differences in method, material parameters, and device morphology. As shown below, matching methods with the device designer greatly improves the discrepancies.

Table 13 Comparison with nominal, Schroedinger

SCHR	1 Period			5 Periods		
DEVICE III	λ_{calc} (μm)	λ_{nom} (μm)	% diff.	λ_{calc} (μm)	λ_{nom} (μm)	% diff.
E_1-E_0	5.427	7.2	32.67	6.541	7.2	10.08
E_2-E_0	4.590	6.8	48.15	5.353	6.8	27.04
E_3-E_0	4.398	6.5	47.79	5.021	6.5	29.45
E_4-E_0	4.198	6.2	47.69	4.769	6.2	30.00

Results for the TMM method are given numerically in Table 14 and graphically in Figure 19. As in the Schroedinger method, energy values for the bound (or quasi-bound) states differ between the single period and whole device simulation results. The same

explanation holds as the input to this method is the same as for the above. Table 15 shows the comparison with the TMM method and the device designer's nominal values. Of note is that the device variation is reduced, most notably for the whole device simulation results. All differences are less than 10%, with three of the four being less than 5%.

Table 14 D3 TMM results

TMM	1 Period		5 Periods	
DEVICE III	E_n (meV)	Tx Prob.	E_n (meV)	Tx Prob.
E_0	31.37	1.9867E-41	35.12	2.3228E-121
E_1	180.35	1.3640E-08	194.15	8.0545E-24
E_2	190.52	7.9625E-05	209.44	2.8981E-13
E_3	202.85	1.0116E-03	222.75	1.5933E-03
E_4	218.58	6.2691E-03	238.75	4.8105E-04

Ec,contact = 0 eV

Table 15 D3 Comparison with nominal, TMM

TMM	1 Period			5 Periods		
DEVICE III	λ_{calc} (μm)	λ_{nom} (μm)	% diff.	λ_{calc} (μm)	λ_{nom} (μm)	% diff.
E_1-E_0	8.323	7.2	15.60	7.797	7.2	8.29
E_2-E_0	7.791	6.8	14.58	7.113	6.8	4.61
E_3-E_0	7.231	6.5	11.25	6.609	6.5	1.67
E_4-E_0	6.624	6.2	6.83	6.089	6.2	1.82

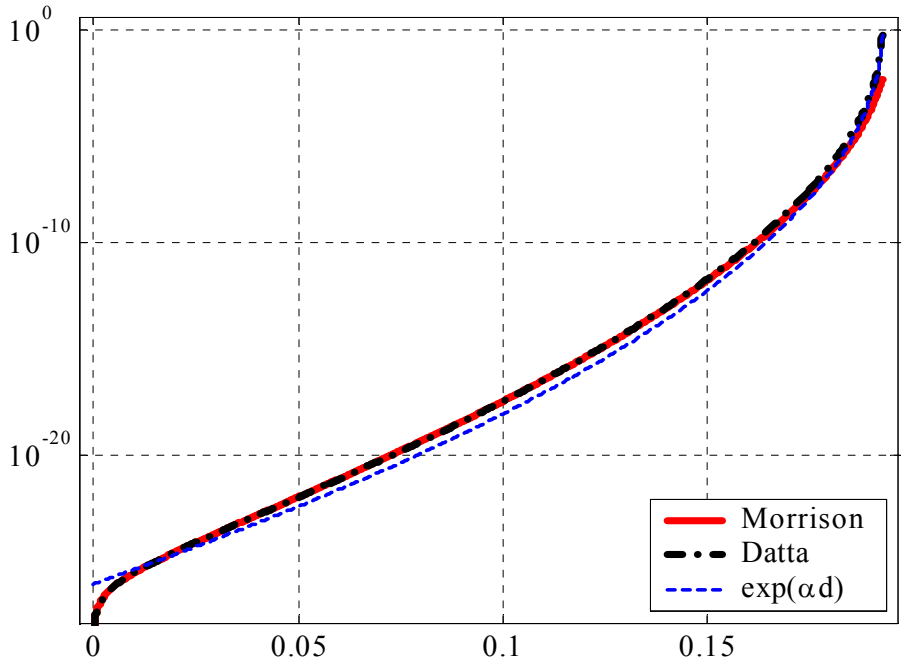

Figure 12 Comparison of three methods to compute the transmission coefficient through a square potential barrier.

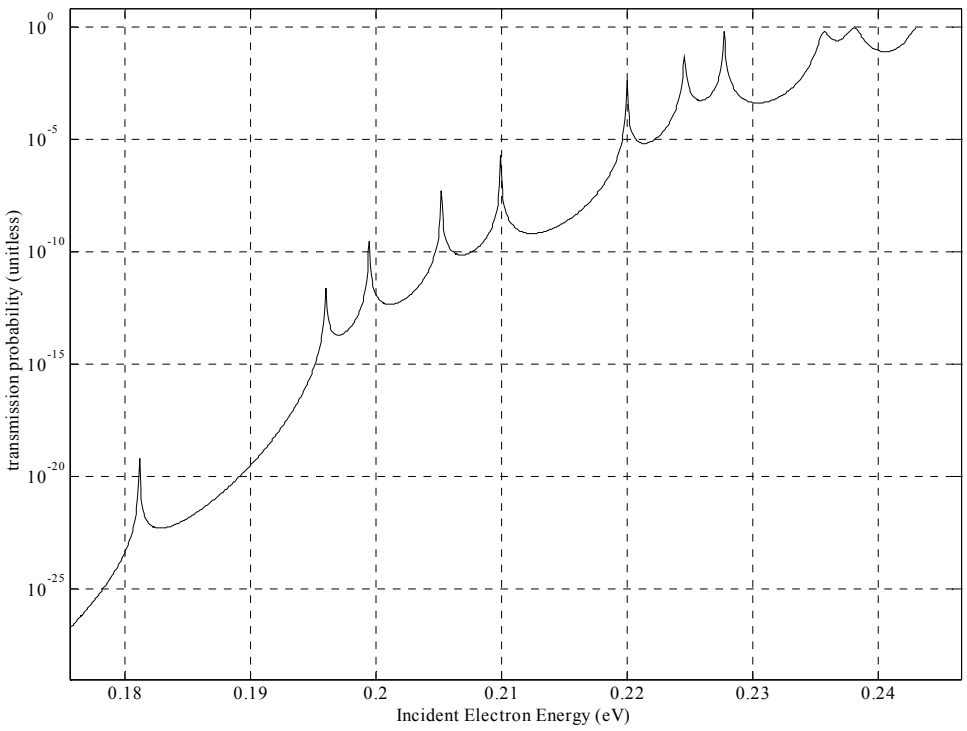

Figure 13 Device I, low bias, transmission coefficients versus incident energy.

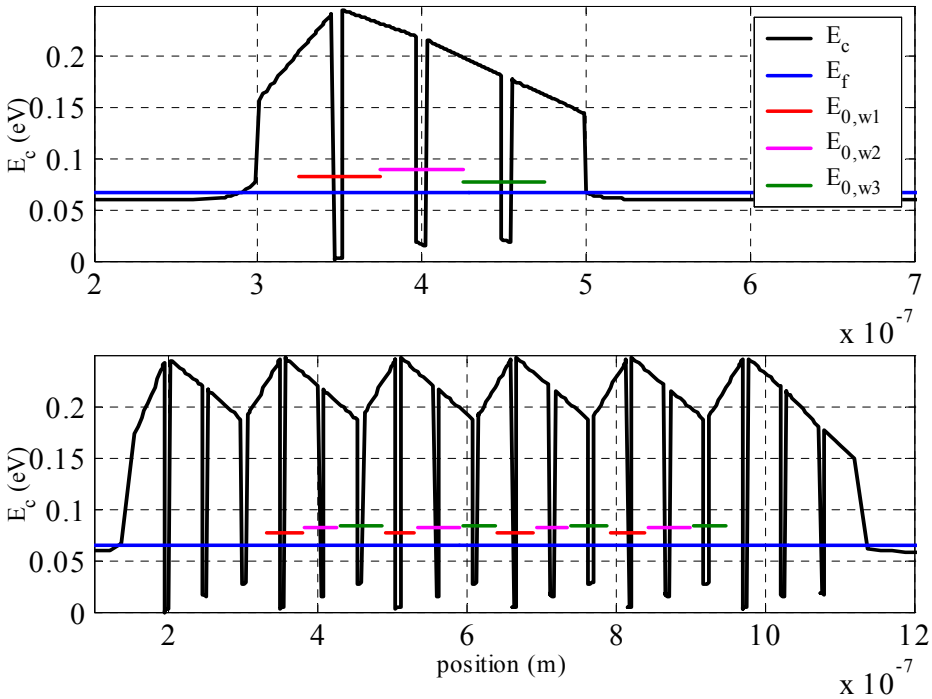

Figure 14 Device I results of the Schroedinger equation (FEM) for a single period (top) and for six periods of the 20 period device (bottom).

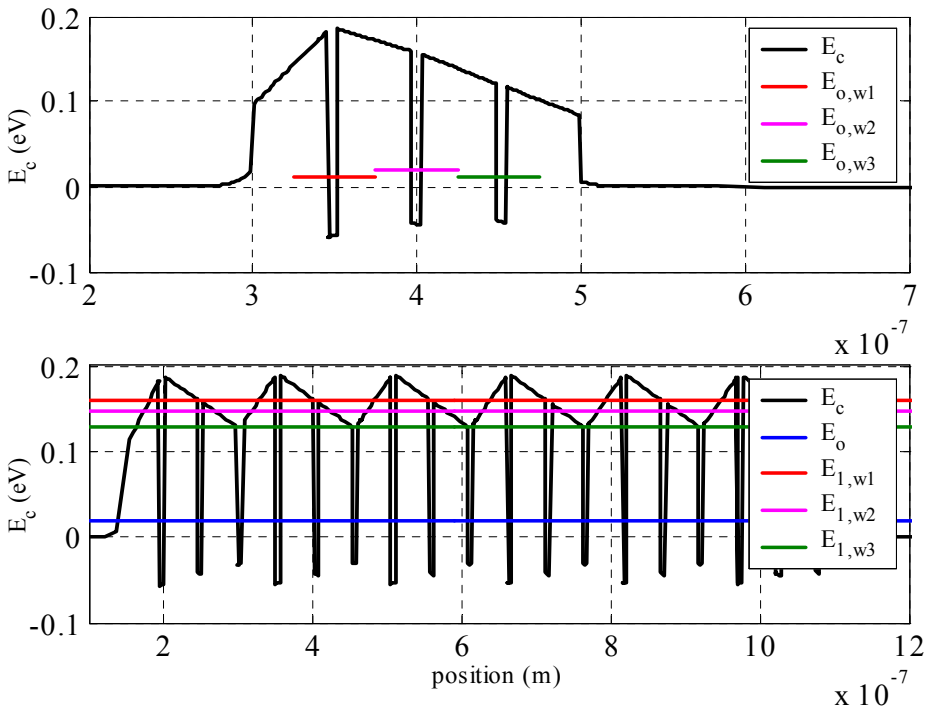

Figure 15 Device I results of the transfer matrix method for a single period (top) and for six periods of the 20 period device (bottom).

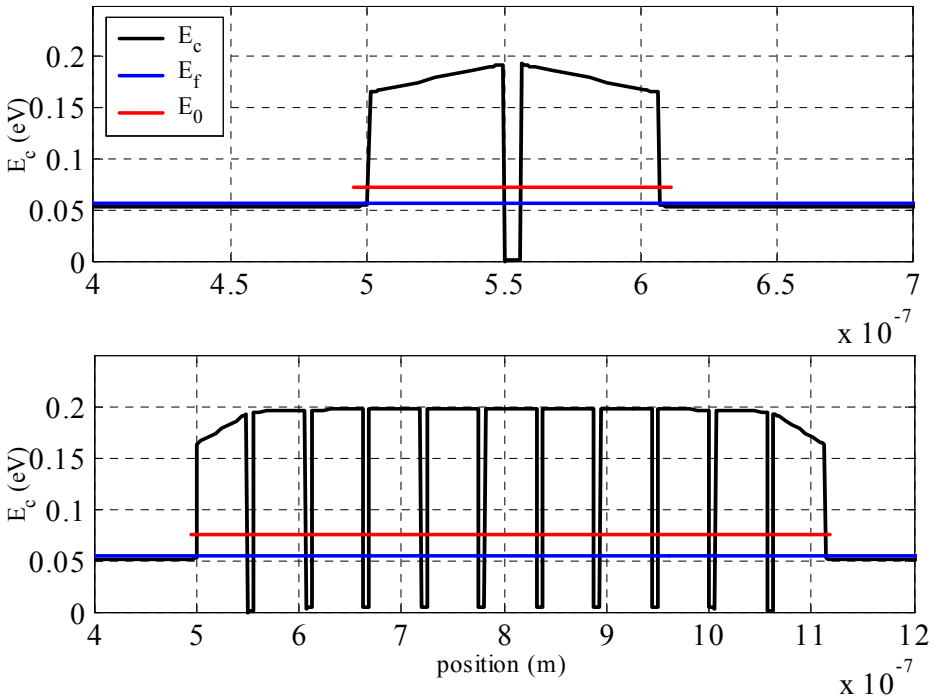

Figure 16 Device II results of the Schroedinger equation (FEM) for a single period (top) and for the whole device (bottom).

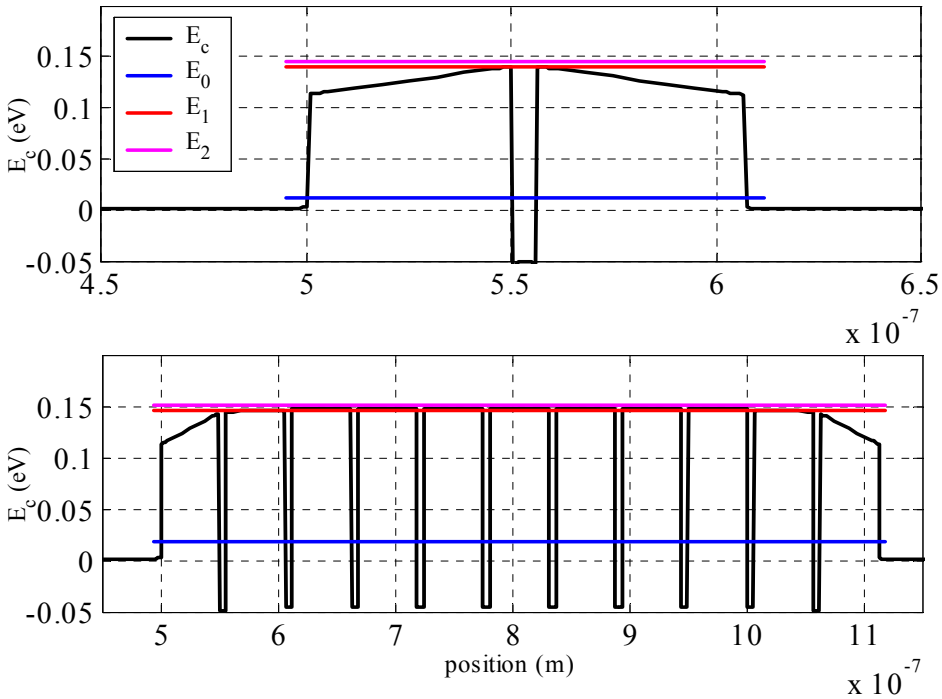

Figure 17 Device II results of the transfer matrix method for a single period (top) and for the whole device (bottom).

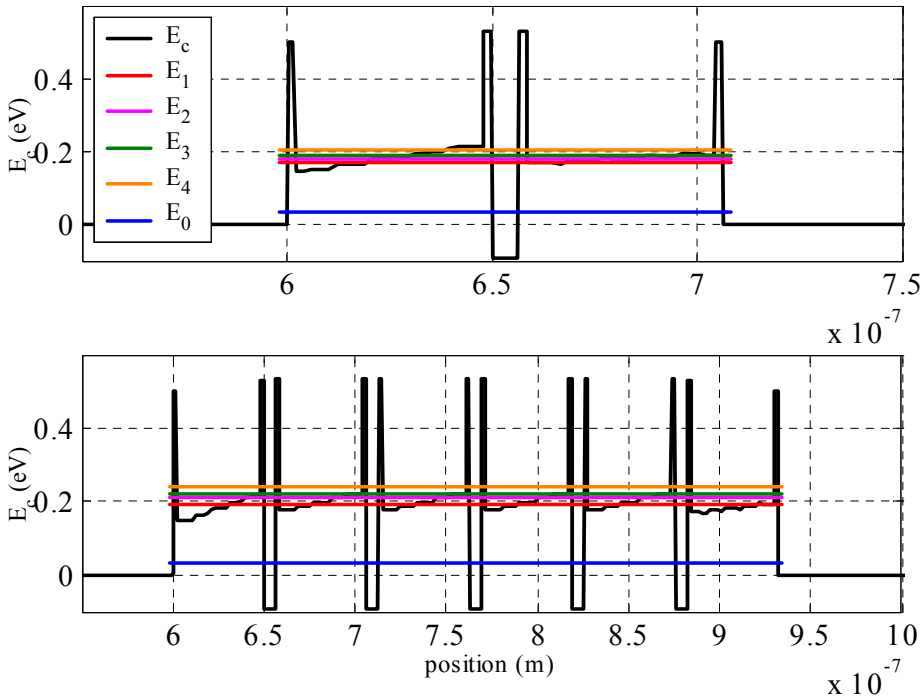

Figure 18 Device III results of the Schroedinger equation (FEM) for a single period (top) and for the whole device (bottom).

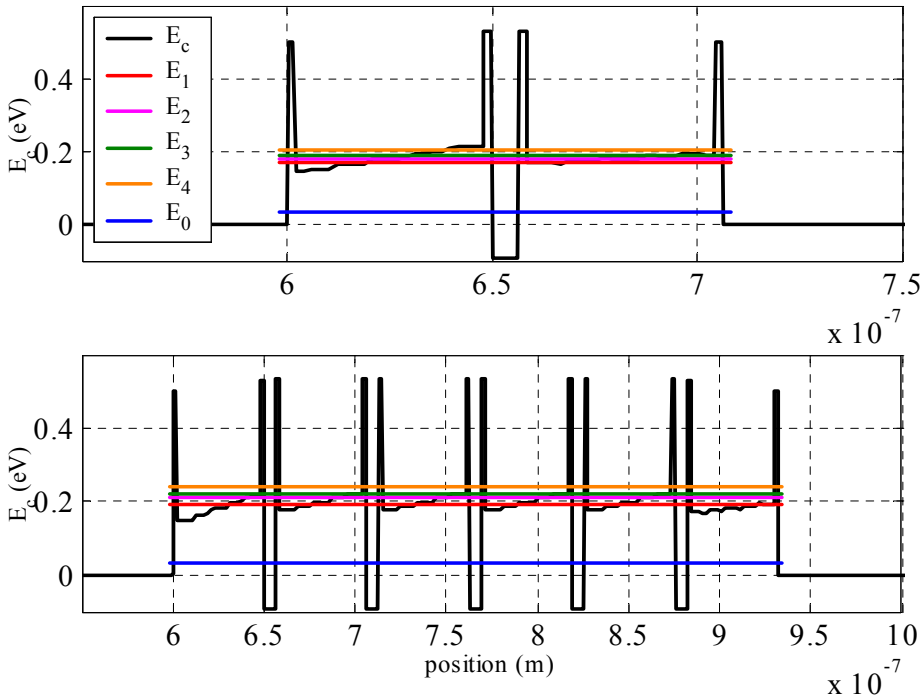

Figure 19 Device III results of the transfer matrix method for a single period (top) and for the whole device (bottom).

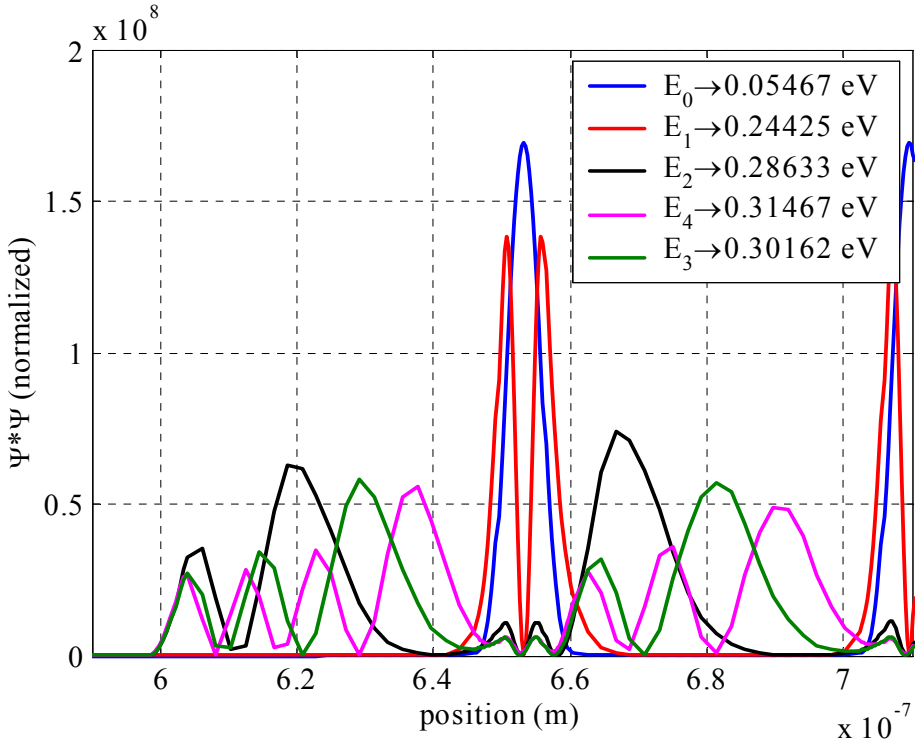

Figure 20 D3 normalized Ψ*Ψ, whole device simulation, zoomed in

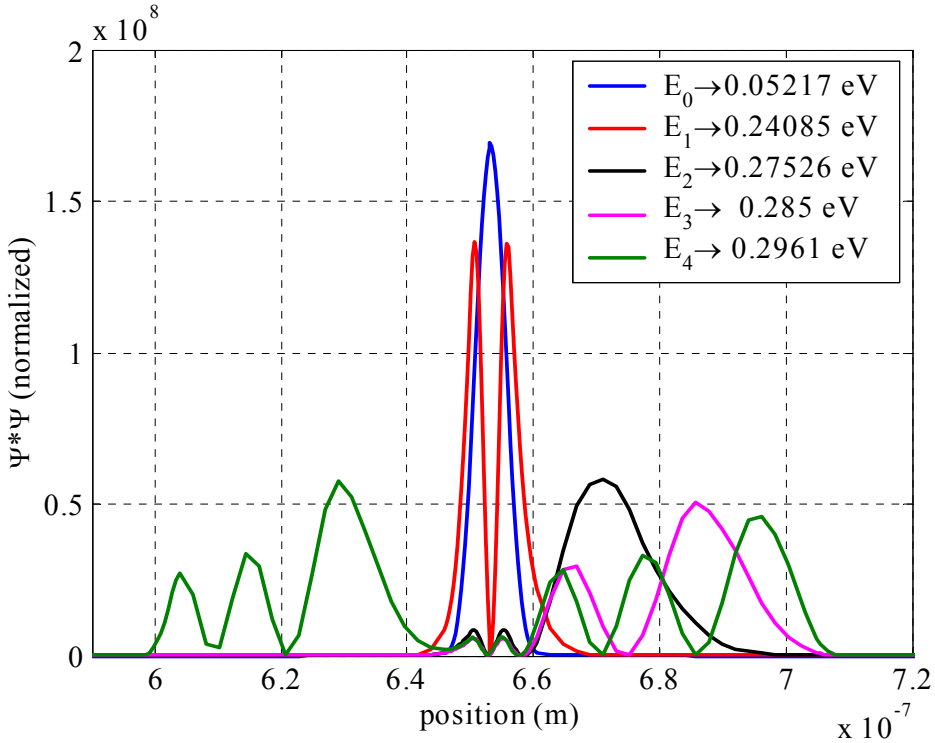

Figure 21 D3 normalized Ψ*Ψ, single period simulation.

CHAPTER 4
IV CHARACTERISTICS AND MODELS

QWIPs are typically utilized in a low temperature and high bias regime. This is precisely where a non-linearity in the dark current is observed. This is of concern as it will interfere with the photo-current and thus reduce the signal to noise ratio and the device's efficacy. Determining the physics behind this phenomenon will enable informed design choices as well as operating condition optimization.

To that end analysis was performed using the prevailing theories of charge transport in QWIPs, thermionic emission and tunneling. It is likely that tunneling current is the primary cause of the non-linear behavior. In addition, it appears that the bias regions used for noise measurements encompass the cross over from one mechanism to another. This may allow further insight into the noise behavior and perhaps the physics of QWIPs.

Theory

Thermionic Emission Current

Predicting the current due to thermionic emission requires a knowledge of the energy barrier height seen by the electron and the effects of bias on the energy configuration. In essence the barrier height is set by material and growth parameters. However, the bias conditions will modify this through the Schottky barrier lowering effect and band bending due to the electric field in the quantum well.

Thermionic emission occurs when an electron obtains enough thermal energy to exit the quantum well in an energy sense. The required energy is known as the activation

energy. What the electron does subsequently is determined by the conditions in the immediate vicinity of the well. In one dimension at zero bias the electron has three choices, recombine in the same position, diffuse left, or diffuse right as depicted in Figure 22. There is an equal probability of diffusion in both directions, therefore over time the amount of charge moving right balances the amount of charge moving left. This results in dynamic equilibrium with no net charge transport.

Under bias the energy configuration is modified from that at zero bias. Schottky barrier lowering results in a decrease in the activation energy. Band bending due to the applied electric field results in an additional energy difference between the two sides of the quantum well. These are shown stylistically in Figure 23 and mean that the energy picture seen by the electron is no longer symmetric. As well, the applied electric field provides directional impetus to the electron once it has exited the quantum well, resulting in net charge transport.

At low bias neither the energy changing effects nor the electric field impetus are strong. In this regime the current is approximately linear with voltage and due to thermionic emission. As the bias is increased the energy changes result in a consistent increase in numbers of electrons available for transport as well as velocity of electrons set in motion by the electric field. The increase in current is a direct result of the lowering of the energy barrier allowing less energetic electrons to exit the quantum well. In this regime the current begins to veer away from linear and is due to field-assisted thermionic emission. Increasing the electric field further results in a change in current that is no longer attributable even to field-assisted thermionic emission. In this regime the current appears to be exponential.

In the low bias, linear regime a preliminary picture emerges, in one dimension, of a series of resistances each statistically independent of the others. Since the quantum wells are doped and the barriers are not, the barrier regions may be approximated as a resistance between two contacts. Previous work [24] shows that at zero bias the electrons, if they diffuse, are most likely to diffuse to the nearest neighboring quantum well and recombine. Estimating the electron lifetime in the continuum on the order of picoseconds and the electron lifetime in the quantum well on the order of microseconds allows the assumption of statistical independence. Operationally this means that there is no correlation in carrier generation between the various sections of the device.

Current is a measure of how many electrons pass through a device cross section per second. In order to have no net current in one dimension, the number of electrons moving left must be matched by the number moving right. Shot noise is generated by the random motion of carriers across a barrier. Since diffusion is a random process then the electron motion through any cross section will be random, thereby contributing shot noise. Thus, in this construct, each direction of particle flow will contribute full shot noise to the system. This is stylistically depicted in Figure 24. Measured current noise spectral density will therefore be twice the full shot noise or

$$S_{i,barrier} = 4qI_0 \tag{4.1}$$

where I_0 is the zero bias generation current and q is the magnitude of the electric charge. With M statistically independent contributions, the total measured noise is

$$S_i = \frac{S_{i,barrier}}{M}. \tag{4.2}$$

Spectral density of current noise due to thermal scattering, also known as Johnson noise or Nyquist noise or diffusion noise, is a function of the dynamic resistance and temperature.

$$S_{i,Nyquist} = 4k_b T \Re\{G_{ac}\} \tag{4.3}$$

$\Re\{\ \}$ denotes the real part, G_{ac} is the dynamic conductance, k_b is Boltzmann's constant, and T is temperature in Kelvin. Solving for the thermal generation current, I_0, gives

$$I_0 = \frac{Mk_b T}{qR_{ac}} \tag{4.4}$$

in which R_{ac} must be at zero bias.

The thermionic emission current follows from the thermal generation current once barrier lowering and bias are taken into account. I_0 is proportional to $\exp\left(-\phi_b / k_b T\right)$ where ϕ_b is the activation energy for an electron in the quantum well. In order to account for the barrier lowering ϕ_b must be replaced with the lower energy required for activation, $\phi_b - \Delta E$. The new equation for the thermal generation current is

$$I_0 \exp\left(\frac{\Delta E}{k_b T}\right) \tag{4.5}$$

where ΔE is the total barrier lowering and is the sum of the Schottky barrier lowering and the lowering due to the electric field in the quantum well.

$$\Delta E = q\Delta\phi + q\mathscr{E}_w L_w \tag{4.6}$$

The first term is the Schottky model of barrier lowering and is given, at its maximum, by [23]

$$q\Delta\phi = q\sqrt{\frac{q\mathscr{E}_b}{4\pi\varepsilon_r\varepsilon_0}} \tag{4.7}$$

where ε_r is the dielectric constant for the barrier material, ε_0 is the permittivity of free space, and $\mathscr{E}_b^o$ is the electric field in the barrier. The second term in equation (4.6) accounts for the band bending due to the electric field in the quantum well. The thermionic emission current is given by

$$I_{TE} = I_0 \exp\left(\frac{\Delta E}{k_b T}\right)\left[1 - \exp\left(-\frac{qV_p}{k_b T}\right)\right] \tag{4.8}$$

where V_p is the magnitude of the voltage drop across a single barrier, hence accounts for the bias dependence.

Tunneling

In contrast to thermionic emission, tunneling is a quantum mechanical event that is not predicted by classical physics. The energy quantity of interest is no longer the activation energy but the tunneling barrier height. The tunneling barrier height, ϕ_t, is the energy distance between the activation energy and the kinetic energy of the electron that tunnels. Figure 25 is a stylized depiction of the energy relationships.

The transmission probability varies exponentially with the tunneling barrier height and is a measure of the likelihood that an electron with any given energy, below the activation energy, will move in space. In classical mechanics if an energy barrier exists that is greater than the total energy of the electron, the electron cannot change its position. In other words the transmission probability is zero. The same scenario viewed quantum mechanically reveals a finite transmission probability regardless of the total energy of the electron. The transmission probability will change according to the energy environment of the electron and can be anywhere between zero and one

Two major categories of tunneling are resonant tunneling and Fowler-Nordheim tunneling. The former requires alignment of the ground state energy in one quantum well with an allowed energy state in a neighboring well and a sufficiently short tunneling distance to make the transition likely. QWIPs are now designed to obviate resonant tunneling, by the width of the barriers and number of bound states per quantum well.

Fowler-Nordheim tunneling occurs through a triangular energy barrier. For example, when a square energy barrier shifts as a result of a uniform applied electric field as shown in Figure 23, energy requirements for transmission are perturbed such that the probability of an electron with kinetic energy lower than the activation energy getting 'free' of the quantum well is increased. This increase in mobile electrons requires a minimum electric field and results in an increase in current observed in the external circuit. One rendition [11] of the Fowler-Nordheim current equation is

$$I_{tun} = CV_p^2 \exp\left(\frac{-B}{V_p}\right) \tag{4.9}$$

with C a constant, V_p the voltage across one period, and with a uniform electric field assumed. The exponential term represents the tunneling probability with

$$B = \frac{4}{3}\frac{\sqrt{2m^*}}{q\hbar} L_b \phi_t^{3/2} \tag{4.10}$$

in which m^* is the carrier effective mass in the barrier, q is the magnitude of the electric charge, L_b is the barrier width, $\hbar$ is Planck's constant divided by 2π, and ϕ_t is the tunneling energy barrier height. The definition of the tunneling energy barrier height is shown stylistically in Figure 25 with no Schottky barrier lowering, and in Figure 26 with Schottky barrier lowering.

The tunneling probability representation in the Fowler-Nordheim equation is an approximation derived for electron transmission through triangular barriers [25]. A comparison between that approximation and the quantum-mechanically derived transmission probability [21] is depicted in Figure 27. The close agreement allows use of the approximation without trepidation. Figure 28 shows the energy picture used to make the above comparison.

A Fowler-Nordheim plot shows whether tunneling is a factor in charge transport and enables extraction of the tunneling barrier height if it is. Fowler-Nordheim plots are constructed by graphing I/V_p^2 versus $1/V_p$ on a semi-logarithmic plot. If a portion of this curve has a constant negative slope at high bias then tunneling is a factor in the current. The value of the slope is used to extract the tunneling barrier height, ϕ_t.

$$\phi_t = \left(\frac{-slope}{\frac{4}{3}\frac{\sqrt{2m_n^*}}{q\hbar} L_b} \right)^{2/3} \tag{4.11}$$

The denominator is material parameters (m_n^* is the electron effective mass and L_b is the barrier width) and constants (q is the magnitude of the electric charge and $\hbar$ is Planck's constant divided by 2π).

Analysis

Device I

The IV characteristic of D1 as depicted in Figure 29, appears nearly symmetric. Noticeable differences are seen at the lower temperatures where there is a shape difference between forward and reverse bias. Comparison on a double logarithmic scale as seen in Figure 30, clearly shows the extent of the asymmetry. At voltage magnitudes

below 40 mV, forward and reverse bias currents essentially match in both shape and magnitude. The curves do not meet again until ±3 V bias which is the maximum measured. Forward bias current magnitude is about two times that of the reverse bias at its maximum difference. This asymmetry is expected since the device geometry is not symmetric. The remainder of the analysis deals with only the reverse bias portion of these curves which is the operating regime of choice due to the lower dark current.

Focusing on the reverse bias curves in Figure 30 there appears to be two distinct regimes of operation. At bias magnitudes below 100 mV the IV relationship appears to be nearly linear for all six temperatures. The four lowest temperatures however, seem to remain linear until around 0.5 V. At higher bias magnitudes the IV characteristic takes a definite turn to super-linear. To determine what form these relationships take, thermionic emission and tunneling models were compared with the data.

Figure 31 and Figure 32 show the measured data, the thermionic emission model, and the tunneling model where applicable for each temperature. The bias values shown with the diamonds were measured at the time of the noise measurements. At the two highest temperatures the measured bias values are below the resolution of the parameter analyzer settings used for the IV characteristic. This is not anomalous, as an extension of the IV to those values affords a good fit. A total of six temperatures are shown, with the middle two temperatures being duplicated in the second figure for ease of comparison.

The extent to which the thermionic emission model fits the data is temperature dependent. Higher temperatures relate to a larger extent of prediction. At the highest two temperatures the fit is predictive up to 100 mV in magnitude. At higher magnitudes another mechanism is beginning to take effect. The highest bias magnitude measured is

not sufficiently high to explicitly show tunneling as that mechanism however. As the temperature is decreased below 144.3 K, the predictive value of the thermionic emission model also decreases. For example, at 121.2 K there is good agreement between the data and the model whereas at 82.1 K the agreement begins to deviate at a magnitude of 30 mV. Of note is that the thermionic emission model actually overestimates the current magnitude for 82.1 K, 91.7 K, 104.2 K, and 121.2 K until a second mechanism begins to dominate the current.

A likely candidate for this second mechanism is Fowler-Nordheim tunneling. To check this out a Fowler-Nordheim plot was generated and the barrier tunneling heights were extracted where possible. Looking at Figure 33, there is an obvious difference in behavior in each of the bottom three curves as $1/V_p$ decreases, or the bias magnitude increases. The top curve shows the same change but is not as far into the operational difference so the effect is not as strong and may not reflect the actual tunneling barrier height. The slope of the high bias portion of the curves contains the information required to extract the tunneling barrier heights.

Using the extracted tunneling barrier heights, given in Table 16, and plugging back into the Fowler-Nordheim equation a comparison was made with the IV characteristic. This comparison is shown in Figure 31 and Figure 32. Not surprisingly, the high bias fit appears to be perfect. This is due in part to the method of extracting the values from the data and plugging them back into the same equation. However, it also confirms that Fowler-Nordheim tunneling is a strong possibility and that it will not become an issue until relatively high bias is achieved.

Interpretation of the tunneling barrier height for this device is not straight forward due to its complexity. Recall that this device has three separate quantum well depths interspersed with homogeneous barriers. With reverse bias applied and image force barrier lowering, two periods of D1 would look like Figure 34 at 82 K or Figure 35 at 91.7 K. Contacts are not included in these pictures as the tunneling current will be coming from the quantum wells. An argument could be made that the quantum well with the smallest activation energy will provide the electrons for transport. Looking at Figure 34, in order to tunnel out of the shallowest quantum well, W3, the entire barrier width would have to be traversed. The probability of this is small and in fact is a design characteristic used to prevent tunneling. Tunneling has a higher probability of occurring from the other two quantum wells at this bias and temperature.

Table 16 D1 tunneling barrier height and constant *C*.

Temperature (K)	ϕ_t (meV)	C (A/V^2)
82.0	11.5	0.07
91.7	9.8	0.51
104.2	8.9	1.41
121.2	4.3	1.96

Figure 35 shows that at a slightly higher temperature, and therefore a slightly lower voltage magnitude, any electrons escaping from W3 are essentially blocked from going either direction. Transmission probability is driven by the tunneling energy barrier height. That means approaching either side of a triangular barrier will result in the same transmission probability. However, as an electron approaches a triangular barrier on the sloped side, its kinetic energy is reduced. This is depicted pictorially in Figure 36. Therefore the rate at which electrons travel varies depending on which side is approached. Since current is the rate of charge transport, it will be affected by which

slope of barrier is present. An electron from W1 has a probability of tunneling in either direction. However, tunneling to the left it quickly encounters recombination options that could erase its contribution to charge transport. If it were to tunnel to the right, it would gain energy from the electric field and thus contribute to the current.

The extent of band bending throughout the temperature and bias ranges measured is shown in Figure 37. As can be seen, low bias combined with high temperature results in virtually no band bending with some Schottky barrier lowering. Looking at the equilibrium energy band diagram in Figure 38, as predicted by a single iteration of Fish1D, it is most likely that electrons escaping from W1 would be the sole contributors to the current under low bias. This could explain the overestimation of the current by the thermionic emission model at low bias. Electrons thermally generated from either W2 or W3 will encounter an energy barrier within a short distance of each well. Though some tunneling is possible, each successive barrier crossing increases the probability of recombination or reflection. The exception would be when the quantum wells of interest are within one or two periods of the contacts since the band bending varies from that occurring deep within the device.

In contrast, low temperature and high bias results in the maximum band bending and barrier lowering. For this case, in addition to the thermally generated electrons from all three quantum wells it appears that W1 and W2 contribute electrons via tunneling.

Device II

The IV characteristic of D2, Figure 39, shows highly symmetric behavior for forward and reverse bias. This is not unexpected since it has a simple and symmetric material geometry. The small amount of asymmetry can be attributed to the growth process. The noise studies were done at reverse bias values for all temperatures. The

ground reference chosen by the device designer is the substrate. Thus negative bias means that the top of the mesa is more negative than the substrate. It is usually found that forward bias shows a slightly higher current for the same magnitude of reverse bias, which is not observed for this device.

When both axes are logarithmic as in Figure 40, the IV characteristic shows nearly linear behavior up to about 0.1 V bias at all four temperatures. An increase in bias magnitude beyond that results in non-linear current behavior. Lower temperatures show more marked behavior at smaller bias magnitude. It is expected that this trend would not vary if higher bias magnitudes were measured at higher temperatures. This was not done to ensure that the device remained intact for all measurements.

Each subplot in Figure 41 compares measured current with that predicted by the thermionic emission model outlined previously. At all temperatures good agreement is observed at bias magnitudes up to 100 mV. As bias magnitude is increased beyond 100 mV agreement breaks down and diverges most rapidly at the lowest temperature. Values of the bias voltage at which the non-linearity begins for each temperature fall between 0.1 V and 0.2 V. Assuming a uniform electric field at all temperatures and biases, the associated applied electric field is between 1.82 kV/cm and 3.64 kV/cm.

A Fowler-Nordheim plot of the IV characteristic at each temperature was analyzed for the characteristic negative slope region at high bias magnitudes and is shown in Figure 42. Only three temperatures are shown as data from the highest temperature showed no region of negative slope at high bias. In fact the plot for 103.7 K is potentially inaccurate since the current is obviously just barely into the operating regime consisting of tunneling. The tunneling barrier heights obtained for 81.66 K, 91.3 K, and 103.7 K

are given in Table 17. Comparison of the tunneling model with measured data is also included in Figure 41. For D2 the tunneling model must be added to the thermionic emission model for good agreement at high bias magnitudes. In addition, the transition region between the two regimes of operation is modeled accurately by the sum of the contributions from thermionic emission and tunneling.

Table 17 D2 tunneling barrier heights

Temperature (K)	ϕ_t (meV)	C (A/V^2)
81.66	6.0	0.83
91.3	4.4	1.88
103.5	2.0	2.85

Opposite extremes of band bending are shown in Figure 43 for the temperature and bias ranges measured. The maximum band bending occurs at the lowest temperature and the highest bias magnitude. Essentially no band bending occurs at high temperature and low bias. This is reflected in the temperature and bias dependence of the current. Whenever the conditions result in little or no band bending the only method of escape for an electron is via thermal generation. The current is then dictated by thermionic emission. Beyond a requisite electric field where band bending is no longer negligible, more electrons escape via tunneling thereby increasing the current. Tunneling escape of electrons becomes the dominant mechanism of current as the electric field increases beyond the transition region.

Device III

The IV characteristic of D3, Figure 44, exhibits marked asymmetric behavior between forward and reverse bias. This characteristic strongly argues for use of this device only in reverse bias. The dark current is at least a factor of ten lower and has a much more gradual increase in reverse bias as compared with forward bias. Focusing on

reverse bias, a second view of the IV characteristic is shown in Figure 45. An obvious change in the IV characteristic is noted for bias magnitudes greater than 300 mV. The diamonds give the bias values at which noise measurements were taken.

Comparison with the thermionic emission model is good at all temperatures for bias magnitudes less than 70 mV as can be seen in Figure 46. Above 70 mV in magnitude the thermionic emission model consistently underestimates the current.

A Fowler-Nordheim plot of the data for D3, Figure 47, reveals a strong tunneling component for each of the three lowest temperatures. As seen in Figure 48, a close-up of the Fowler-Nordheim plot, at 120.4 K the portion with negative slope has barely begun before the bias range is complete. Therefore the highest temperature value for the tunneling barrier height may not be accurate. The calculated tunneling barrier heights are given in Table 18. Looking at Figure 46 good agreement between the model and measured data is observed beginning between 1 and 2 volts magnitude. In Figure 46D, which shows the IV at 120.4 K, the model matches the measured data only in a short bias magnitude range close to 2 V. This is consistent with the observation noted from the Fowler-Nordheim plot.

Table 18 D3 tunneling barrier heights and constant

Temperature (K)	ϕ_t (meV)	C (A/V^2)
81.61	89.8	5.1
90.97	87.8	4.5
103.5	77.8	2.3
120.4	33.8	0.1

Of note is that in the region of bias magnitudes between 100 mV and 1 V, neither model adequately predicts the current behavior, nor does the sum of the two models. Insight may be gained by looking at the energy band configuration. One possible

explanation lays with the graded barrier energy configuration. Figure 49 shows the opposite extremes of band bending for the temperature and bias ranges measured. At low bias and high temperature the possibility of Fowler-Nordheim tunneling is small since the energy barrier is almost unperturbed from equilibrium. At high bias and low temperature the possibility for tunneling is greater due to the direction of band bending.

Figure 50 is a stylized picture of how the energy band is perturbed under both positive and negative bias. Under high enough positive bias the graded barrier is effectively neutralized. This means electrons capable of escaping above the low side of the graded barrier have no more impediments until the 2 nm barrier is encountered. Operationally the electron maintains its kinetic energy which further enhances the probability of tunneling through the next 2 nm barrier into the next quantum well. If no scattering occurs in the quantum well, the electron only has another 2 nm barrier between it and being swept away by the electric field. In addition, Fowler-Nordheim tunneling is not likely since the barrier approaches its maximum width.

Under negative bias the width of the graded barrier is effectively decreased. In addition, the electric field increases the kinetic energy of an electron that tunnels through the barrier. Resonant tunneling may be increasing the current in the bias range under question since continued band bending enables the bound state energies in the barrier region to resonate with transition states in the quantum well. However, typical evidence of resonant tunneling is peaks in the IV characteristic which are not seen in the data for this device. The three possible contribution paths are shown in more detail in Figure 51

Discussion

The thermionic emission model is shown to predict the low bias behavior of each device. As well, the tunneling model does reasonably well predicting the high bias

behavior of each device. The major differences in the transition region are tied to device complexity. For Device 2, the simplest of the three, the transition region is predicted by the sum of the two models. This is a logical result since it possible for both mechanisms to be operating concurrently due to the simple energy picture. Moving up in complexity to Device 1 which has three distinctly different quantum wells per period, the transition region is overestimated by the thermionic emission model at the lower four temperatures. One potential cause is that the bias induced band bending is not strong enough to overcome the effects of the equilibrium band bending. This would prevent electrons excited out of the shallower two wells from contributing to current unless they get enough energy to also get out of the pseudo-quantum well formed between two deep quantum wells. Thus thermionic emission would overestimate the number of charge carriers eligible to contribute to current. Finally, the most complex of the three devices tested, Device 3, produces more current than predicted by either model in the transition region. This speaks to the likelihood that a mechanism for electron generation exists other than what has been modeled in this work. Or perhaps a combination of mechanisms would account for the increase. In short, each device can be modeled at either extreme of IV behavior by one of these two models. Device complexity plays a key role in the ability to model the transition region of each device.

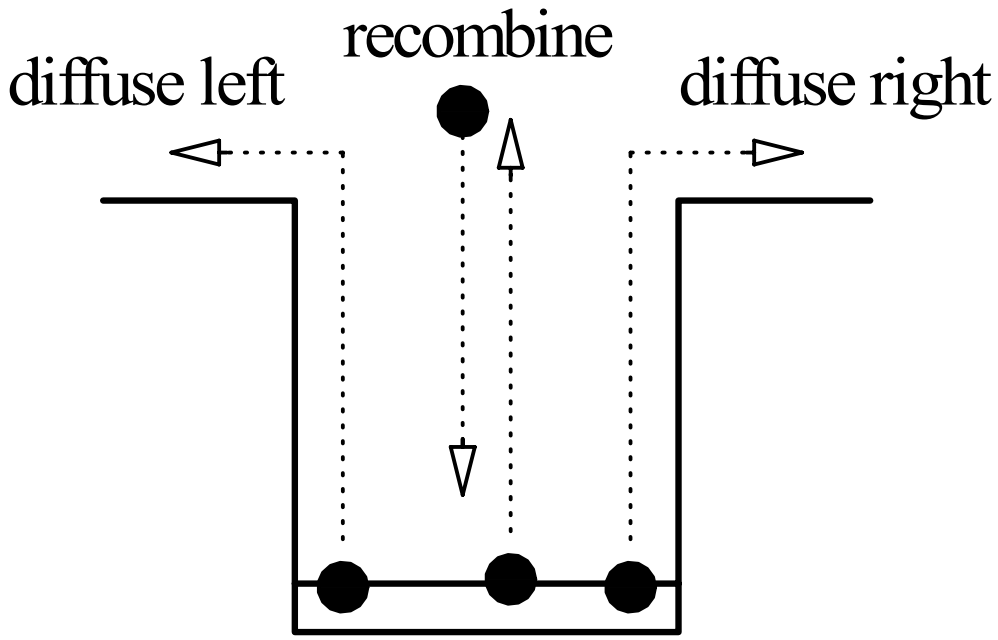

Figure 22 Choices for a generated electron at zero bias.

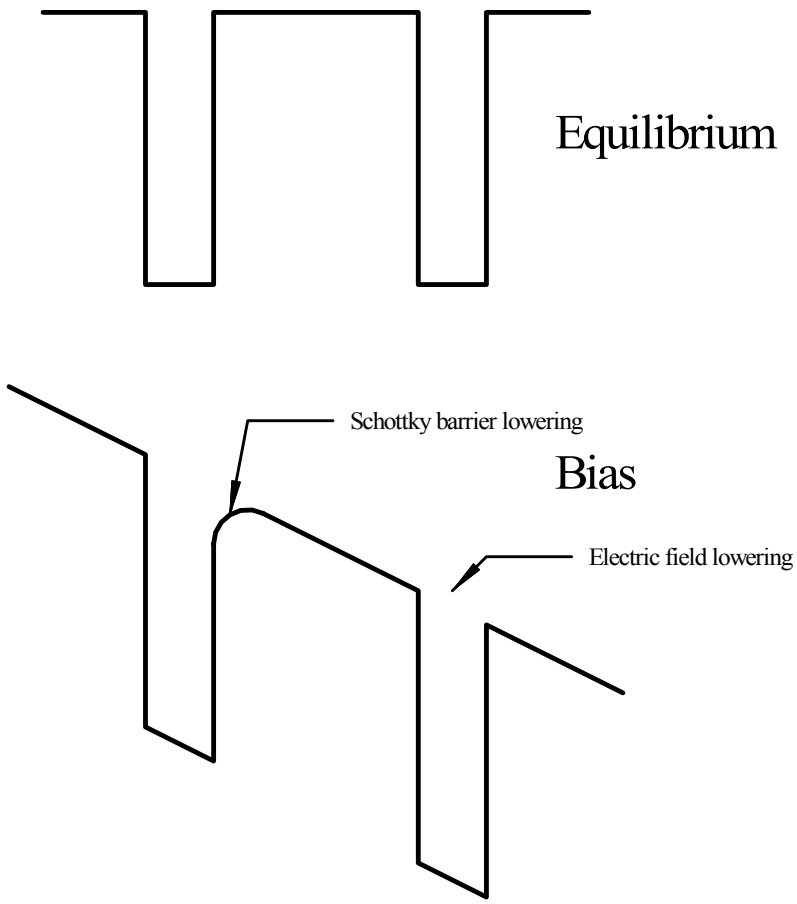

Figure 23 Two types of barrier lowering.

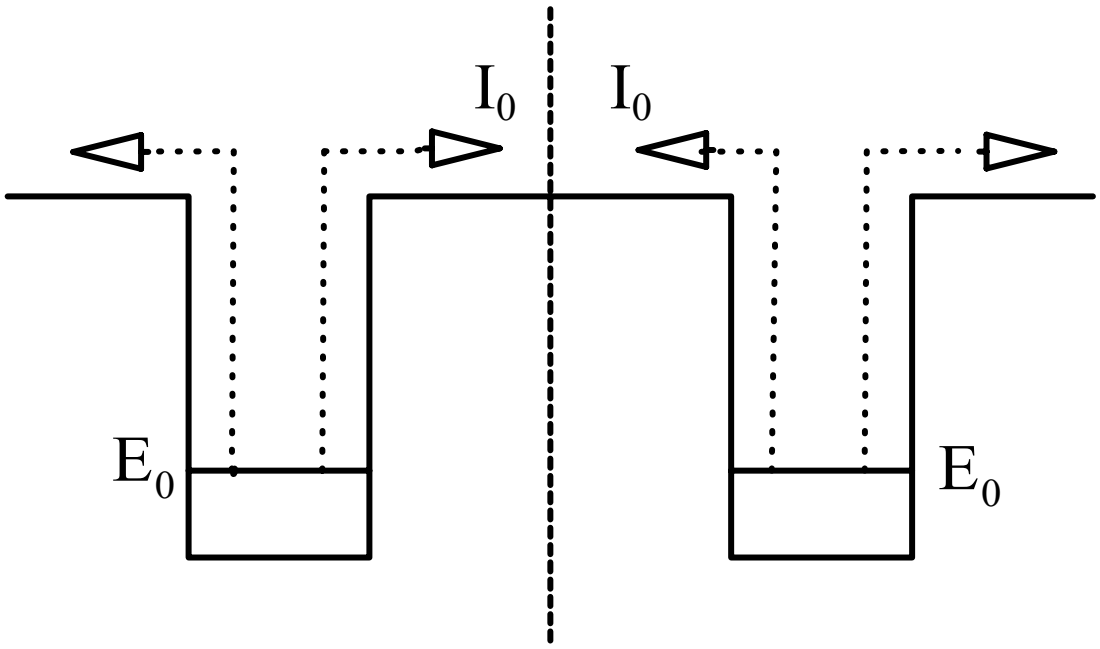

Figure 24 Stylized representation of the generation current at zero bias.

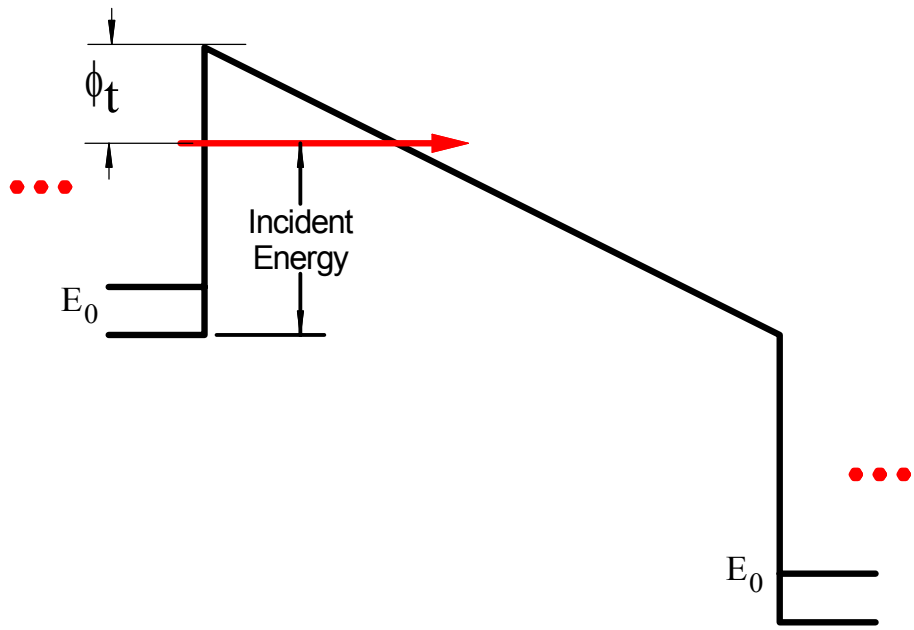

Figure 25 Energy picture of a barrier under bias without Schottky barrier lowering.

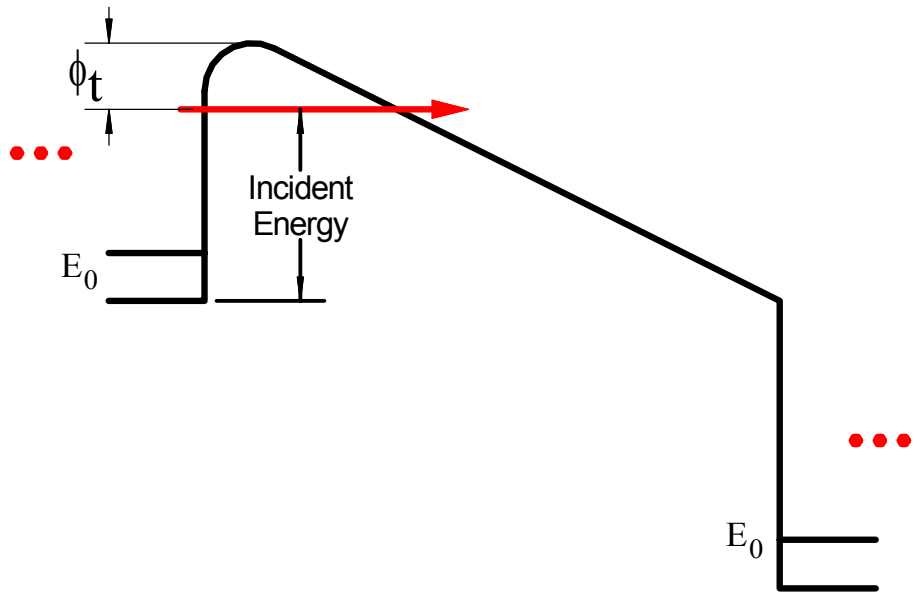

Figure 26 Energy picture of a barrier under bias with Schottky barrier lowering.

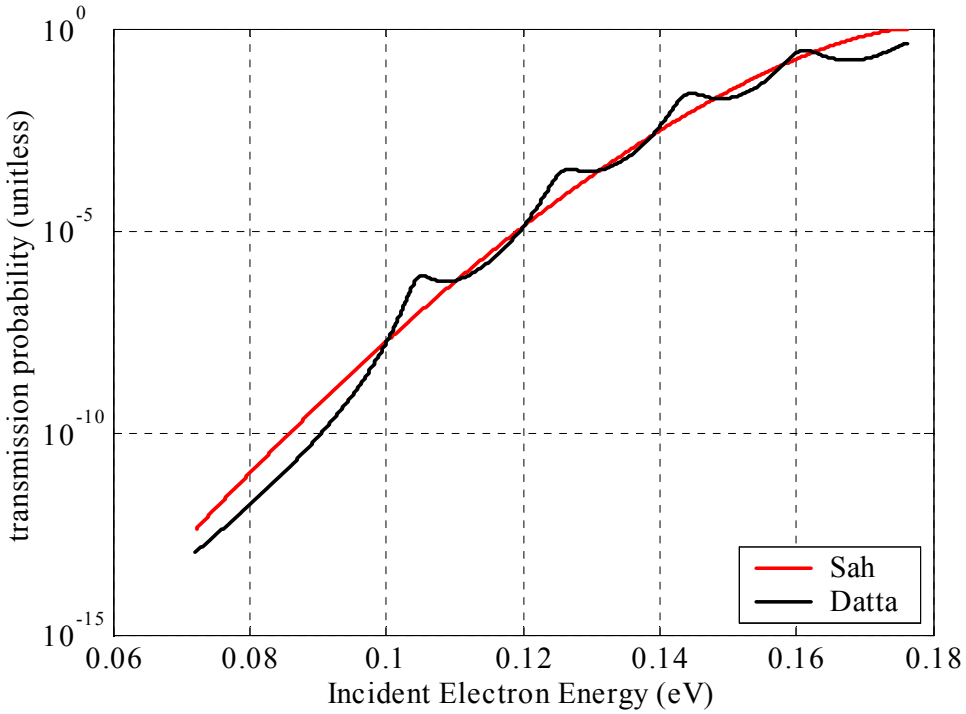

Figure 27 Comparison of two methods that determine the transmission probability of an electron through a triangular barrier including Schottky barrier lowering.

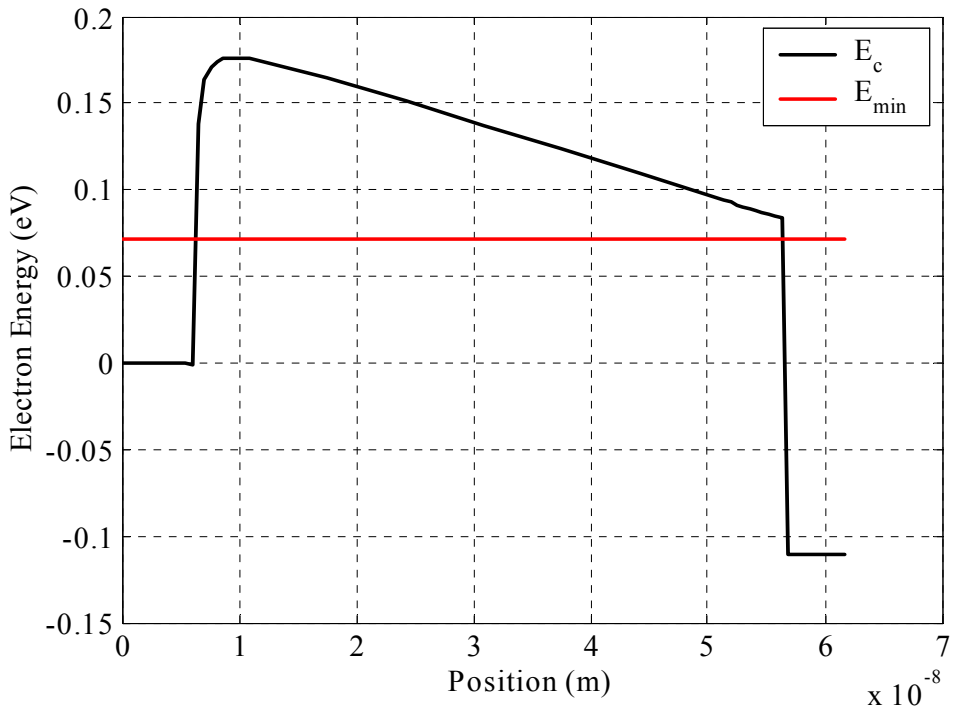

Figure 28 Energy picture for the barrier under bias used in the comparison of two methods to determine the transmission probability.

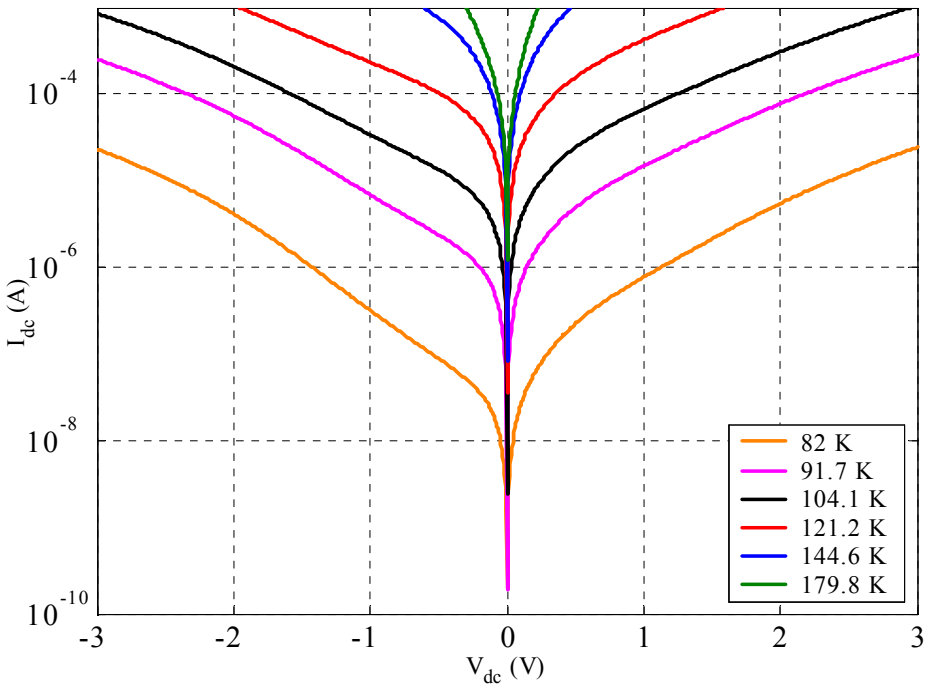

Figure 29 Device 1 IV characteristic at six temperatures.

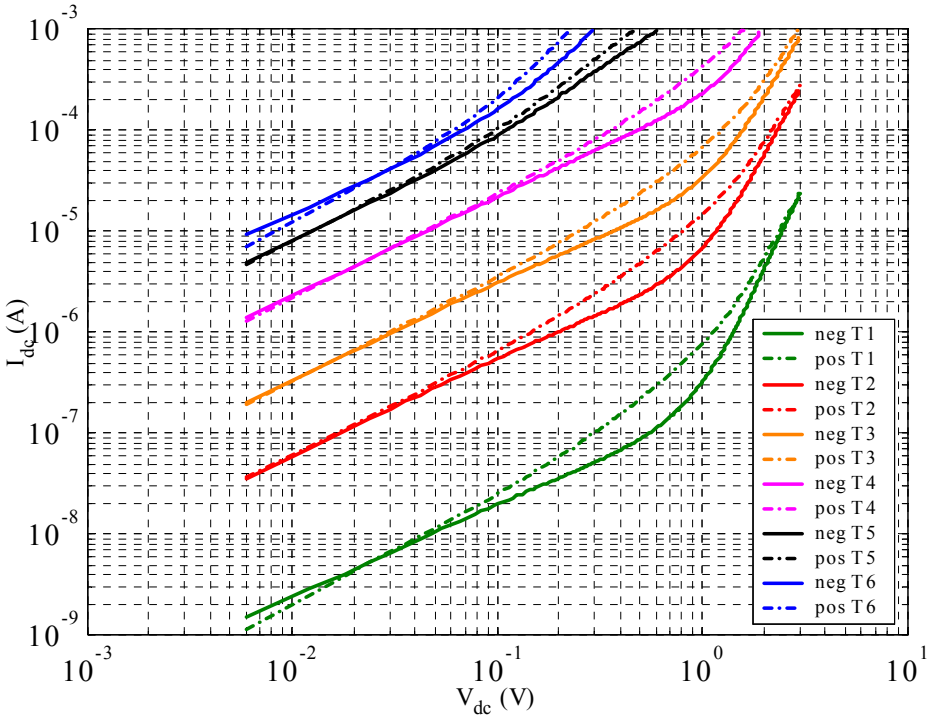

Figure 30 Device 1 double log IV characteristic at six temperatures.

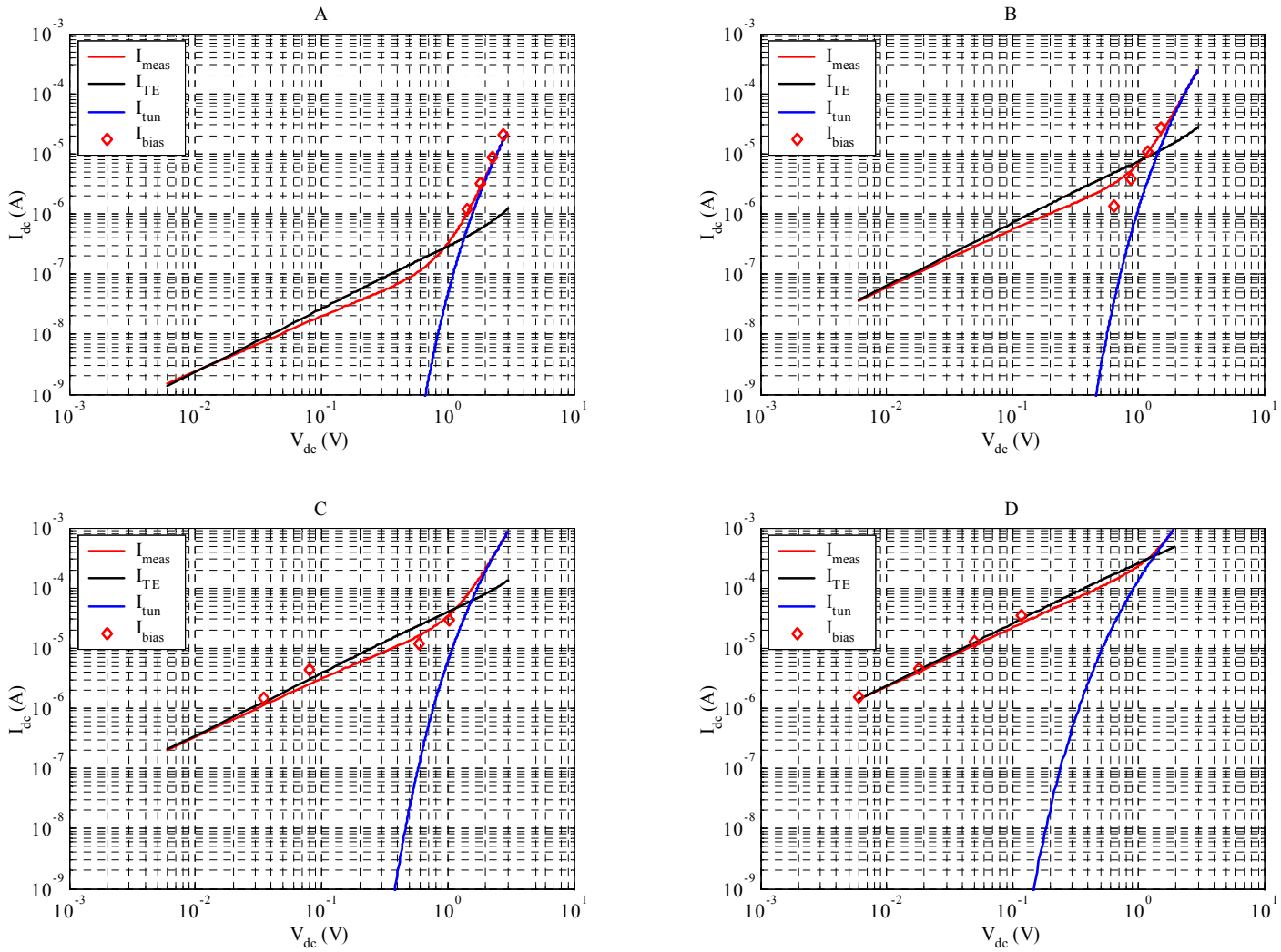

Figure 31 Device 1 measured and modeled IV characteristic at four temperatures. A) 82.1 K B) 91.7 K C) 104.2 K D) 121.2 K

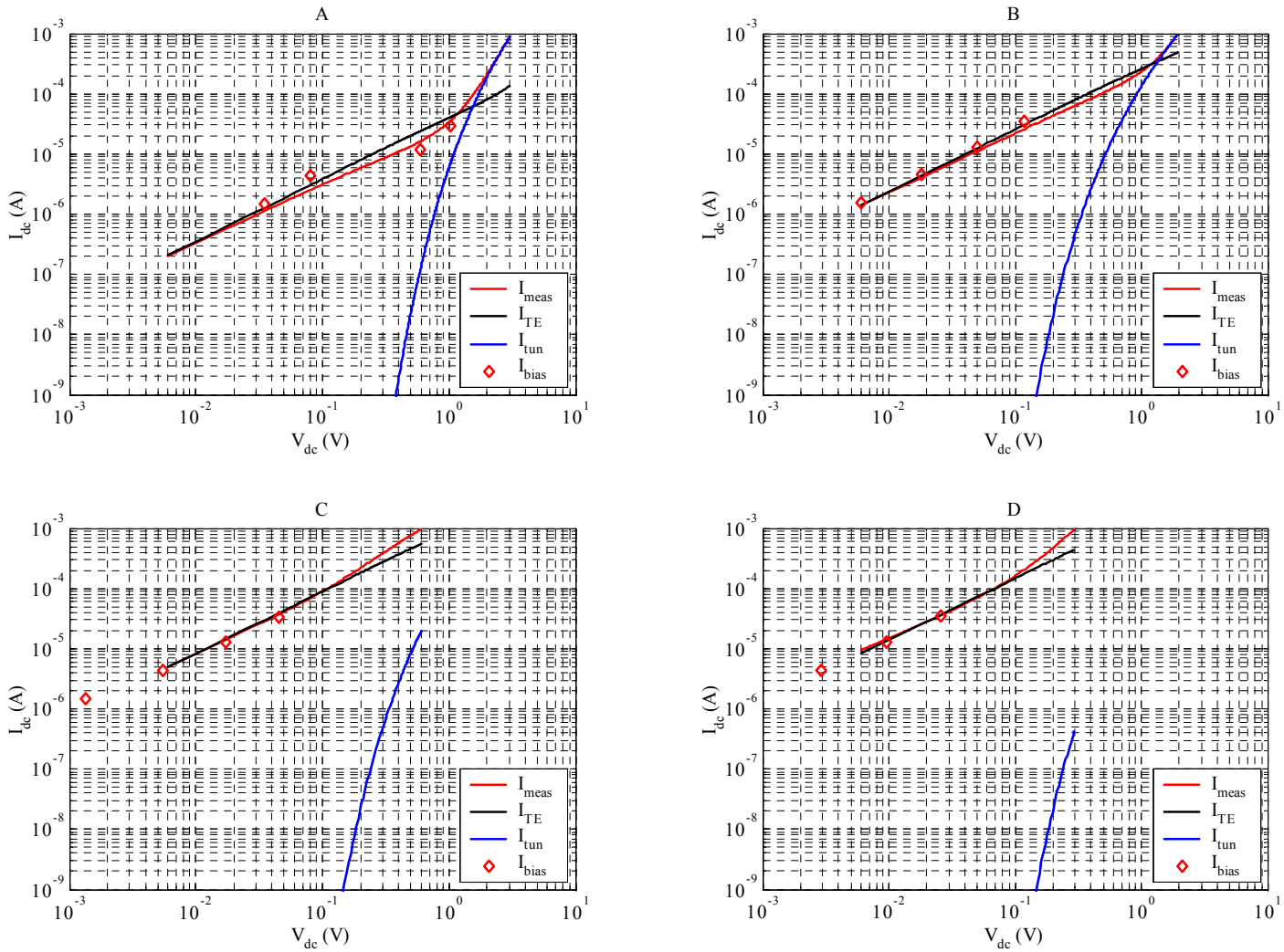

Figure 32 Device 1 measured and modeled IV characteristic at four temperatures. A) 104.2 K B) 121.2 K C) 144.3 K D) 179.8 K

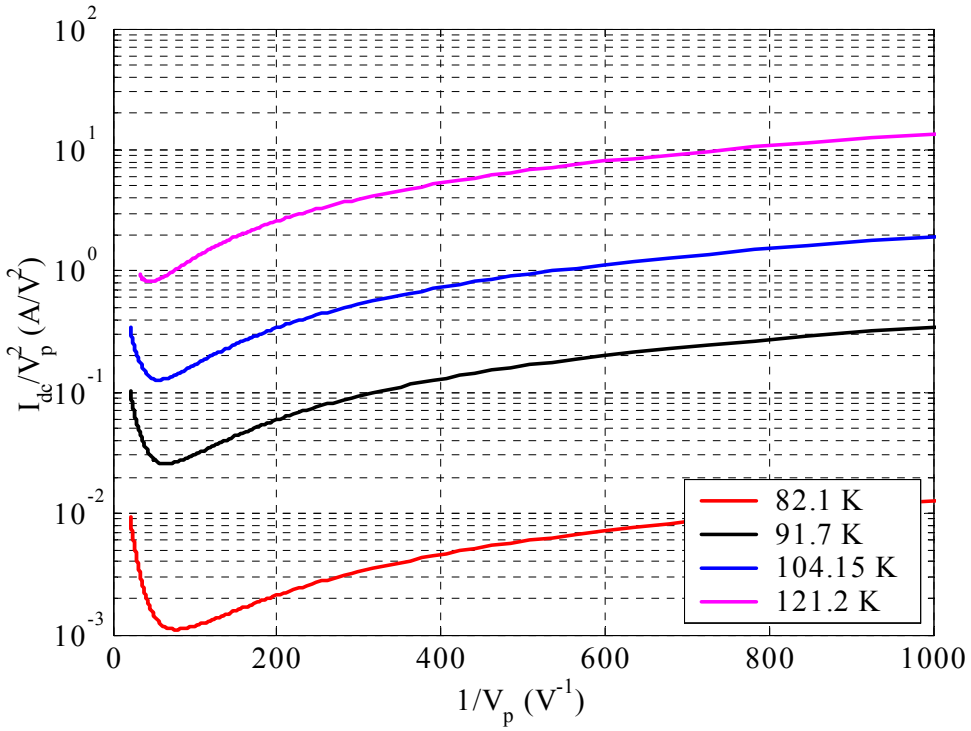

Figure 33 Device 1 Fowler-Nordheim plot of four temperatures, broad view.

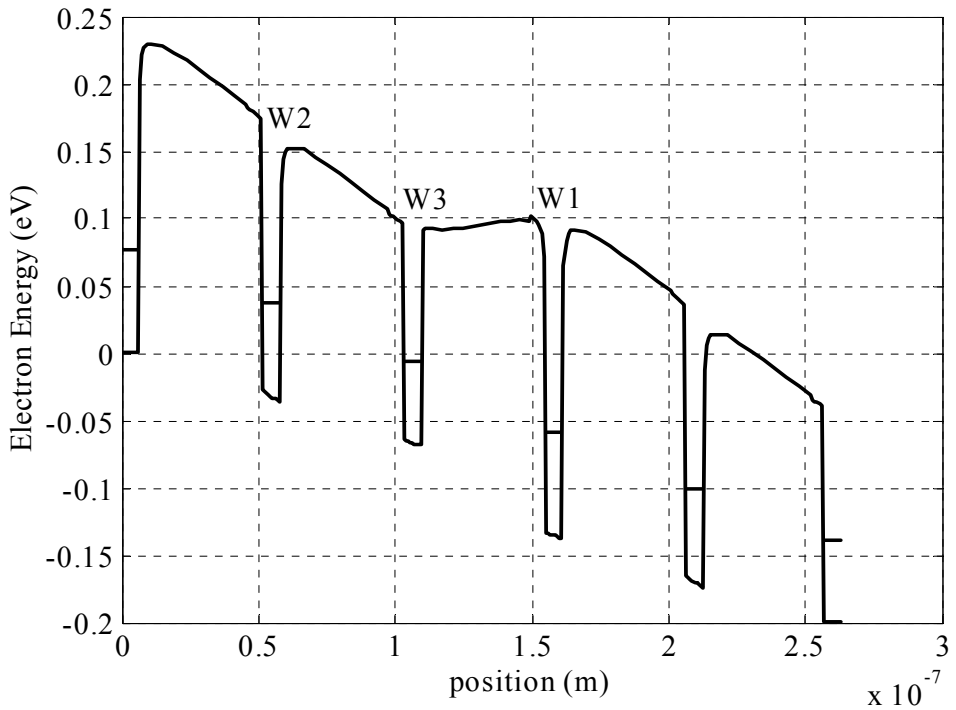

Figure 34 Energy band diagram of Device 1 at 82.1 K and 21.1 μA.

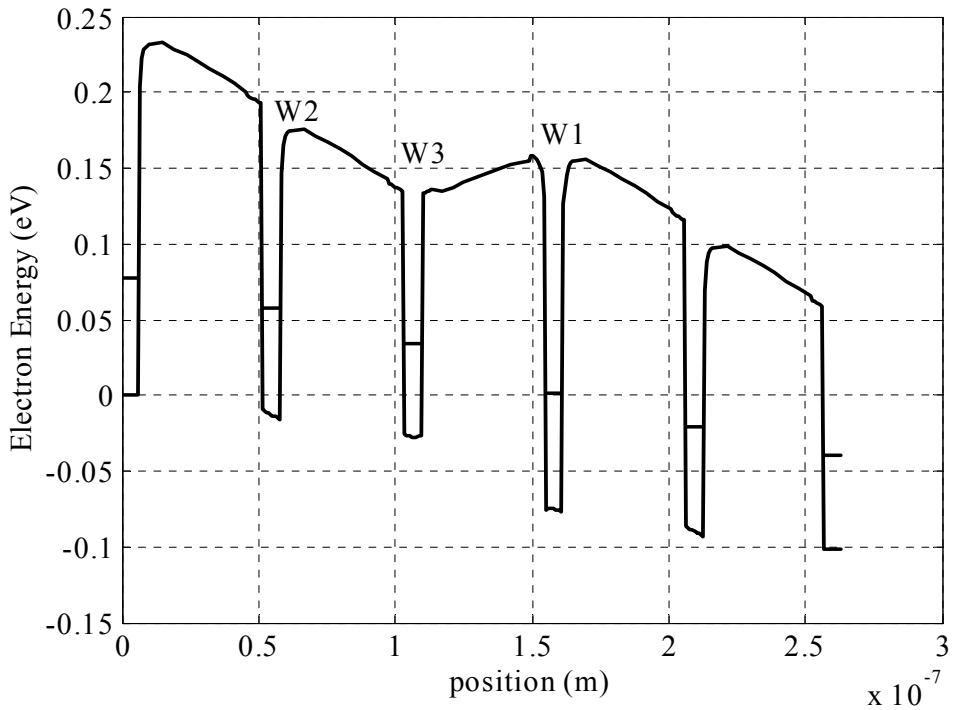

Figure 35 Energy band diagram of Device 1 at 91.7 K and 26.8 μA.

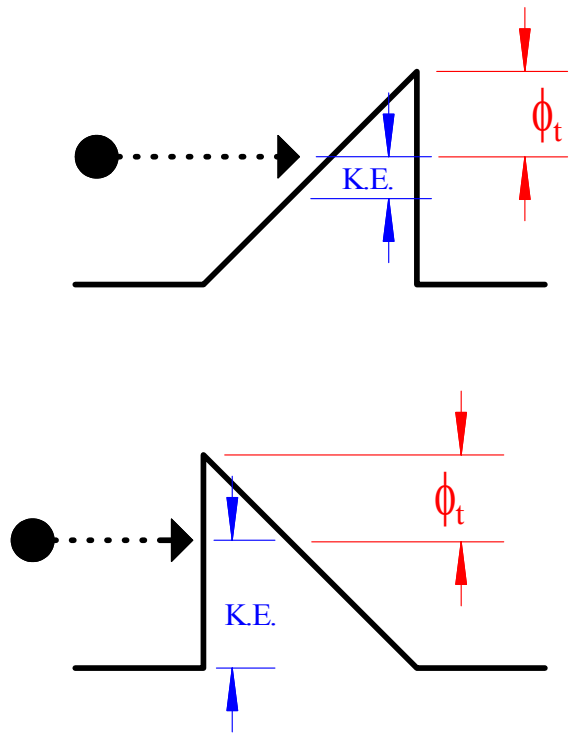

Figure 36 Electron approaching a 1D triangular barrier from both sides.

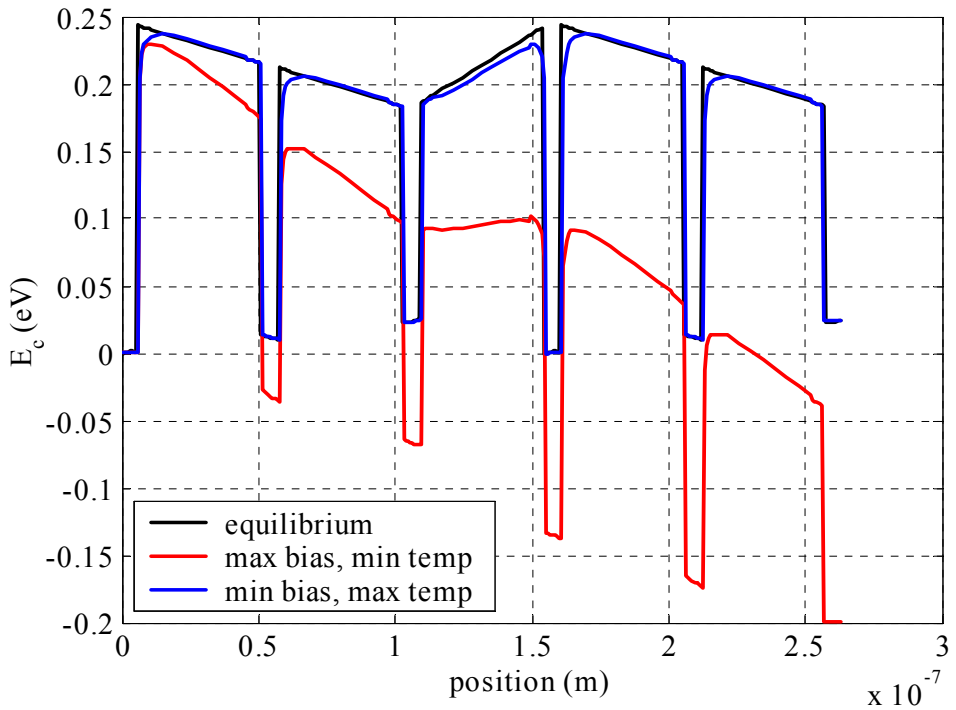

Figure 37 Comparison of the energy band diagram of Device 1 at equilibrium and extreme bias cases.

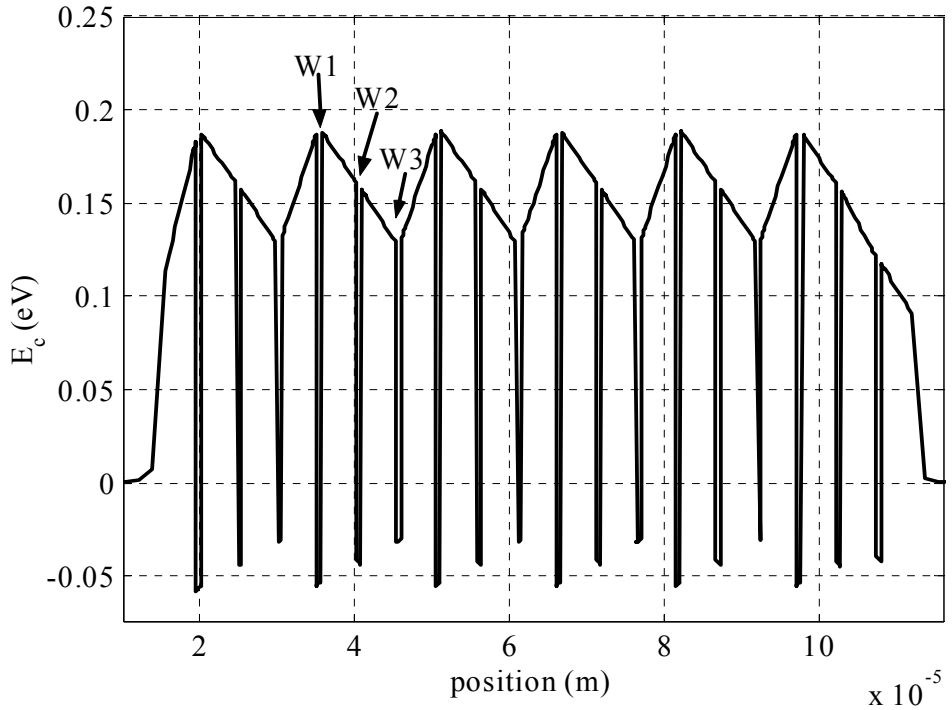

Figure 38 Energy band diagram for six periods of Device 1 at equilibrium.

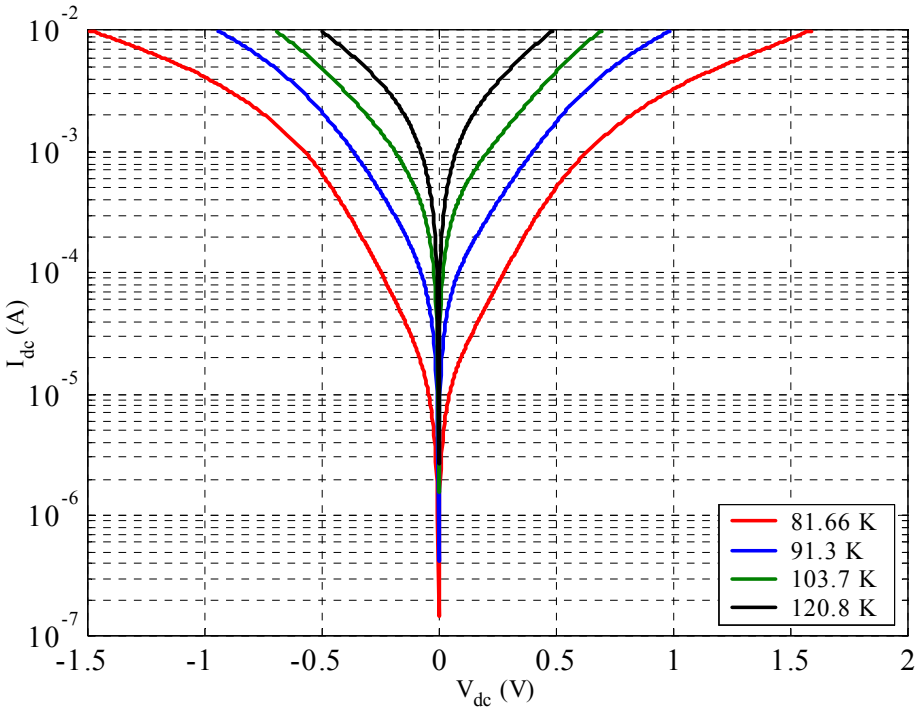

Figure 39 Device 2 IV characteristic at four temperatures.

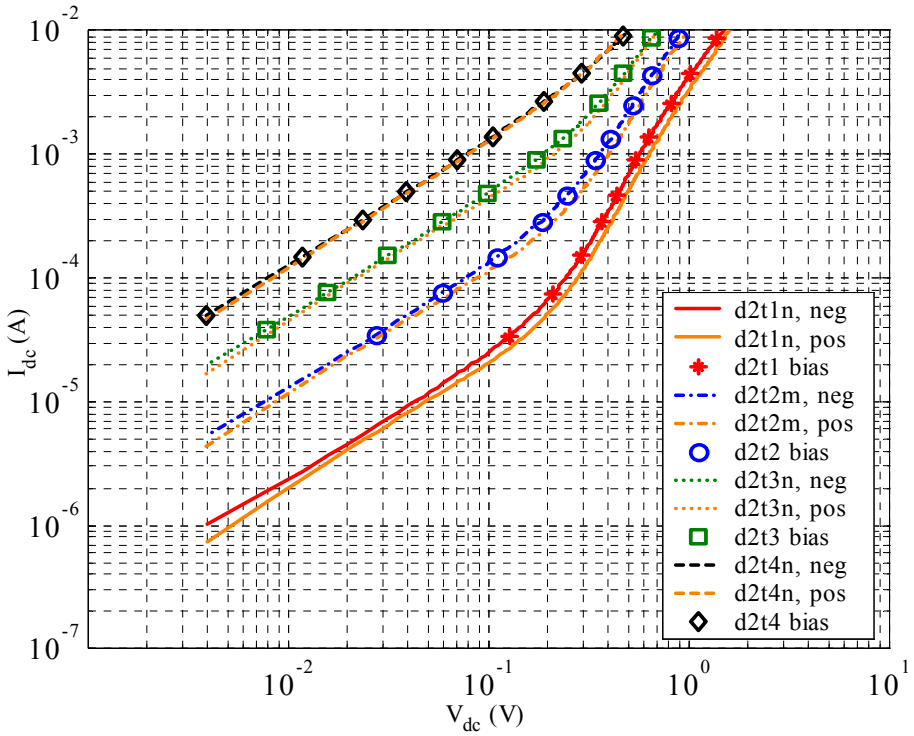

Figure 40 Device 2 double log IV characteristic at four temperatures with noise measurement biases.

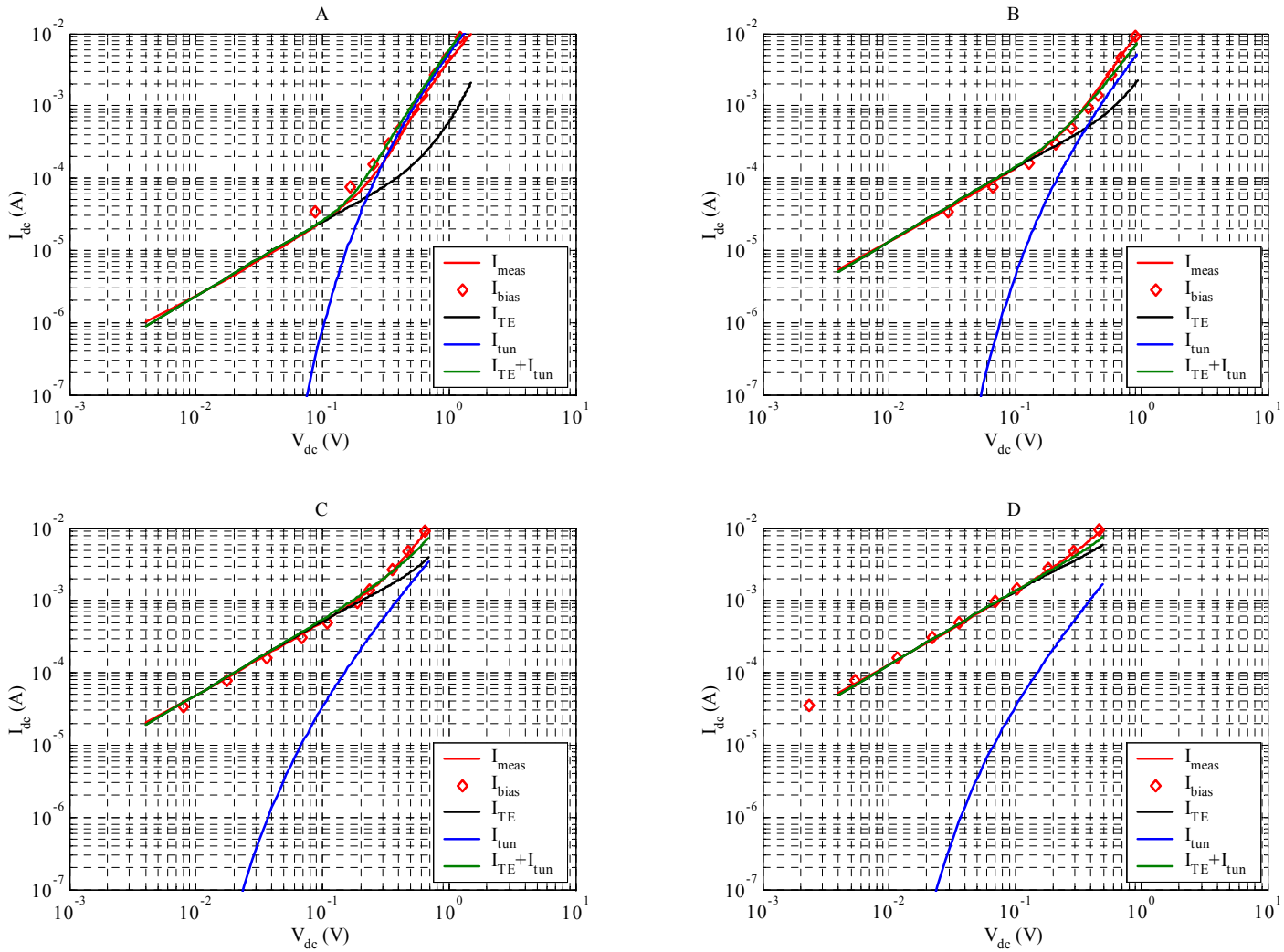

Figure 41 Device 2 measured and modeled IV characteristic at four temperatures. A) 81.66 K B) 91.3 K C) 103.7 K D) 120.8 K.

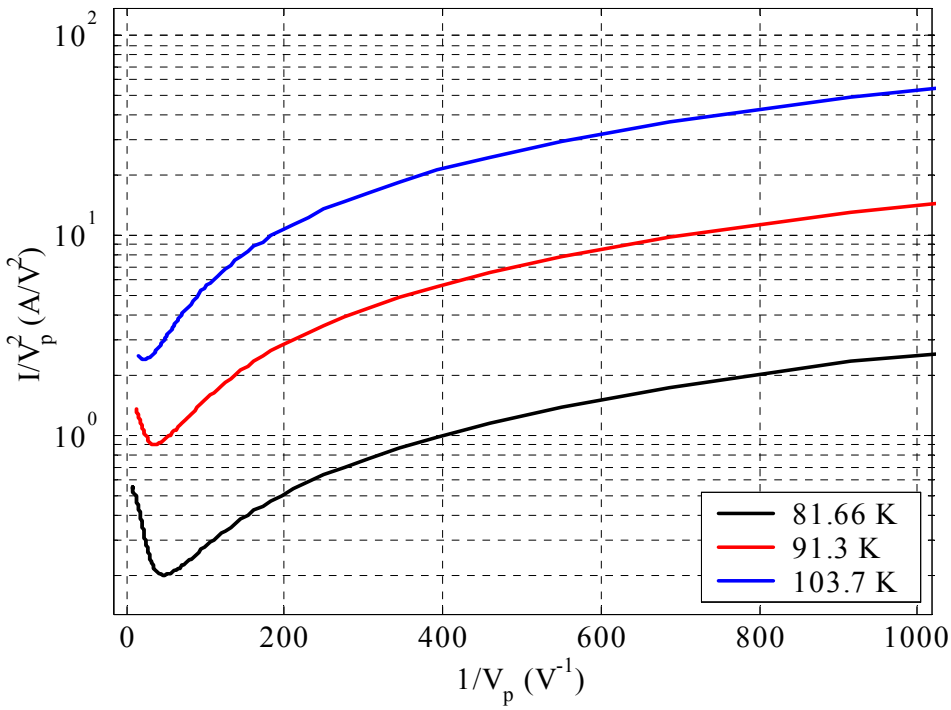

Figure 42 Device 2 Fowler-Nordheim plot of three temperatures, broad view.

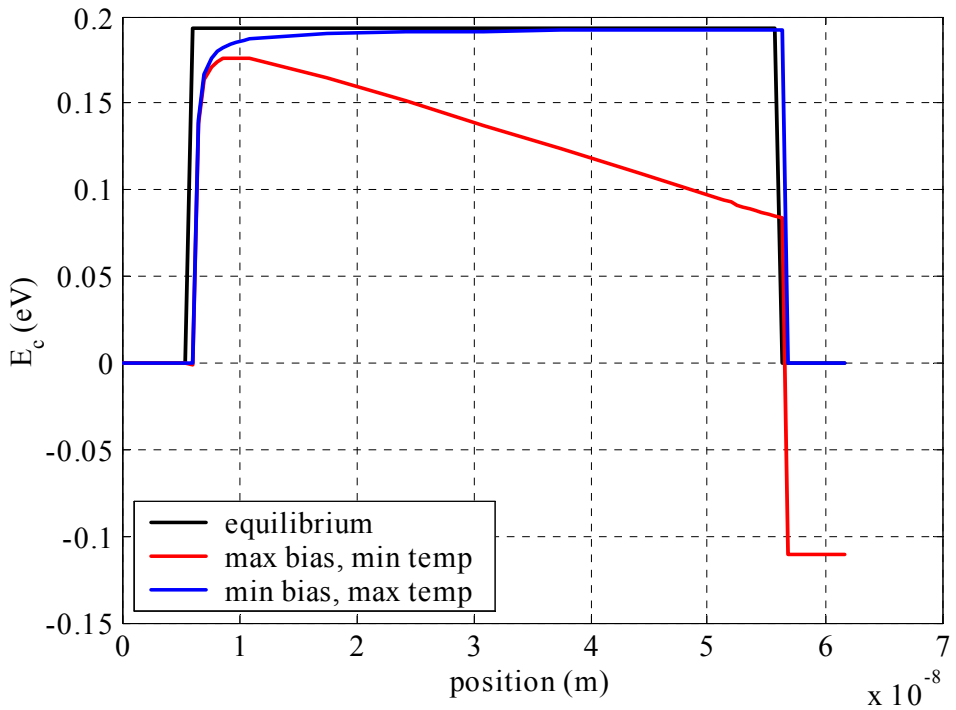

Figure 43 Comparison of the energy band diagram of Device 2 at equilibrium and extreme bias cases.

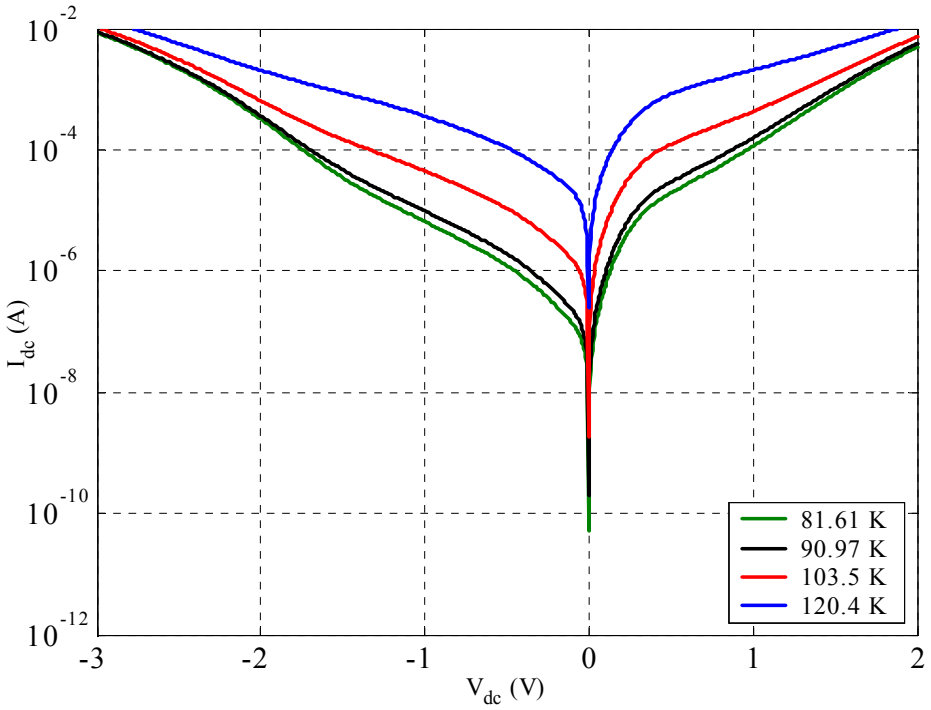

Figure 44 Device 3 IV characteristic at four temperatures.

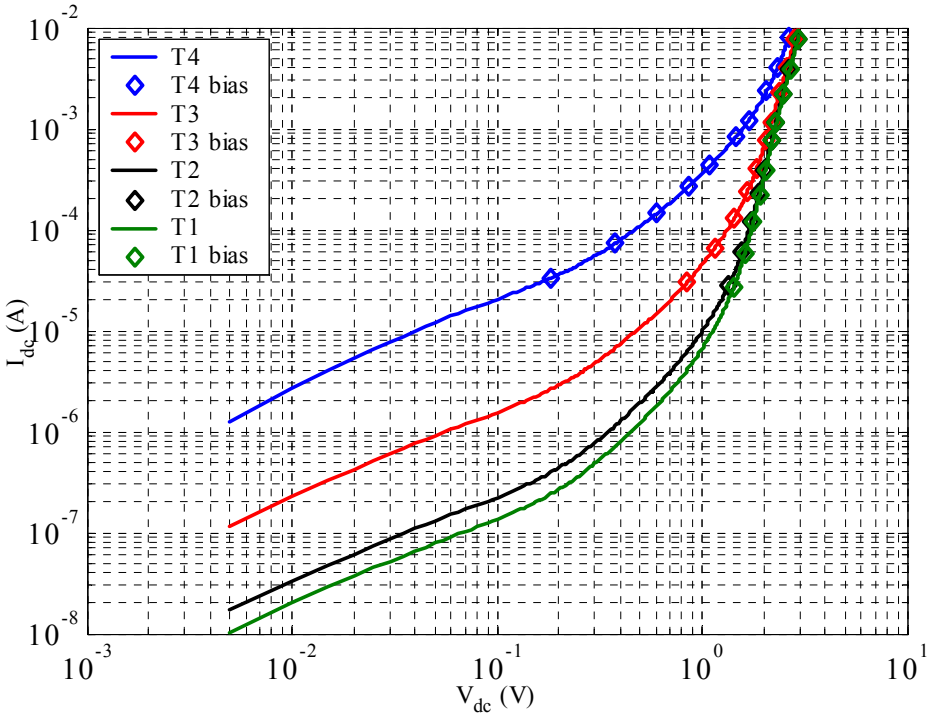

Figure 45 Device 3 double log IV characteristic at four temperatures with noise measurement biases.

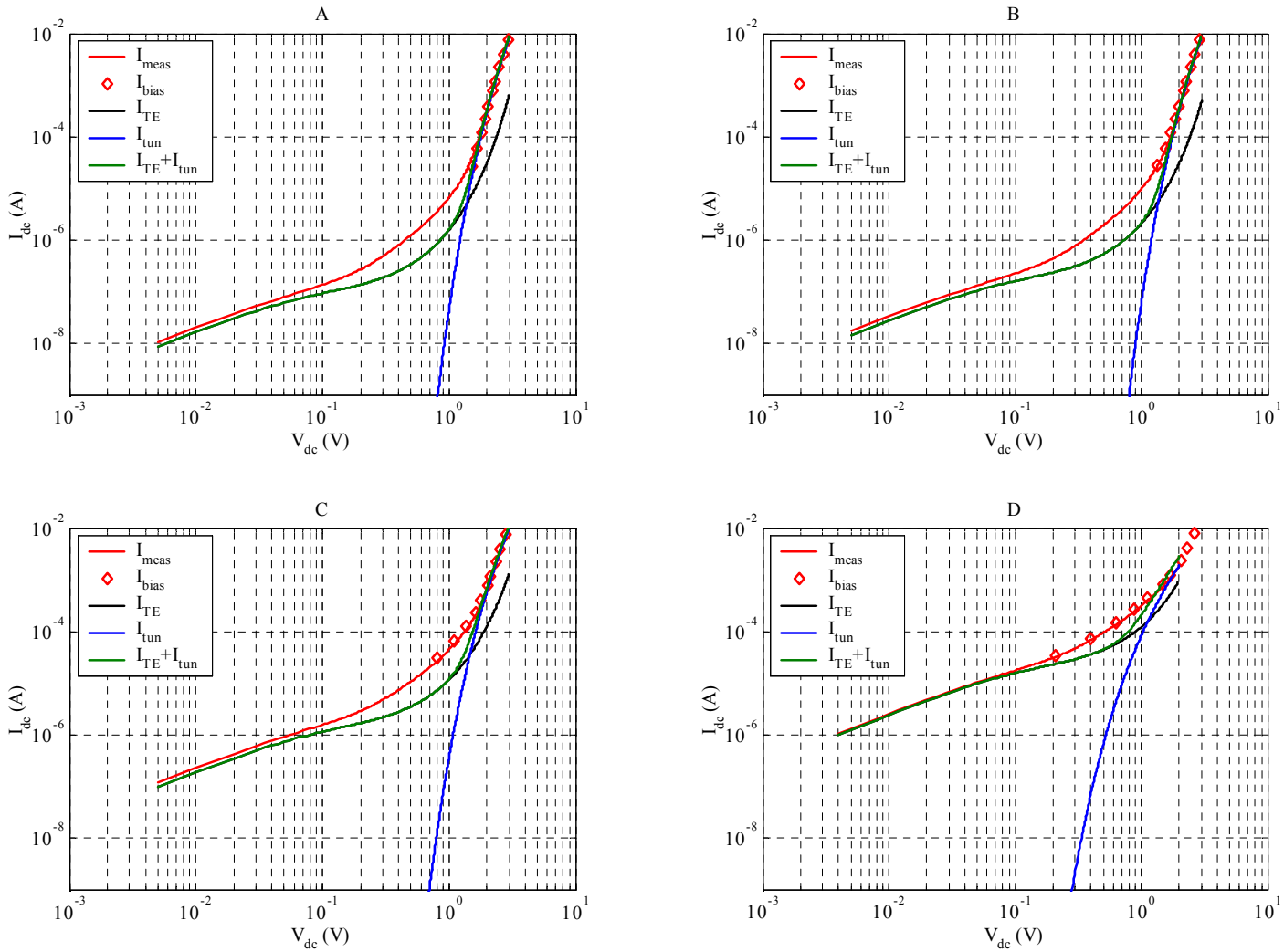

Figure 46 Device 3 measured and modeled IV characteristic at four temperatures. A)81.61 K B) 90.97 K C) 103.5 K D) 120.4 K.

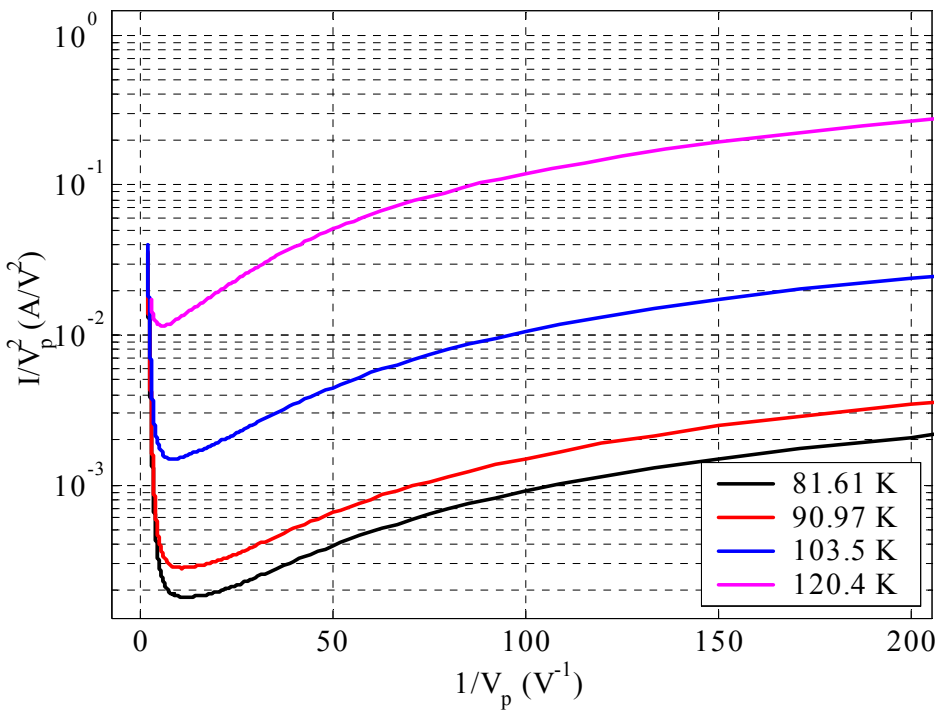

Figure 47 Device 3 Fowler-Nordheim plot of four temperatures, broad view.

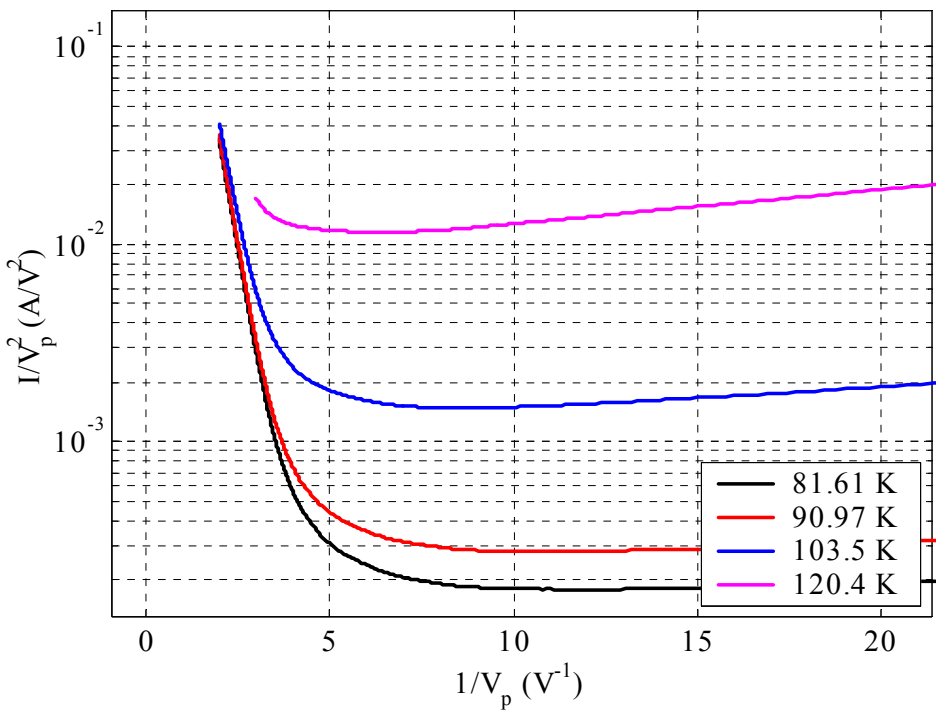

Figure 48 Device 3 Fowler-Nordheim plot of four temperatures, close up.

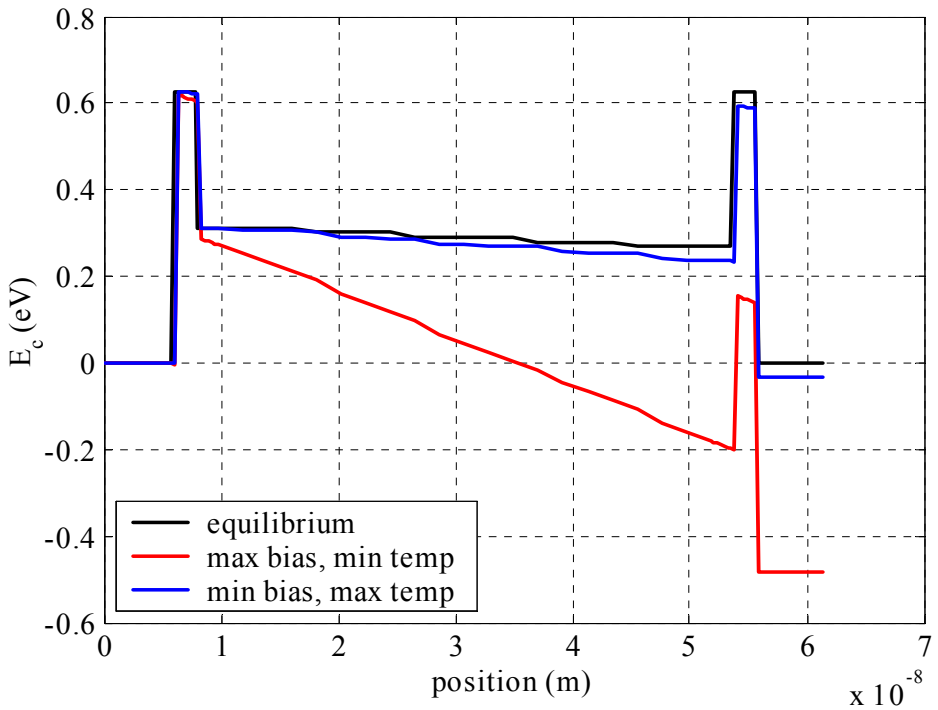

Figure 49 Comparison of the energy band diagram of Device 3 at equilibrium and extreme bias cases.

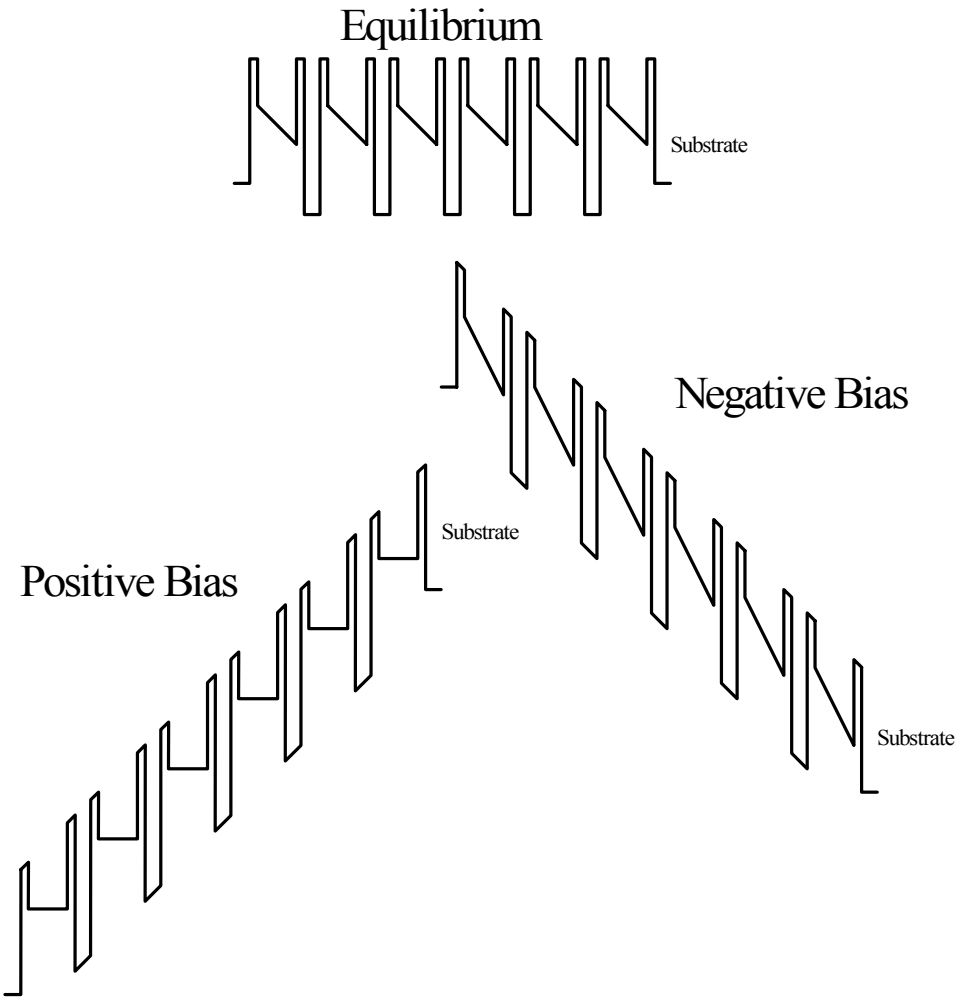

Figure 50 Stylized energy band diagrams for Device 3 at zero, negative, and positive bias.

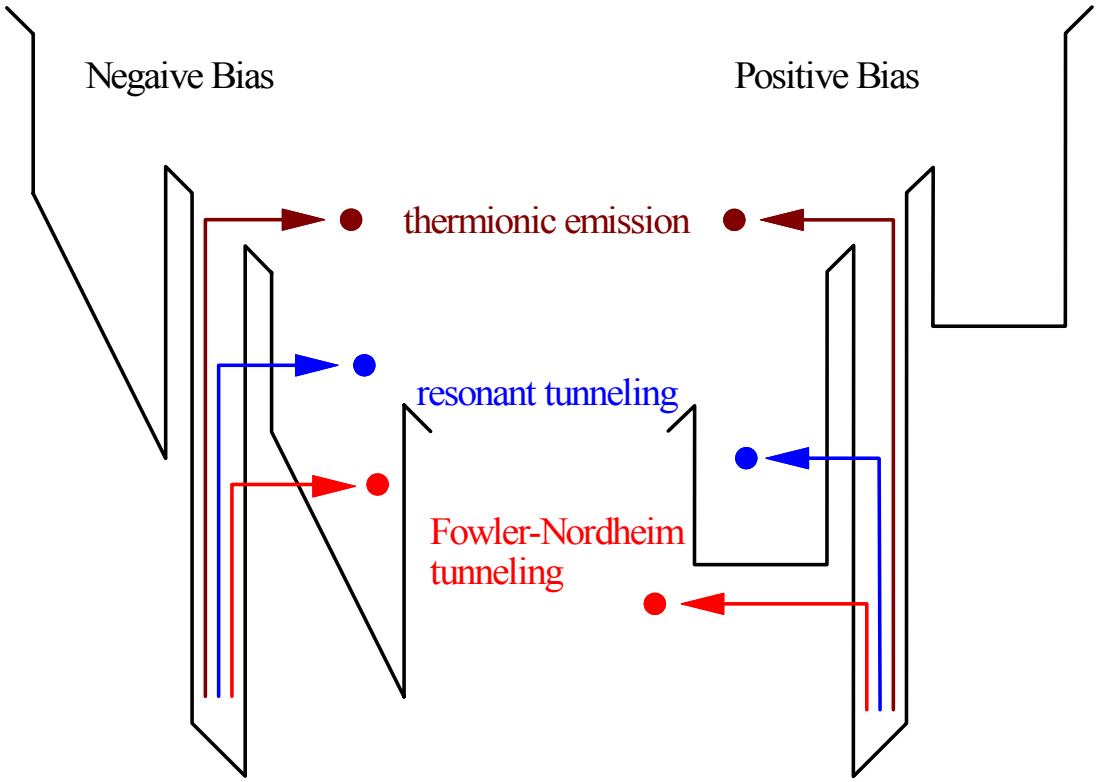

Figure 51 Three kinds of electron generation possible in Device 3 at negative and positive bias.

CHAPTER 5
NOISE

Noise takes on many forms in the world. Generally it is understood to be an unwanted phenomenon that impacts clarity. Its all-encompassing nature has created some terminology that is invariable across disciplines, such as 'white' noise. However, each discipline creates some terminology that is more specific to its ideology, such as 'shot' noise, and may contrive to change the meanings associated with the generally accepted terminology.

At its core, noise is a random collection of statistically independent events. In a concert hall noise may be defined by the presence of talking during a performance. In electronic circuits noise may be defined by the presence of a spurious signal from a known or unknown source. In semiconductor devices noise may be defined by the random change in numbers and types of charge carriers. Each of these examples arguably does not rigorously describe random events nor describe strictly independent events. However, to the extent that they are random and independent, they may each be studied and perhaps modeled using theories in stochastic processes and random variables.

Theory

General

Noise is a negative phenomenon that can be utilized for positive outcomes. Manifestation of noise varies with device bias, temperature, and frequency region of interest. As a result, knowledge of device operating parameters is important so that the analysis is focused in an applicable regime of operation. On the other hand, if the desired

result is modeling the device physics then analysis is required utilizing data from several operating conditions.

Theories exist for several types of noise found in semiconductor devices. They are primarily based on the device operating in a linear regime. This enables the use of simplifying assumptions that render the analysis tractable. However, some adaptation of existing theories is necessary to apply them to novel devices such as QWIPs.

The first step in the noise analysis is determining the operating parameters encountered during noise measurements. Then a determination must be made as to the type of noise observed as both a function of frequency, a function of temperature, and a function of bias. The most basic comparison is between thermal noise and measured noise as a function of frequency. If the device noise measurements are above that predicted by thermal noise, then the device is said to have excess noise. Excess noise comes in many forms including flicker (1/f or 1/f-like), generation-recombination (G-R), and shot noise. Each is believed to contribute to noise in a different physical manner. Though G-R, shot, and thermal noise physics are well known the same cannot be said of flicker noise. The latter has been theorized to come from different mechanisms or combinations of mechanisms with no consensus from one school of thought to another. Interestingly it is found in many processes throughout the physical world, not just in semiconductor devices or even electrical engineering.

Thermal Noise

Thermal noise is caused by the random motion of charge carriers which, in semiconductor devices, is observed as a fluctuating emf at its terminals. Thermal energy injected into the system causes particles to vibrate, resulting in random collisions between mobile charge carriers and the vibrating lattice atoms. Analysis of the resulting

noise may be approached as a diffusion problem, thus termed diffusion noise, or as a velocity fluctuation problem, termed velocity fluctuation noise [26]. In either case it is a fundamental limit to device operation. In other words, if all other noise sources could be completely eradicated thermal noise would still be there. Synonymous terms found throughout the literature are Johnson noise and Nyquist noise. Nyquist [27] formulated an equation to model the power spectral density of the voltage noise in a resistance as a function of temperature. Its modern equivalent is

$$S_v(f) = 4k_bTR \tag{5.1}$$

where S_v is the power spectral density of the voltage noise, f is frequency, k_b is Boltzmann's constant, T is temperature in Kelvin, and R is the resistance. The equivalent expression for the power spectral density of the current noise, S_i, is

$$S_i(f) = \frac{4k_bT}{R} \tag{5.2}$$

where all the variables on the right hand side have the same meaning as stated previously.

All semiconductor devices have thermal noise, as do most other devices. Whether or to what extent it will affect device operation is dependent on the device, its temperature, its bias point, the frequency range considered, and the presence or absence of other noise sources. At low frequencies thermal noise may be overshadowed by other noise, such as flicker noise and generation-recombination noise. At very high frequencies thermal noise rolls off due to the frequency dependence of the diffusion constant. The roll-off typically occurs well above the operating frequency for many devices.

Analysis of thermal noise as diffusion noise begins with modeling the semiconductor as a contiguous group of rectangular boxes with dimensions Δx, Δy, and

Δz. Collisions enable the charge carrier to randomly jump from one box to another and are considered as independent events. Solving for the probability that an electron will change boxes during a time interval Δt, van der Ziel [26] shows that the power spectral density of the noise in the particle current, S_n, is

$$S_n(f) = 4D_n n(x)\frac{\Delta y \Delta z}{\Delta x} \tag{5.3}$$

where f is the frequency, D_n is the electron diffusion constant, and $n(x)$ is the electron concentration. This converts to the power spectral density of the noise in the electrical current by including the charge associated with each carrier, q.

$$S_i(f) = q^2 S_n(f) = 4q^2 D_n n(x)\frac{\Delta y \Delta z}{\Delta x} \tag{5.4}$$

In order to reduce this result for diffusion noise to that of thermal noise, Einstein's relation must be valid.

$$qD_n = k_b T \mu_n \tag{5.5}$$

Where q is the magnitude of the electric charge, D_n is the diffusion constant for electrons, k_b is Boltzmann's constant, T is temperature in Kelvin, and μ_n is the low field electron mobility. The current noise spectral density may then be expressed as

$$S_i(f) = 4k_b T\left[q\mu_n n(x)\right]\frac{\Delta y \Delta z}{\Delta x} = \frac{4kT}{\Delta R} \tag{5.6}$$

where ΔR is the differential resistance. Thus, diffusion noise is reduced to thermal noise by replacing the DC resistance with the differential resistance. This has no effect on the result unless the device does not exhibit a linear current-voltage characteristic. In that case, as with QWIPs, the operating bias point will affect the thermal noise characteristics of the device via the differential resistance.

Shot Noise

The mechanism of shot noise is the independent and random crossing of potential energy barriers by charge carriers. In the frequency domain, shot noise, like thermal noise, is independent of frequency. There are two main differences between shot noise and thermal noise, the former requires a DC current and is independent of temperature whereas the latter is independent of current and directly proportional to temperature. The reason for these differences is the origin of the carriers.

Shot noise results because the carriers are randomly 'emitted' from a potential barrier then 'swept' into the continuum, adding to the total number of carriers moving through the device. The random crossing of the barrier results in the random arrival of those carriers at the contact. Without current there would be no 'sweeping' of the carriers out to the contact, thus no fluctuation in the current or voltage. In equation form shot noise is

$$S_i(f) = 2q\bar{I} \tag{5.7}$$

where q is the magnitude of the electric charge and $\bar{I}$ is the DC current.

Manifestation of shot noise in a device is indicative that there is at least one source of random injection of carriers through a potential barrier, as for instance at the metal-semiconductor interface of a Schottky barrier diode. The nature of QWIPs all but promises the existence of potential barriers that could result in shot noise. Unfortunately that prediction was not born out in the data.

Generation-Recombination Noise

Generation-recombination (G-R) noise is so called because of the underlying physics. A charge carrier is generated or it recombines. These events may be band-to-

band, to and from a trap or recombination center, or to and from an impurity center. In the QWIPs under study band-to-band events and recombination centers are highly unlikely so will not be considered. Each event changes the number of charge carriers within the system at any given time. Typically these events are outside the preferred current contributing path, therefore are considered noise. The statistics of these events include the time each carrier spends either trapped or in the continuum and the number of sites available. G-R noise manifests as a Lorentzian spectrum in frequency with the corner frequency representative of the time constant for the generation and recombination events.

The extent to which a trap, or impurity, center will be active depends on its proximity in energy to the quasi-Fermi energy level. If the center is too far above the quasi-Fermi energy it will always be empty therefore have no carriers to contribute to the continuum. Conversely, if the center is too far below the quasi-Fermi energy it will always be full. This condition also obviates contribution to the continuum. The same reasoning results in the conclusion that the trap will be the most active when the quasi-Fermi energy coincides with the trap energy level. This also suggests that if there are traps at different energy levels, they could be isolated by manipulating the quasi-Fermi energy.

The power spectral density of the noise in the particle number, S_N, is

$$S_N(f) = \overline{4\Delta N^2}\,\frac{\tau}{1+\omega^2\tau^2} \tag{5.8}$$

where τ is the lifetime of the carriers, N is the number of carriers, and $\overline{\Delta N^2}$ is the variance of N [26]. The key to using this equation is determining the variance of N and

the carrier lifetime τ in terms of known parameters. One such determination [26] results in

$$\tau = \frac{1}{r'(N_0) - g'(N_0)} \tag{5.9}$$

where the primes denote derivatives, r is the recombination rate, g is the generation rate, and N_0 is the most probable value of N and in

$$\overline{\Delta N^2} = g_0 \tau \tag{5.10}$$

where g_0 is the equilibrium generation rate. Making the appropriate substitutions, the power spectral density of the noise in the particle number is

$$S_N(f) = 4g_0 \frac{\tau^2}{1+\omega^2\tau^2} \tag{5.11}$$

where all variables are as described previously. These equations take on many forms according to the particular semiconductor parameters such as dopant energy levels and concentrations.

Flicker Noise

Flicker noise is characterized by its *1/f* or *1/f*-like frequency dependence. To date no single theory has been accepted as to the physics behind it or how to model it. This is unfortunate as the lack of definitive knowledge hinders attempts to reduce *1/f* noise in device design. One prevailing theory asserts that it is due to a continuous distribution of time constants in the GR sense [26]. As well, flicker noise has been postulated to emanate from either or both number fluctuations and mobility fluctuations. For a resistor, van der Ziel [26] derives a theoretical model of *1/f* noise based on both number fluctuations and mobility fluctuations. If the two sources of fluctuation are independent

then the normalized voltage noise is equal to the sum of the normalized number fluctuation noise and the normalized mobility fluctuation noise.

$$\frac{S_v(f)}{\left(\overline{V}\right)^2} = \frac{S_N(f)}{\left(\overline{N}\right)^2} + \frac{S_\mu(f)}{\left(\overline{\mu}\right)^2} \tag{5.12}$$

This allows for the possibility of one mechanism dominating the other. Given that separate equations can be derived to describe each mechanism, the source of the dominant noise in any particular device may be obtained. The form of each equation is

$$\frac{S_v(f)}{\left(\overline{V}\right)^2} = \frac{S_I(f)}{\left(\overline{I}\right)^2} = \frac{\alpha}{f\overline{N}} \tag{5.13}$$

where the interpretation of α depends on whether a description of number fluctuation noise or mobility fluctuation noise is sought. This same form was postulated by Hooge [28] with α replaced by α_H and called the Hooge parameter. When it was first proposed the Hooge parameter was believed to be a universal dimensionless constant with a value of to $2 \cdot 10^{-3}$. It has since been shown to vary widely with device geometry and material.

Experimental Data

Device I

A look at the IV characteristics for D1 in Figure 52 shows which noise measurements were taken within a linear regime of operation. The two lowest temperatures, 82.1 K and 91.7 K, are definitely in the non-linear regime. With the possible exception of one bias at 104.15 K, the remainder of the noise measurements were taken while the device was operating in the linear regime. Interestingly, the amount of excess noise is at its maximum for the higher temperatures. The current noise spectral density is plotted as a function of frequency for each temperature in Figure 53 and Figure

54. The two middle temperatures are duplicated to better observe the transition. In these graphs each data set within a graph represents a single bias point. The diamonds are the measured data and the circles are the predicted thermal noise at the dynamic resistance value calculated for that bias point. The actual bias values at each temperature are associated with labels and presented in Table 19. B0 means no bias was applied.

Table 19 Bias currents at each temperature for D1 (μA).

	82.1 K	91.7 K	104.15 K	121.2 K	144.3 K	179.8 K
B1	1.192	1.349	1.500	1.517	1.481	1.486
B2	3.281	3.843	4.399	4.468	4.373	4.384
B3	8.851	10.73	12.02	13.11	12.88	12.92
B4	21.10	26.82	29.71	34.37	33.99	34.15

As the temperature increases the dynamic resistance values, and therefore the predicted thermal noise, become less variable with bias, i.e., the device is operating in the linear regime. Unfortunately reliable noise data were not obtained above 1 kHz so analysis using thermal noise was impossible at the highest four temperatures. At 82.1 K and 91.7 K at least one data set enters the thermal regime, which is where the noise becomes independent of frequency. Although the noise becomes independent of frequency there is still excess noise above that predicted by thermal noise.

Beginning with 82.1 K and focusing on the high frequency part of Figure 53A it is observed that at each bias there is a portion of frequency independence. This may represent the onset of the diffusion regime. Since there are no data from higher frequencies, it is unclear whether this plateau is in fact onset of the diffusion regime or part of a Lorentzian with a time constant shorter than 160 μs. Looking at the frequency range up to 100 Hz, the measured noise at B1 appears to be *1/f* in nature. In the same frequency range, the measured noise at B2 may be showing Lorentzian characteristics. A pure Lorentzian has a roll-off proportional to f^{2}. Using 7 Hz as the peak, this would

represent a time constant of about 23 ms. The same argument would hold for B4 resulting in the same time constant. The data from B3 have a negative slope less than f^{1} but the lowest frequencies cannot be interpreted as concave down.

The next higher temperature, 91.7 K, is shown in Figure 53B. In the highest decade of frequencies only the data measured at B1 exhibit behavior representative of the onset of frequency independence. In addition, there is a possible Lorentzian peak beginning around 40 Hz and continuing until the flattening begins at about 250 Hz. Each of the next two biases appear to be descending as one would expect on the high frequency side of a Lorentzian. At the high frequencies of B4 the values may be descending or they may be representative of a portion of f^{1} dependence. (Since the latter is unlikely, there is a strong possibility that a Lorentzian is represented.) If in fact a single Lorentzian is represented in each of the first three biases, their respective time constants are approximately 0.88 ms, 0.44 ms, and 0.796 ms. For B4, there are potentially three time constants represented, 7.96 ms, 2.12 ms, and 0.398 ms. In the lower two decades of frequencies B1 shows f^{1} dependence, B2, B3, and B4 have a negative slope without the concave down portion as seen at 82.1 K.

Proceeding on to 104.15 K in Figure 53C, each non-zero bias at low frequencies shows a negative slope between f^{1} and f^{2} until about 100 Hz. While B1 shows variation, the trend continues up to 1 kHz. At about 400 Hz B2, B3, and B4 all appear to change slope, which would represent a change to $1/f$ dependence. Possibilities for this progression in frequency dependence would include very low frequency G-R events that dominate even the flicker noise until about 400 Hz and an overlap in two low frequency

G-R events. A more extensive frequency picture would be required to make a definitive determination.

Figure 53D is the current noise spectral density data at 121.2 K. At this temperature each of the first three biases appear to have a G-R peak at about 20 Hz. For the highest bias the peak looks to be at its maximum closer to 40 Hz. These would represent time constants of 7.97 ms and 3.98 ms, respectively. It is unlikely that the dependence at low frequencies is *1/f* since it is followed by a negative slope between f^{1} and f^{2}.

The next higher temperature, 144.3 K is shown in Figure 54C. Each of the four biases begin with a portion that is concave down. It could be argued that there is a time constant similar to that of the previous temperature at about 7.97 ms. Above about 30 Hz the three higher biases appear to show *1/f* frequency dependence. It appears that B1 may contain two more G-R peaks at about 100 Hz and 500 Hz. These would correspond to time constants of about 1.59 ms and 0.318 ms, respectively. For 179.8 K, shown in Figure 54D, all four biases appear to have about the same slope. The frequency dependence of the data was calculated and resulted in about $f^{0.78}$, slightly less than *1/f*. In each of the four bias data sets there appears to be two features. One of them is at about 40 Hz and the other at about 700 Hz. These would correspond to time constants of 3.98 ms and 0.227 ms, respectively. A summary of the time constants potentially represented in the current noise spectral density data is given in Table 20. In the time domain, D1 exhibited random telegraph signal (RTS) at temperatures between 115 K and 135 K. Analysis of that phenomenon is presented in chapter 8 of this work.

Table 20 Time constants (ms) at each temperature and bias for D1. X means that no Lorentzian was observed.

	82.1 K	91.7 K	104.15 K	121.2 K	144.3 K	179.8 K
B1	X	0.88	X	7.97	7.97, 1.59, 0.318	3.98, 0.227
B2	23	0.44	X	7.97	7.97	3.98, 0.227
B3	X	0.796	X	7.97	7.97	3.98, 0.227
B4	23	7.96, 2.12, 0.398	X	3.98	7.97	3.98, 0.227

Device II

For this device noise spectra were measured at 11 biases for each of four temperatures. The actual bias values at each temperature are associated with labels and presented in Table 21. B0 means no bias was applied. Figure 55 shows the relationship between the noise measurement bias points and the IV characteristic. For none of the temperatures do all of the noise measurement bias points reside in the linear regime of operation. The two higher temperatures, 103.7 K and 120.8 K, contain the most linear bias points. For 81.66 K the lowest non-zero bias is at the edge of the linear regime and for 91.3 K the three lowest non-zero bias points are in the linear regime.

Table 21 Bias currents at each temperature for D2 (μA).

	81.66 K	91.3 K	103.7 K	120.8 K
B4	33.94	34.37	34.59	34.63
B5	74.91	76.31	77.03	77.09
B6	154.8	158.3	160.7	161.0
B7	292.7	299.7	306.2	307.5
B8	476.7	486.5	496.2	498.7
B9	916.5	936.0	952.6	960.0
B10	1388	1386	1411	1437
B11	2654	2659	2701	2756
B12	4621	4652	4727	4824
B13	8972	9113	9280	9466

Current noise spectral density data are shown in Figure 56 and Figure 57. For clarity, each temperature is represented by two graphs. Again, the diamonds are the data and the circles are the thermal noise associated with the dynamic resistance at each bias

point. The difference in the size of the frequency vectors between the first six biases and the last four biases represent two passes of data gathering. It was decided that higher bias noise measurements were required after initial perusal of the first pass. The extended frequency range allowed more extensive analysis on the diffusion noise regime.

At 81.66 K, Figure 56A and Figure 56B, predicted thermal noise consistently underestimates the measured high frequency noise at non-zero bias, i.e., there is excess noise which potentially contains extractable information. Increasing the temperature to 91.3 K, Figure 56C and Figure 56D, shows the same trend except at B4 (the lowest bias) where the measured noise coincides with the zero bias value. A further increase in temperature to 103.7 K, Figure 57A and Figure 57B, collapses the measured data of the first three non-zero biases onto the zero bias data. In other words, the device is exhibiting only predicted thermal noise at low bias and high frequency. Finally, at 120.8 K, Figure 57C and Figure 57D, the high frequency noise approaches the zero-bias value for the first six non-zero biases. In addition, at the highest four biases the relative amount of excess noise is reduced from that observed at lower temperatures.

Utilizing graphs of the D2 noise data in the diagnostic configuration $f \cdot S_i$ versus f for 81.66 K through 120.8 K, respectively, the following were observed. At 81.66 K from about 200 Hz up to the maximum measured for all biases, the spectra exhibit frequency independence as predicted by the G-R excess noise plateau. Between 20 Hz and 200 Hz there is no deviation from the high frequency until B8. From there up to B13 there appears to be a transition region exhibiting close to *1/f* dependence. A similar trend is observed at 91.3 K with the sole exception that the *1/f* transition does not clearly begin until B9. At 103.7 K the *1/f* dependence is clearer and continues to higher frequencies,

especially at the higher biases. The transition to frequency independence begins closer to 500 Hz for the top three bias values. In addition, there appears to be some *1/f* dependence in B7 and B8 at the lower three frequencies measured. Again beginning with B7 and continuing to B13, there appears to be some *1/f* dependence at lower frequencies at 120.8 K. At this temperature, however, the transition to frequency independence does not begin until close to 1 kHz for the top three biases. In contrast to D1, there do not appear to be any other artifacts that would be of predictive value in D2. This is not surprising since D2 is the simplest of the three devices, both in geometry and materials.

Device III

Shown in Figure 58 is the double logarithmic representation of the negative quadrant of the IV characteristic for D3 with the noise measurement bias data points superimposed. The actual bias values at each temperature are associated with labels and presented in Table 22. B0 means no bias was applied. Unlike the other two devices, nearly all of the noise measurements were done at bias values within the non-linear regime of operation. In fact, there is only a narrow range of biases near zero at which the device can be said to be operating linearly. This may make the application of the popular noise analysis techniques inappropriate, except perhaps for comparisons with theory. Again for clarity, each group of temperature data is divided into two graphs, B0 through B9 and B10 through B13.

The graphs in Figure 59 and Figure 60 plot the measured noise spectra for D3. Of note is that with the exception of at 120.4 K the calculated dynamic resistance does not predict the zero bias noise magnitude.

At 81.61 K, shown in Figure 59A and Figure 59B, there are a couple of other features to note. All non-zero biases have a negative slope at lower frequencies that tends

toward frequency independence at higher frequencies. B4, B5, and B13 are somewhat different with the first two appearing to begin to roll off at about 60 kHz and the last one not definitively exhibiting frequency independence. In addition, the predicted thermal noise is well below the measured high frequency noise for all biases.

Table 22 Bias currents at each temperature for D3 (μA).

	81.61 K	90.97 K	103.5 K	120.4 K
B4	26.93	27.91	30.40	33.34
B5	58.40	59.85	64.69	72.36
B6	119.1	121.2	128.9	146.2
B7	222.7	225.7	236.5	268.9
B8	384.6	387.4	398.3	437.2
B9	763.5	767.0	780.3	830.1
B10	1150	1155	1171	1227
B11	2238	2245	2269	2336
B12	3911	3923	3959	4048
B13	7655	7670	7732	7868

Measurements taken at 90.97 K, Figure 59C and Figure 59D, show the same characteristics. The only exception of note is that B5 is no longer exhibiting a roll off in frequency near 60 kHz and the roll off at B4 begins nearer 40 kHz. In addition to the trends seen at cooler temperatures, some new features begin to appear with the measurements taken at 103.5 K, shown in Figure 60A and Figure 60B. First, the frequency roll off beginning at about 40 kHz is noticeable in the data from B4, B5, and B6. Next, B8 through B11 appear to have what could be a Lorentzian artifact below 1 kHz. Also, B4 and B5 do not exhibit the low frequency negative slope. Finally, the predicted thermal noise is above the measured noise at zero bias. Measured noise data at 120.4 K, Figure 60C and Figure 60D, also exhibit the trends noted for the data at 81.61 K with a couple of exceptions. Similar to 103.5 K, the low frequency negative slope is not evident at B4 and B5. With the possible exception of B11, there does not appear to be any Lorentzian behavior at any bias.

Utilizing the $f \cdot S_i$ perspective of the data, not shown, stronger arguments may be made regarding some of the observations above. Beginning with 81.61 K a migration of the corner frequency with increased bias is noted, from about 70 Hz to about 3 kHz. Once B13 is reached the low frequency behavior is approaching a *1/f* dependence. At the lower biases the dependence consistently appears to be approximately $f^{0.5}$ up to the corner frequency. Above the corner frequency for all biases there appears to be frequency independence, with the exceptions that B4 and B5 begin to turn down at 100 kHz.

At 90.97 K there is a similar trend as that noted for 81.61 K. The transition frequency is at its lowest at B4, at about 50 Hz. For B5 and B6 it appears to be about 400 Hz and for B7-B12 it is about 2 kHz. B13 shows an approximately *1/f* dependence up to about 4 kHz. After the transition B5-B13 all appear to approach frequency independence. B4 exhibits the turn down similar to that at 81.61 K with the transition being at about 50 kHz. Unlike the behavior noted at 81.61 K, there appear to be artifacts in the data at 90.97 K. B5, B7, and B11 have a potentially concave down artifact at about 45 Hz which equates to a time constant of 3.54 ms. B10 has a lot of variation at low frequencies which may be overlap of three separate GR peaks. The lowest would be below the lowest frequency measured, the next would be at about 80 Hz, and the last would be at about 450 Hz. These correspond with time constants of 1.99 ms and 0.354 ms, respectively. Finally, B12 appears to have a GR peak at about 450 Hz as well.

At 103.5 K frequency independent behavior is noted for B4-B6 at all frequencies up to 40 kHz. At low frequencies B7 is approximately *1/f* with two potential GR peaks, one at about 80 Hz and the other at about 450 Hz. The second appears to be swamped by

the beginning of the frequency independent region just below 1 kHz. B8 through B13 show GR peaks below 1 kHz. B10, B11, and B13 have what could be an additional GR peak between 1 kHz and 10 kHz. At B8 the peak appears to be at its maximum at about 200 Hz, corresponding to 0.796 ms. At B9 the maximum appears to be at about 450 Hz, corresponding to 0.354 ms. At B10-B13 the maximum appears to be at about 300 Hz, corresponding to 0.531 ms. For the three biases with a second GR peak, the maximum appears to be at about 4.5 kHz for B10 and B11 and at about 2.5 kHz for B13. These frequencies correspond to 35.4 μs and 63.7 μs, respectively. With the exception of B13, there appears to be frequency independence at all the higher frequencies measured. B13 begins a turn down at 63 kHz.

Finally, at 120.4 K there are essentially no frequency characteristics of note until B8. B4-B7 show a primarily frequency independent behavior at all frequencies. B6 and B7 appear to be in a transition region at low frequencies, however. At B8 there is *1/f* behavior until about 100 Hz where the frequency dependence ends. At B9 the *1/f* behavior continues until about 400 Hz. At B10 and B11 the transition frequency is about 1 kHz. Also at B10 a potential GR peak appears at about 800 Hz, corresponding to 0.199 ms. At B11 the GR peak is at about 450 Hz, corresponding to 0.354 ms. At B12 there appear to be two GR peaks, one at about 1.5 kHz and the other at about 8 kHz, and the transition to frequency independence is at about 25 kHz. The corresponding time constants for the GR peaks are 0.106 ms and 19.9 μs, respectively. At B13 the lower frequencies also show *1/f* behavior with potentially two GR peaks at 2.5 kHz and 8 kHz. Their respective time constants are 63.7 μs and 19.9 μs. The transition frequency appears

to be at about 15 kHz. The time constants approximated for D3 are consolidated into Table 23.

Table 23 Time constants (ms) at each temperature and bias for D3. X means that no Lorentzian was observed.

	81.61 K	90.97 K	103.5 K	120.4 K
B4	X	X	X	X
B5	X	3.54	X	X
B6	X	X	X	X
B7	X	3.54	1.99, 0.654	X
B8	X	X	0.796	X
B9	X	X	0.354	X
B10	X	1.99, 0.354	0.531, 0.0354	0.199
B11	X	3.54	0.531, 0.0354	0.354
B12	X	0.354	0.531	0.106, 0.0199
B13	X	X	0.531, 0.0637	0.0637, 0.0199

Discussion

Both Device 1 and Device 3 show artifacts in the low frequency noise that may indicate more than a single noise source was active. Device 2 showed only *1/f*-like noise. At high frequency no data were obtained for Device 1, for Device 2 the low biases showed little excess noise, and for Device 3 there was excess noise at all biases and temperatures. These observed characteristics determined which type of analysis would be performed. For Device 1 the strong random telegraph signal noise and the lack of high frequency data restricted the analysis to that shown in chapter 8 of this work. Both Device 2 and Device 3 were analyzed with models for mobility fluctuation *1/f* noise and high frequency excess noise of the generation-recombination type.

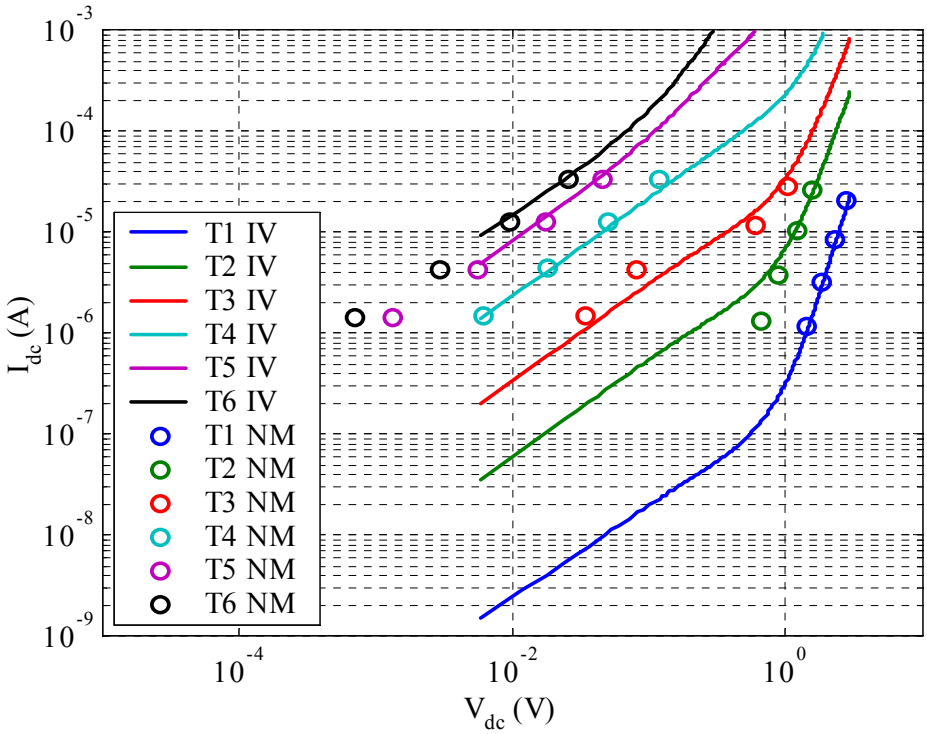

Figure 52 Third quadrant IV characteristic of Device 1 with noise measurement bias values shown.

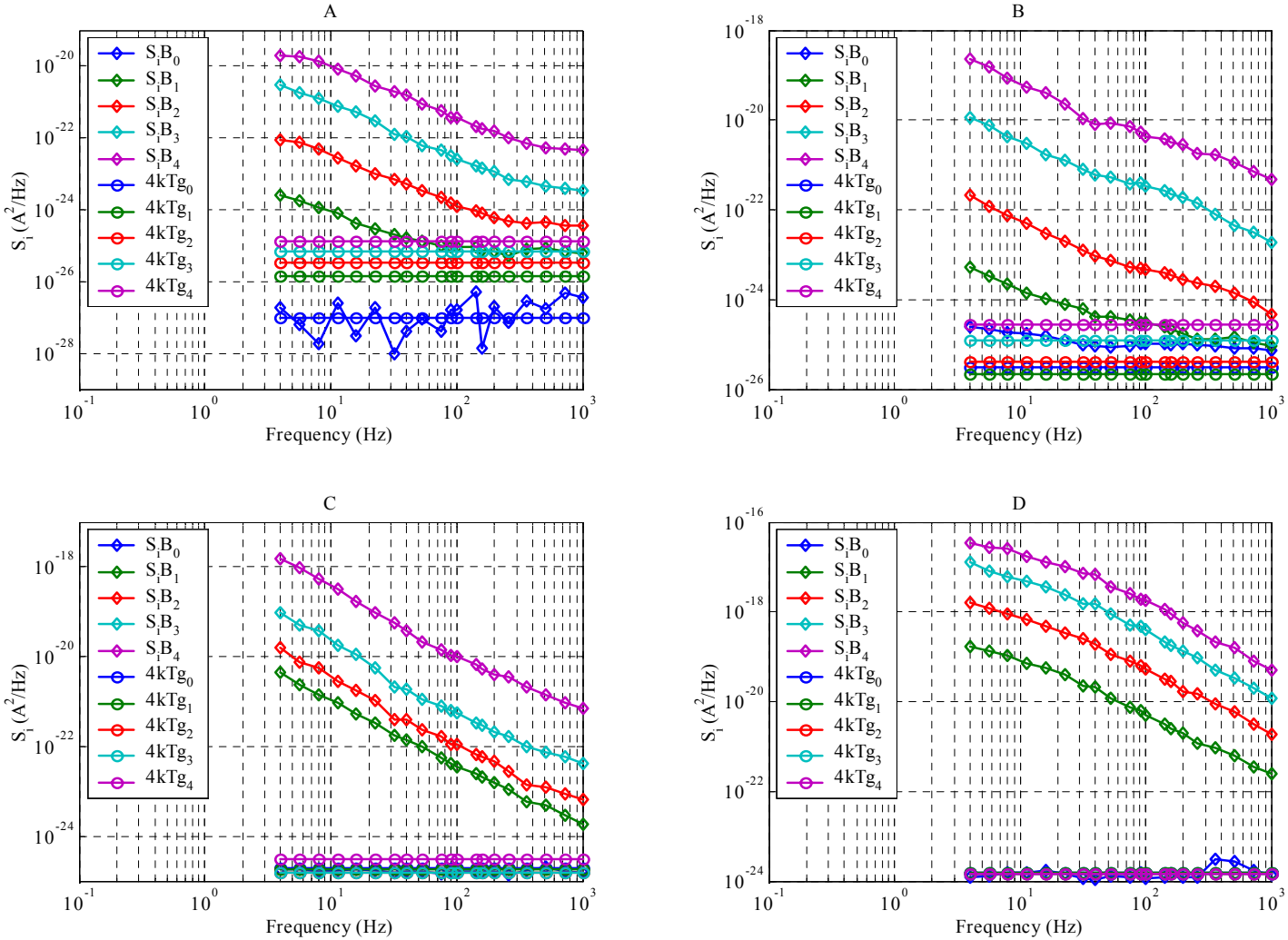

Figure 53 Current noise spectral density versus frequency for Device 1 at all biases measured. A) 82.1 K B) 91.7 K C) 104.2 K D) 121.2 K

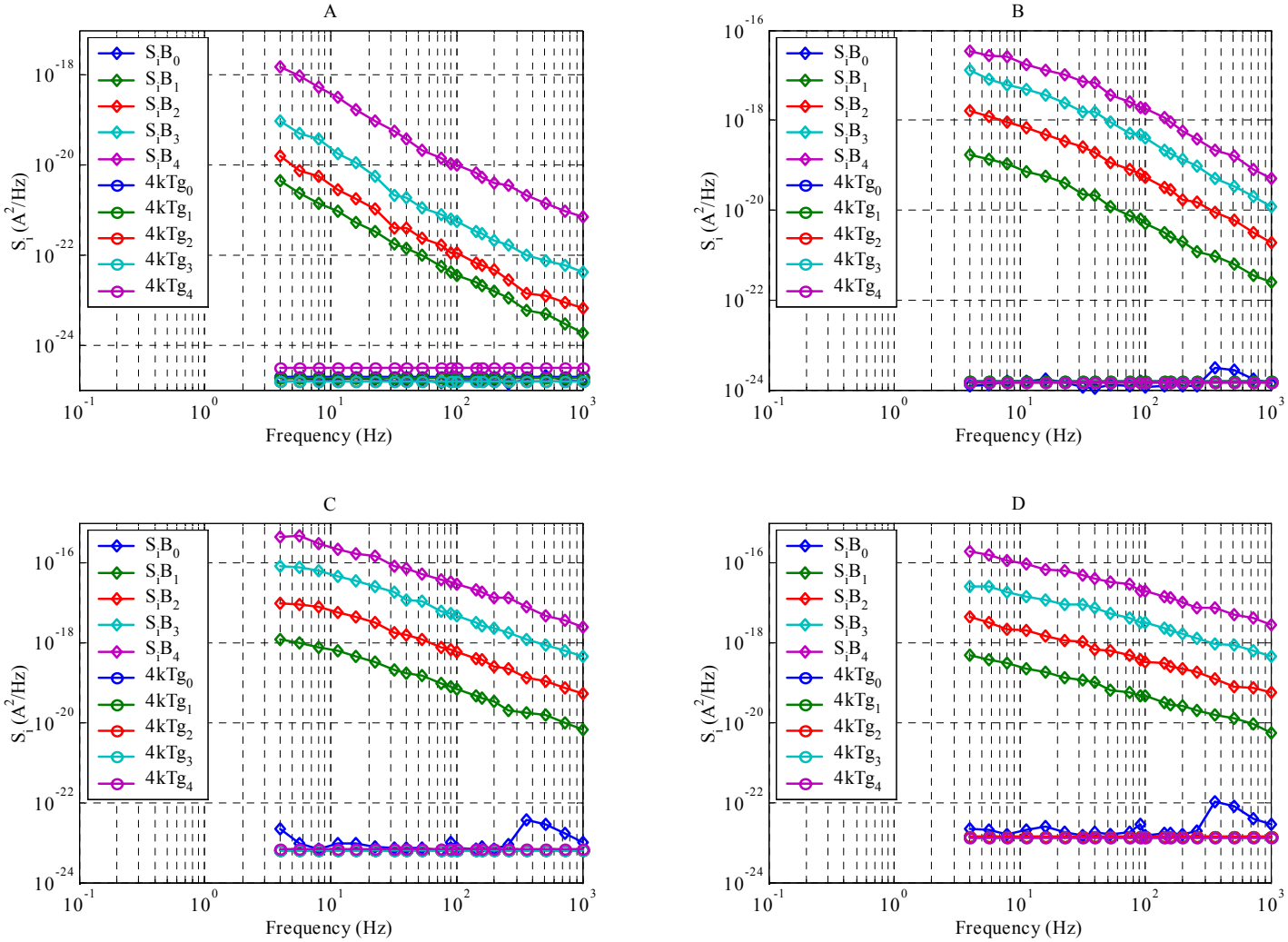

Figure 54 Current noise spectral density versus frequency for Device 1 for all biases measured. A)104.2 K B) 121.2 K C) 144.3 K D) 179.8 K

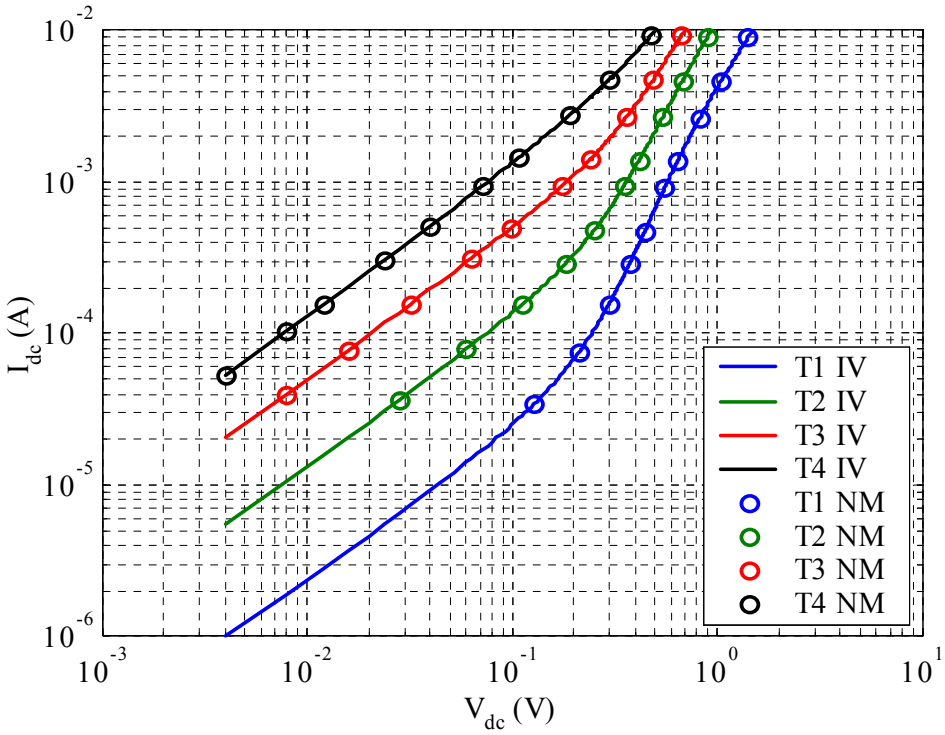

Figure 55 Third quadrant IV characteristic of Device 2 with noise measurement bias values shown.

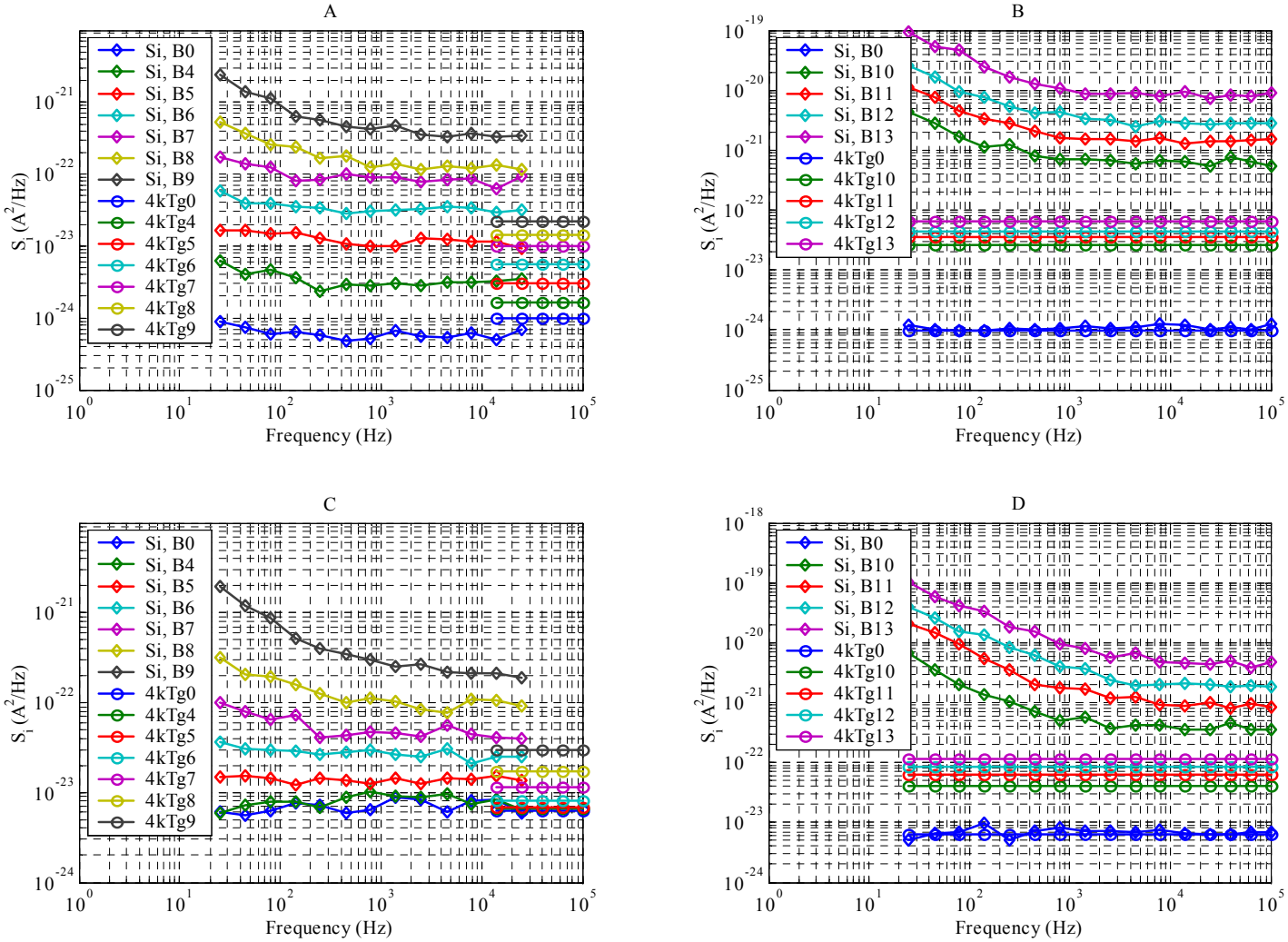

Figure 56 Current noise spectral density versus frequency for Device 2 for all biases measured. A) 81.66 K, B0-B9 B) 81.66 K, B0, B10-B13 C) 91.3 K, B0-B9 D) 91.3 K, B0, B10-B13

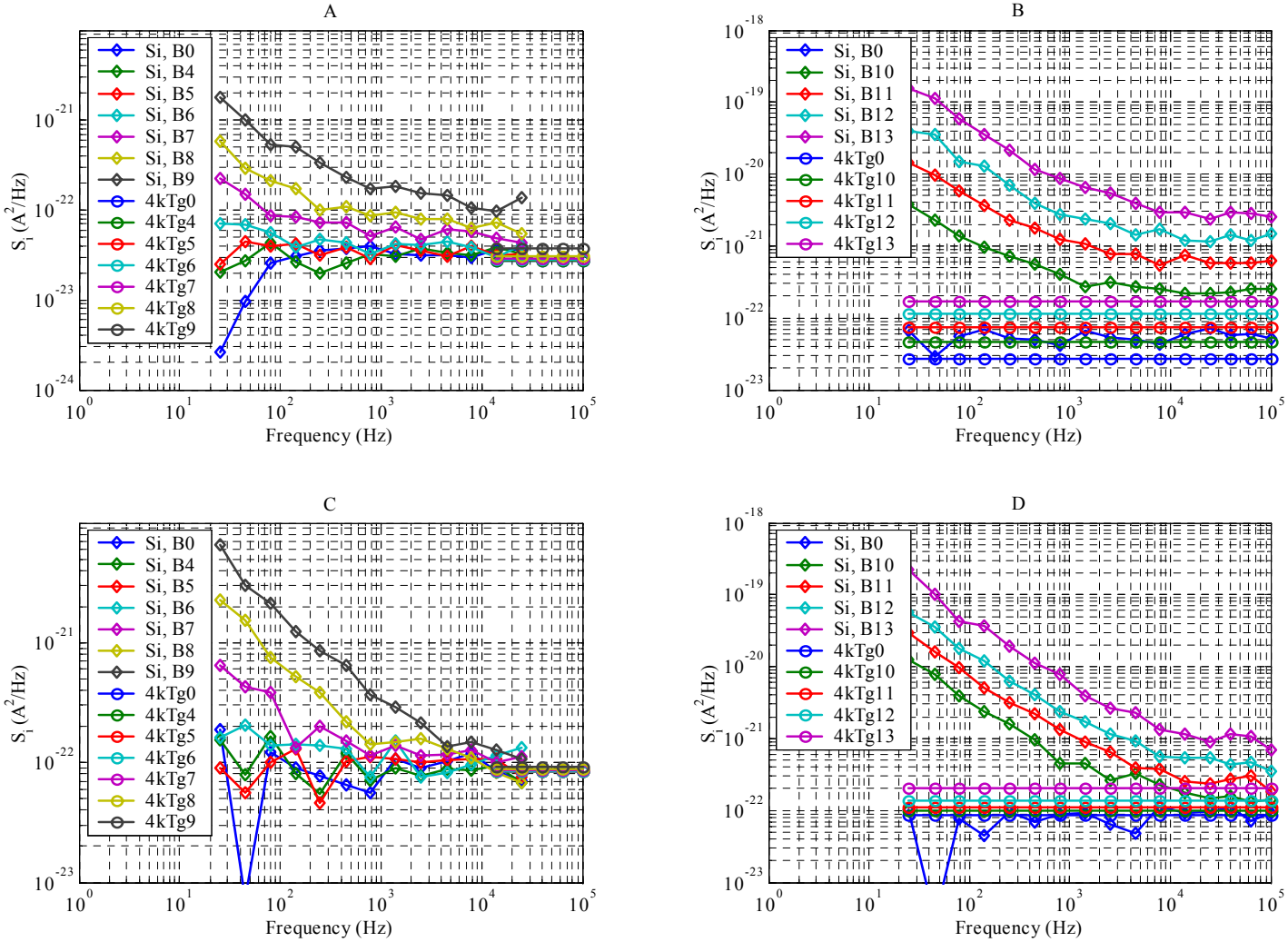

Figure 57 Current noise spectral density versus frequency for Device 2 for all biases measured. A) 103.7 K, B0-B9 B) 103.7 K, B0, B10-B13 C) 120.8 K, B0-B9 D) 120.8 K, B0, B10-B13

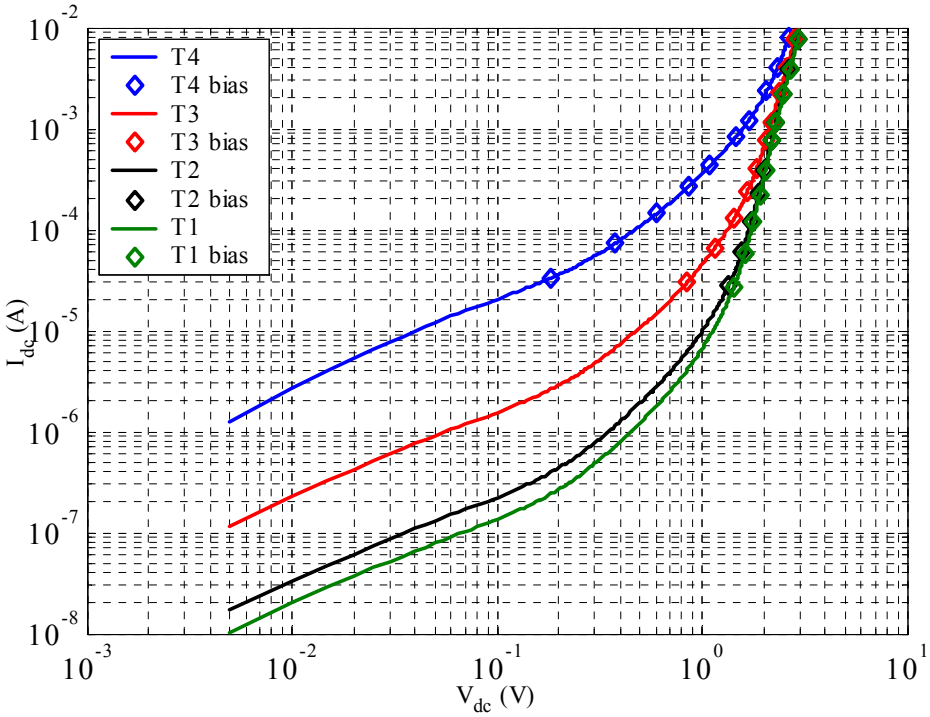

Figure 58 Third quadrant current versus voltage characteristic of Device 3 with noise measurement bias values shown.

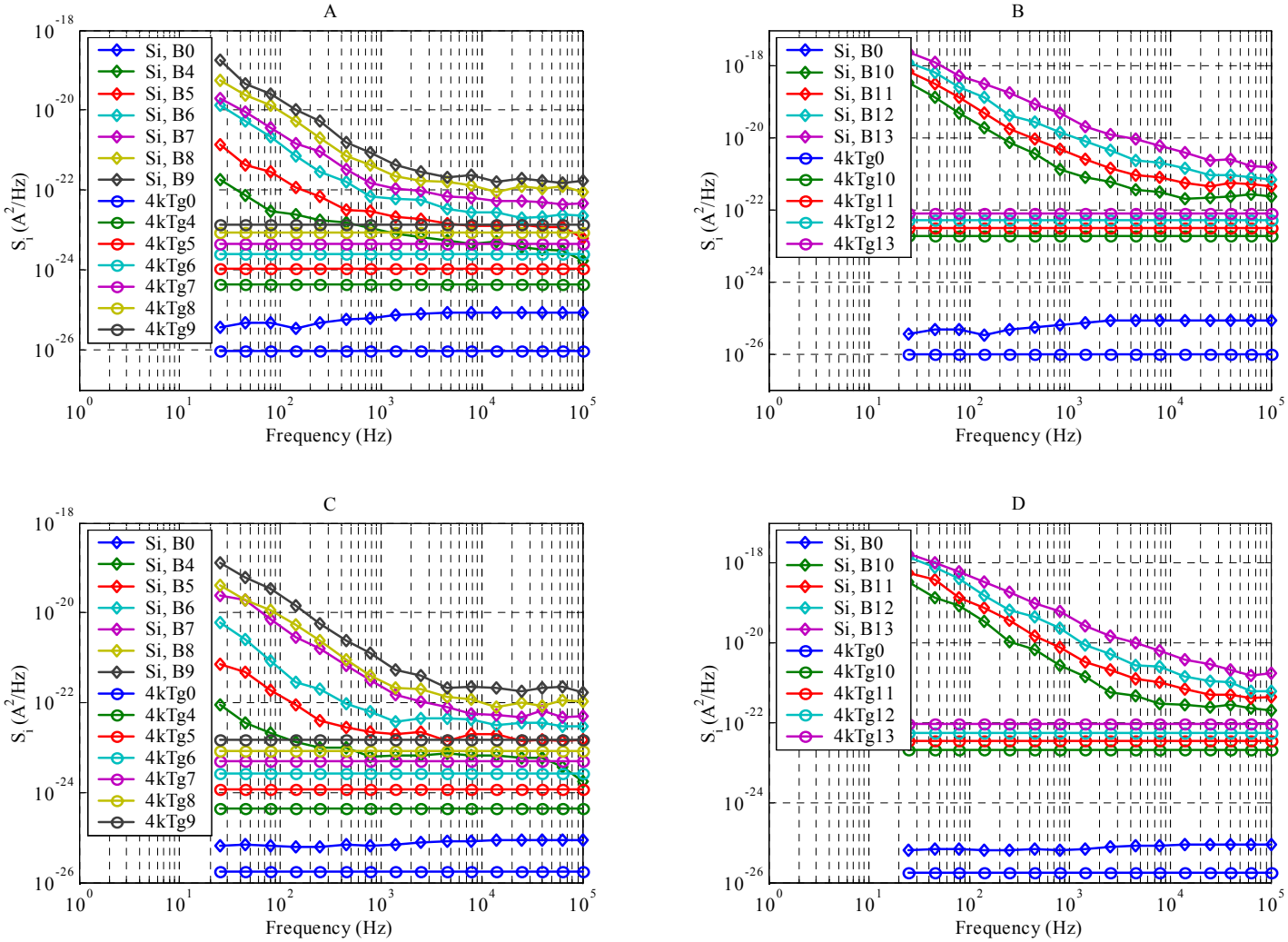

Figure 59 Current noise spectral density versus frequency for Device 3 for all biases measured. A) 81.61 K, B0-B9 B) 81.61 K, B0, B10-B13 C) 90.97 K, B0-B9 D) 90.97 K, B0, B10-B13

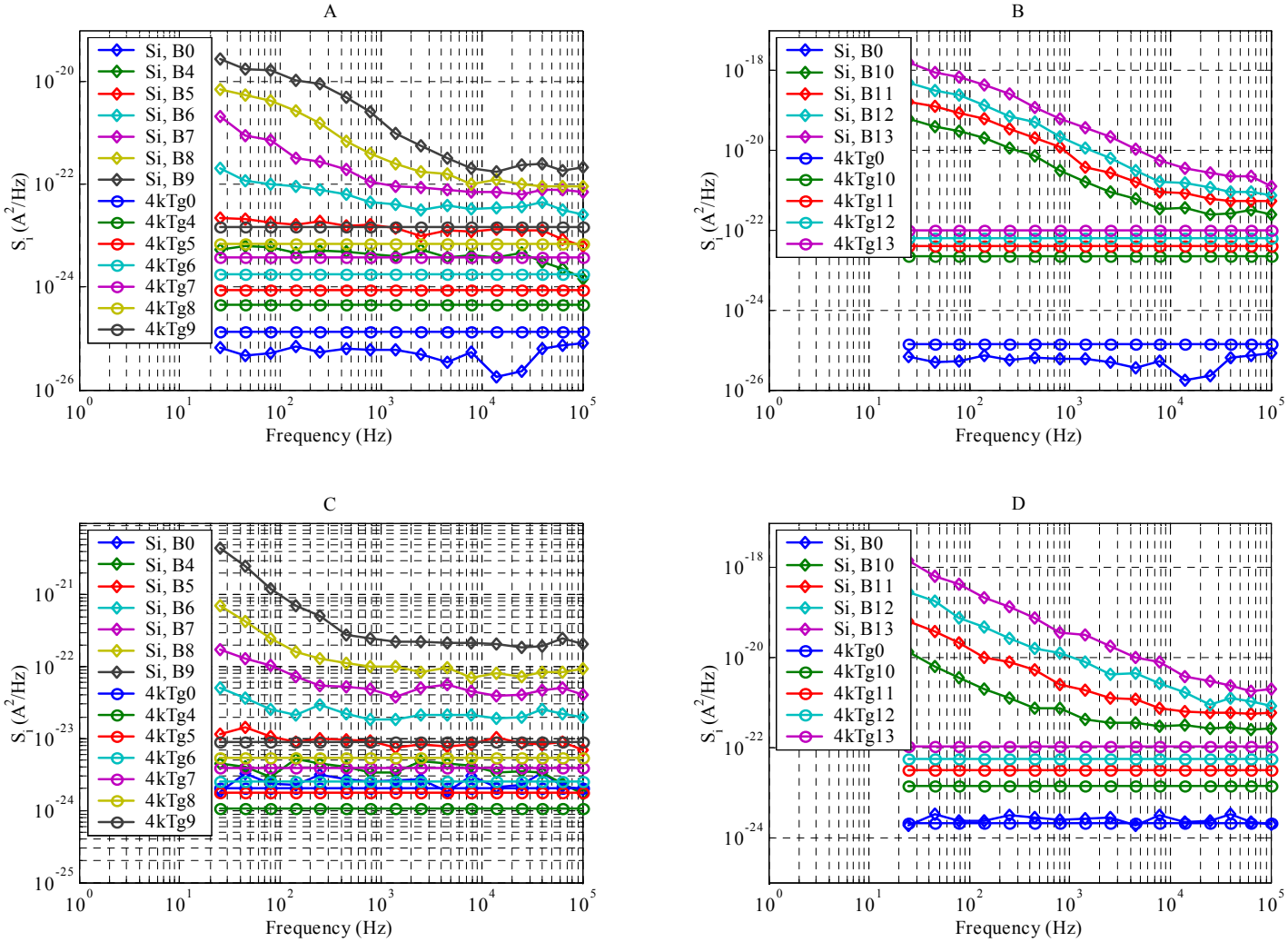

Figure 60 Current noise spectral density versus frequency for Device 3 for all biases measured. A) 103.5 K, B0-B9 B) 103.5 K, B0, B10-B13 C) 120.4 K, B0-B9 D) 120.4 K, B0, B10-B13

CHAPTER 6
GENERATION-RECOMBINATION NOISE

Introduction

In order to extract useful information from noise data there must be a mechanism that generates noise at a level above that predicted solely by thermal scattering. At the same time it is useful to have noise data taken at bias points where the sole contribution is thermal scattering. To obtain a value of thermal noise to compare with the measured noise, the modern equivalent of the Nyquist equation [27] is used. The real part of the conductance is replaced with the value of the dynamic resistance. The dynamic resistance is obtained by differentiating the IV characteristic. The Nyquist equation becomes

$$S_i(f) = \frac{4k_bT}{R_{ac}} \tag{6.1}$$

where S_i is the current noise spectral density, k_b is Boltzmann's constant, T is temperature in Kelvin, and R_{ac} is the derived dynamic resistance. The Nyquist equation for thermal noise is strictly only valid when the device is operating in the linear regime. Therefore care must be taken when evaluating a device.

Theory

One possible mechanism for excess noise is known as generation-recombination (GR) noise. Recall that the power spectral density of noise in the particle number is

$$S_N(f) = 4g_0 \frac{\tau^2}{1+\omega^2\tau^2} \tag{6.2}$$

where g_0 is the equilibrium generation rate, τ is the carrier lifetime, and ω is the frequency in radians per second [26]. Provided the device is operating in the linear regime, the normalized noise is a constant, or

$$\frac{S_N}{N^2} = \frac{S_V}{V^2} = \frac{S_I}{I^2} \tag{6.3}$$

where the numerators are the power spectral density of particle noise (S_N), voltage noise (S_V), and current noise (S_I) and the denominators are the square of the particle number (N), the voltage (V), and the current (I). The measured quantity was the power spectral density of the voltage noise, which was converted to the power spectral density of the current noise using the calculated dynamic resistance. Making the appropriate substitutions and rearranging, equation (6.2) becomes either

$$S_V = 4g_0 \frac{V^2}{N^2} \frac{\tau^2}{1+\omega^2\tau^2} \tag{6.4}$$

or

$$S_I = 4g_0 \frac{I^2}{N^2} \frac{\tau^2}{1+\omega^2\tau^2} \tag{6.5}$$

where each of the variables are as noted previously. For QWIPs the current in this equation is the dark current, I_d and may be represented by

$$I_d = qvnA \tag{6.6}$$

where q is the magnitude of the electric charge, v is the average velocity of the carrier, n is the density of electrons in the continuum and A is the device area. The electron density, n, can be represented as the total number of carriers, N, divided by the device volume, AL, where L is the device length. Making that substitution results in

$$I_d = qv\frac{N}{L} \tag{6.7}$$

with each variable as described previously. Substituting into equation (6.5) results in

$$S_I = 4q^2 g_0 \left(\frac{v\tau}{L}\right)^2 \frac{1}{1+\omega^2\tau^2} \tag{6.8}$$

which gives the power spectral density of current noise in terms of physical parameters. At frequencies a decade or more below the inverse of the carrier lifetime, τ, the term to the right of the parentheses is close to or equal to one, removing the frequency dependence.

Equation (6.8) was derived with the approximation that the generation rate exactly matches the recombination rate, in other words the device is at equilibrium. This approximation is not detrimental provided that the applied bias is small. What constitutes small bias is device and temperature dependent. Close to equilibrium g_0 may be replaced by the average generation rate, $\overline{G}$.

An additional approximation needed for the derivation involves the carrier lifetime. In equilibrium the generation rate is equal to the recombination rate. Designating the electron lifetime in the continuum as τ_o, the electron lifetime in the quantum well bound state as τ_s, the number of electrons in the continuum as N_o, and the number of electrons in the quantum well bound states as N_s, that rate equality may be written as

$$\frac{N_s}{\tau_s} = \frac{N_o}{\tau_o} \tag{6.9}$$

Since at low temperatures the number of electrons in the continuum is much smaller than the number of electrons in the quantum well bound states, equation (6.9) can only be true if τ_o is much smaller than τ_s. Given that and

$$\frac{1}{\tau} \approx \frac{1}{\tau_o} + \frac{1}{\tau_s} \tag{6.10}$$

τ in equation (6.8) can be approximated as τ_o. The power spectral density of current noise is now represented by

$$S_I = 4q^2\overline{G}\left(\frac{v\tau_o}{L}\right)^2 \tag{6.11}$$

In previous research [24] equation (6.11) was further manipulated to show two regimes of operation, diffusion dominant and drift dominant. The former is based on there being a weak enough electric field that carriers travel primarily by diffusion and is given by

$$S_i = 4q^2\overline{G}\left(\frac{L_D}{L}\right)^2 \tag{6.12}$$

where L_D is the distance a mobile carrier travels before recombining, known as the diffusion length. This formulation has two unknowns, L_D and $\overline{G}$. Assuming that the diffusion length is approximately equal to the barrier width in the QWIP, the average generation rate can be found. Of note is that according to this equation the noise is predicted to be bias independent.

The drift dominant noise regime assumes that the applied electric field is strong enough that the primary mode of travel for all carriers is drift. The equation describing this noise behavior is

$$S_i = \frac{4I_d^2}{\overline{G}} \tag{6.13}$$

and predicts that the noise will depend on the dark current squared. These two equations, (6.12) and (6.13), suggest that a clear demarcation exists between the two regimes and that it is dependent on the electric field within the device.

However both models, equations (6.12) and (6.13), contain the generation rate which requires a model that will predict the rate based on known material parameters. Still following Wang's work, a model for the generation rate is derived as follows.

In this derivation, the quantum well ground states are deemed trap states for the continuum electrons. Therefore the generation rate density will be proportional to the effective density of states in the conduction band, the doping density in the quantum well, the thermal velocity, and the capture cross section. There is also an exponential dependence on the energy distance between the continuum and the quantum well ground state. In short

$$\overline{g} = N_d N_c v_{th} \sigma_n \exp\left(-\frac{E_c - E_0}{k_b T}\right) \tag{6.14}$$

where N_d is the doping density, N_c is the effective density of states in the conduction band, v_{th} is the thermal velocity, σ_n is the capture cross section for electrons in the quantum well ground states, E_c is the conduction band energy, E_0 is the quantum well ground state energy, k_b is Boltzmann's constant, and T is temperature in Kelvin. To obtain the total electron generation rate, the generation rate density is multiplied by the volume of each quantum well times the number of quantum wells. In other words

$$\overline{G} = N_w A L_w \overline{g} \tag{6.15}$$

with N_w as the number of quantum wells, A as the area, and L_w as the width of each quantum well. As noted in Chapter 4 of this work during the discussion on current, both image force barrier lowering and electric field induced barrier lowering must be taken into account. This manifests by substituting a corrected energy distance in the exponential term so that it becomes

$$\exp\left(-\frac{E_B - \Delta E}{k_b T}\right) \tag{6.16}$$

where $E_B = E_c - E_0$ and ΔE is the barrier lowering given by

$$\Delta E = q\Delta\phi + q\mathscr{E} L_w \tag{6.17}$$

where q is the magnitude of the electric charge, $\Delta\phi$ is image force barrier lowering, $\mathscr{E}$ is the electric field in the quantum well, and L_w is the width of the quantum well.

The final form for the total electron generation rate is now

$$\overline{G} = N_w A L_w C \exp\left(-\frac{E_B - \Delta E}{k_b T}\right) \tag{6.18}$$

where C will be used as a fitting parameter and is given by

$$C = N_d N_c v_{th} \sigma_n \tag{6.19}$$

in which both the temperature and field dependence are assumed to be negligible.

There are now two equations that can be used to compare measurements with theory. Equation (6.12), applicable to the diffusion regime, is now

$$S_i = 4q^2 N_w A L_w C \exp\left(-\frac{E_B - \Delta E}{k_b T}\right)\left(\frac{L_D}{L}\right)^2 \tag{6.20}$$

and equation (6.13), applicable to the drift regime, is now

$$S_i = \frac{4I_d^2}{N_w A L_w C \exp\left(-\frac{E_B - \Delta E}{k_b T}\right)} \tag{6.21}$$

where all variables have been defined previously.

Experimental Data

Device I

The GR noise analysis as derived in this chapter requires that data be obtained in a region of frequency independence. Since reliable noise measurements were not obtained above 1 kHz and there is no plateau reached below 1 kHz, there can be no analysis for this device as described above.

Device II

A summary of the high frequency plateau current noise spectral density data for D2 are given in Table 24 and Table 25. Comparing the measured and predicted values in the linear regime of operation, set in bold, shows that they are less than a factor of three from each other. Whereas outside of the linear regime of operation the differences are much larger, achieving a factor larger than 140 at B13 of 81.66 K. This confirms, and perhaps refines, observations made using the IV characteristics about the bounds of the linear regime of operation. In short, excess noise exists in the high frequency plateau and is most pronounced at high bias values and low temperatures. Caution is required in the application of GR theory to the high bias, low temperature data since the device has entered the onset of non-linear IV behavior.

Using high frequency data at each temperature, Figure 61 shows the relationship of the noise to the applied field. Even though approximately the same current bias was applied at each temperature, the resulting fields in the device vary widely. This may be explained by the effects of temperature on resistivity. At lower temperatures fewer electrons will be excited into the continuum resulting in a higher resistivity. An increase in resistivity without changing the current results in a larger applied voltage. Since the

device length is unchanged, the increase in applied voltage results in a larger applied field. Therefore, the variation in field with temperature is expected.

Table 24 D2 measured noise spectral density in the high frequency plateau and predicted thermal noise at 81.66 K and 91.3 K. (Units are A^2/Hz, bold type is linear operating regime)

	81.66 K		91.3 K	
BIAS	measured	predicted	measured	predicted
B4	**$3.24\cdot10^{-24}$**	**$1.61\cdot10^{-24}$**	**$8.42\cdot10^{-24}$**	**$6.57\cdot10^{-24}$**
B5	$1.14\cdot10^{-23}$	$2.99\cdot10^{-24}$	**$1.51\cdot10^{-23}$**	**$6.88\cdot10^{-24}$**
B6	$2.94\cdot10^{-23}$	$5.63\cdot10^{-24}$	$2.48\cdot10^{-23}$	$8.12\cdot10^{-24}$
B7	$6.22\cdot10^{-23}$	$1.01\cdot10^{-23}$	$4.08\cdot10^{-23}$	$1.15\cdot10^{-23}$
B8	$1.36\cdot10^{-22}$	$1.44\cdot10^{-23}$	$1.05\cdot10^{-22}$	$1.73\cdot10^{-23}$
B9	$3.28\cdot10^{-22}$	$2.18\cdot10^{-23}$	$2.11\cdot10^{-22}$	$2.96\cdot10^{-23}$
B10	$6.34\cdot10^{-22}$	$2.67\cdot10^{-23}$	$3.60\cdot10^{-22}$	$3.99\cdot10^{-23}$
B11	$1.28\cdot10^{-21}$	$3.55\cdot10^{-23}$	$8.68\cdot10^{-22}$	$6.22\cdot10^{-23}$
B12	$2.79\cdot10^{-21}$	$4.40\cdot10^{-23}$	$2.13\cdot10^{-21}$	$8.59\cdot10^{-23}$
B13	$9.45\cdot10^{-21}$	$6.61\cdot10^{-23}$	$4.54\cdot10^{-21}$	$1.16\cdot10^{-22}$

Table 25 D2 measured noise spectral density in the high frequency plateau and predicted thermal noise at 103.7 K and 120.8 K. (Units are A^2/Hz, bold type is linear operating regime)

	103.7 K		120.8 K	
BIAS	measured	predicted	measured	predicted
B4	**$3.85\cdot10^{-23}$**	**$8.44\cdot10^{-23}$**	**$9.31\cdot10^{-23}$**	**$8.44\cdot10^{-23}$**
B5	**$3.19\cdot10^{-23}$**	**$8.46\cdot10^{-23}$**	**$1.08\cdot10^{-22}$**	**$8.46\cdot10^{-23}$**
B6	**$2.99\cdot10^{-23}$**	**$8.47\cdot10^{-23}$**	**$1.15\cdot10^{-22}$**	**$8.47\cdot10^{-23}$**
B7	**$4.90\cdot10^{-23}$**	**$8.57\cdot10^{-23}$**	**$9.98\cdot10^{-23}$**	**$8.57\cdot10^{-23}$**
B8	**$7.32\cdot10^{-23}$**	**$8.73\cdot10^{-23}$**	**$8.18\cdot10^{-23}$**	**$8.73\cdot10^{-23}$**
B9	**$9.85\cdot10^{-23}$**	**$9.16\cdot10^{-23}$**	**$1.27\cdot10^{-22}$**	**$9.16\cdot10^{-23}$**
B10	$2.19\cdot10^{-22}$	$4.63\cdot10^{-23}$	**$1.76\cdot10^{-22}$**	**$9.72\cdot10^{-23}$**
B11	$7.51\cdot10^{-22}$	$7.51\cdot10^{-23}$	**$2.56\cdot10^{-22}$**	**$1.12\cdot10^{-22}$**
B12	$1.18\cdot10^{-21}$	$1.13\cdot10^{-22}$	$5.37\cdot10^{-22}$	$1.39\cdot10^{-22}$
B13	$2.91\cdot10^{-21}$	$1.68\cdot10^{-22}$	$1.15\cdot10^{-21}$	$2.04\cdot10^{-22}$

In light of that observation, there should also be a variation in the mechanism that couples the noise to the outside circuit. The graphs in Figure 62 represent the noise data with respect to current bias at each temperature. The predicted value of thermal noise at zero bias as described above is added for reference. Referring to Figure 61 the prediction

would be for diffusion dominant noise at low biases of 103.7 K and 120.8 K and for drift dominant noise at all biases of 81.66 K and the majority of biases of 91.3 K. In addition, it appears that no matter what the temperature there is a transition between the two regimes in the vicinity of 800 V/cm to 1000 V/cm.

Returning to Figure 62A there is definitely current bias dependence in the noise at 81.66 K. Further scrutiny reveals that the slope of the curve, or more to the point the exponent of I, is less than two but greater than one. In fact the slope is 1.38 making the current dependence $I^{1.38}$ rather than I^2. Moving on to 91.3 K, depicted in Figure 62B, the current bias dependence is beginning to flatten out below about 100 μA. The slope for currents greater than that is about 1.33 which is close to that of 81.66 K. At 103.7 K, seen in Figure 62C, the flattening begins at a slightly higher current, in the vicinity of 0.5 mA. The noise versus current relationship above that bias exhibits a slope of about 1.34 which is close to both of the lower temperatures measured. At 120.8 K, shown in Figure 62D, bias independence is observed up to about 1 mA at which point an upturn begins that exhibits a slope of about 0.958. This deviation in slope at 120.8 K is also evident in the graph of Figure 61.

For each case a value was calculated for the fitting parameter C, as defined in equation (6.19), from a data point that is convincingly within one regime or another. For the case of the diffusion dominant model, the diffusion length, L_D, was chosen to be the nominal barrier width, 500 Å. The data point used to calculate C was the lowest bias at the highest temperature and resulted in a value of $C_{diff} = 5.64 \cdot 10^{30}$ cm^{-3}s^{-1}. For the drift dominant model the data point used to calculate C was the highest bias of the lowest temperature and resulted in a value of $C_{drift} = 5.41 \cdot 10^{30}$ cm^{-3}s^{-1}. These two values are less

than 5% different. In addition, the drift dominant model C value was used in the diffusion dominant model at the appropriate temperature and bias to extract the diffusion length and resulted in a value of 510.2 Å which is within 2% of the barrier width nominal value.

Predicted noise values were calculated using C_{drift} and the derived diffusion length in equation (6.20), and C_{diff} in equation (6.21). These values were plotted with measured data and are shown in Figure 63 for drift and Figure 64 for diffusion. An overall view of the four graphs in each figure reveals that theory and data follow the same trends at each temperature. In addition, it appears that the range of biases encompasses a transition region, most notable at the middle two temperatures 91.3 K (Figure 63B and Figure 64B) and 103.7 K (Figure 63C and Figure 64C). The proximity to an operational transition region may account for the fact that the data at high bias do not exhibit the predicted I^2 dependence. The data in the low bias regions of 103.7 K (Figure 63C and Figure 64C) and 120.8 K (Figure 63D and Figure 64D) clearly show the expected bias independence of the noise.

Device III

The current noise spectral density versus applied electric field for all four temperatures are shown in Figure 65. One striking difference from D2 is that at no temperature or bias does D3 show the diffusion noise plateau. This is indicative that the noise of D3 did not couple out via diffusion at the biases and temperatures for which noise measurements were taken. This also indicates that the possibility exists that this form of GR analysis may be invalid, or at the least require some modification, for this device.

Turning to the current noise spectral density versus bias current graphs in Figure 66, another reason to be skeptical of this type of analysis on this device is found. Performing a least squares fit on the data at 63 kHz results in an approximately linear dependence of the current noise spectral density on the bias current. The derivation results clearly show that the current noise spectral density is predicted to be proportional to I^2 when the noise couples out via drift. However, revisiting the noise versus applied field, Figure 65, an argument could be made that the regime of operation is somewhere in between diffusion and drift. In addition, recall that for D2 the current dependence was less than squared though clearly greater than linear, yet the theory predicted the current noise spectral density to a close degree.

Performing the same analysis as is done for D2 results in a C_{diff} value of $2.46 \cdot 10^{33}$ $cm^{-3}s^{-1}$ and a C_{drift} value of $2.93 \cdot 10^{36}$ $cm^{-3}s^{-1}$. That these values differ by a factor of a thousand is an indication that there is not a single value for the fitting parameter C which will predict the current noise spectral density at all temperatures and biases. This is in direct contrast to the results of D2. Not surprisingly the drift derived value for C plugged into the drift model equation predicts the current noise spectral density fairly well at 81.61 K. Somewhat unexpectedly, the diffusion derived value for C plugged into the drift model equation predicts the current noise spectral density fairly well at 120.4 K.

Probing further it is found that using either model equation at appropriate bias and temperature to derive the fitting parameter C results in little difference in values between the two methods at corresponding temperatures, shown in Table 26. Using the temperature dependent calculated values for C_{drift} in both model equations results in good prediction of the current noise spectral density as seen in Figure 67. The same was done

with the calculated values of C_{diff} and the results are shown in Figure 68. The latter result is particularly interesting since the data indicate that this device is not definitively operating in the diffusion regime at any bias or temperature at which measurements were taken. This may be another indication that these operating conditions are within a transition region between the two coupling mechanisms of drift and diffusion.

Table 26 Fitting parameter, *C*, for Device 3 as derived by each model equation.

Temperature (K)	C_{drift} ($cm^{-3}s^{-1}$)	C_{diff} ($cm^{-3}s^{-1}$)
81.61	$2.9 \cdot 10^{36}$	$2.0 \cdot 10^{36}$
90.97	$3.1 \cdot 10^{35}$	$2.3 \cdot 10^{35}$
103.5	$1.8 \cdot 10^{34}$	$2.0 \cdot 10^{34}$
120.4	$2.3 \cdot 10^{33}$	$2.5 \cdot 10^{33}$

Discussion

Frequency independent excess noise in Device 2 and Device 3 was analyzed with a model derived for linear operation near equilibrium. The model is predictive for Device 2 in both mechanisms of charge transport, drift and diffusion. As well, the approximation for the diffusion length as the barrier width was confirmed. The bias range for which noise was measured was found to encompass a transition region between the two charge transport mechanisms. All of this indicates that the departure from the derivation conditions of linear operation near equilibrium does not extend beyond the usefulness of the model. It would be instructive to extend the measurement conditions further into the non-linear regime to see how extensive a departure is required for the model to break down.

For Device 3 the conditions obviously extend beyond the purview of the model. The operating conditions for which noise measurements were obtained were primarily outside of linear. There is no definitive transition region observed. As well, the fitting parameter exhibited a strong temperature dependence, which was assumed negligible in

the model. However, allowing for the temperature dependence, the model showed good predictive ability. Further study would be required to discern whether the model could be extended to include the non-linear current regime.

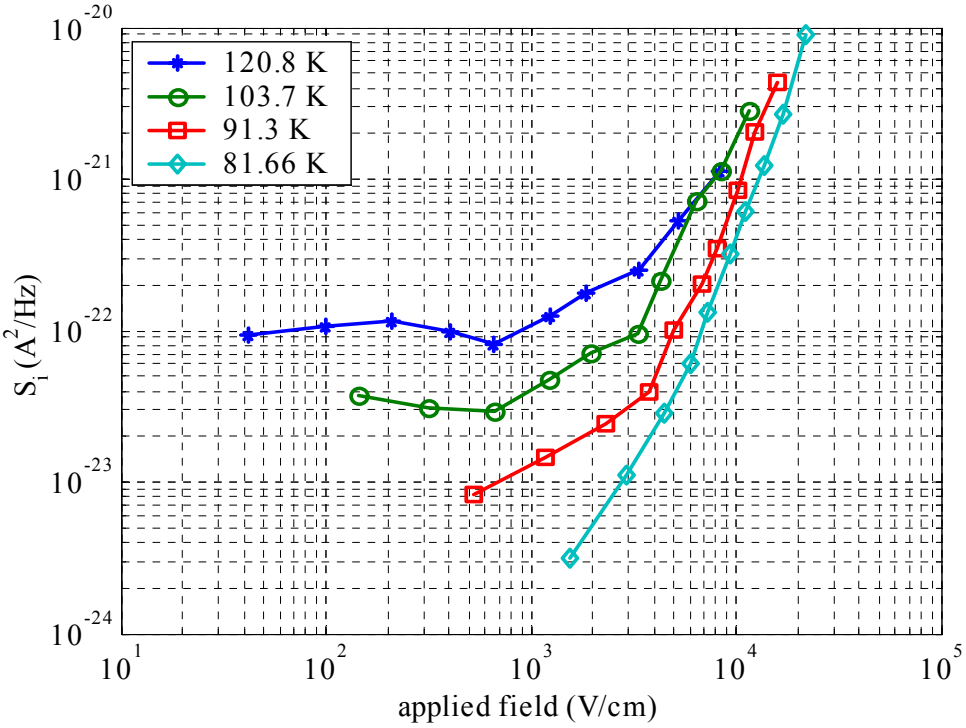

Figure 61 Current noise spectral density versus applied electric field for Device 2 at four temperatures.

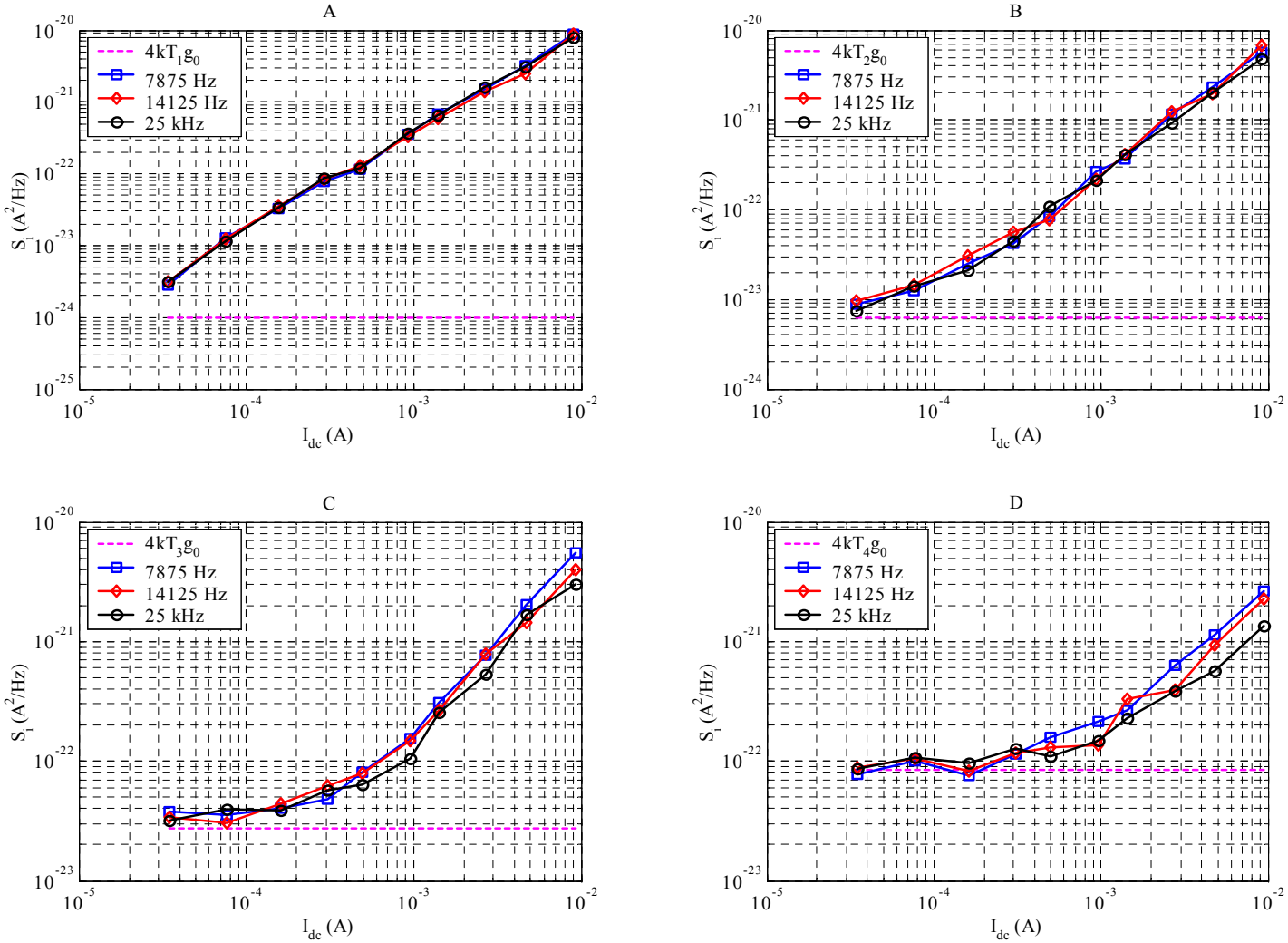

Figure 62 Current noise spectral density versus bias current for Device 2 at high frequency. A) 81.66 K B) 91.3 K C) 103.7 K D) 120.8 K

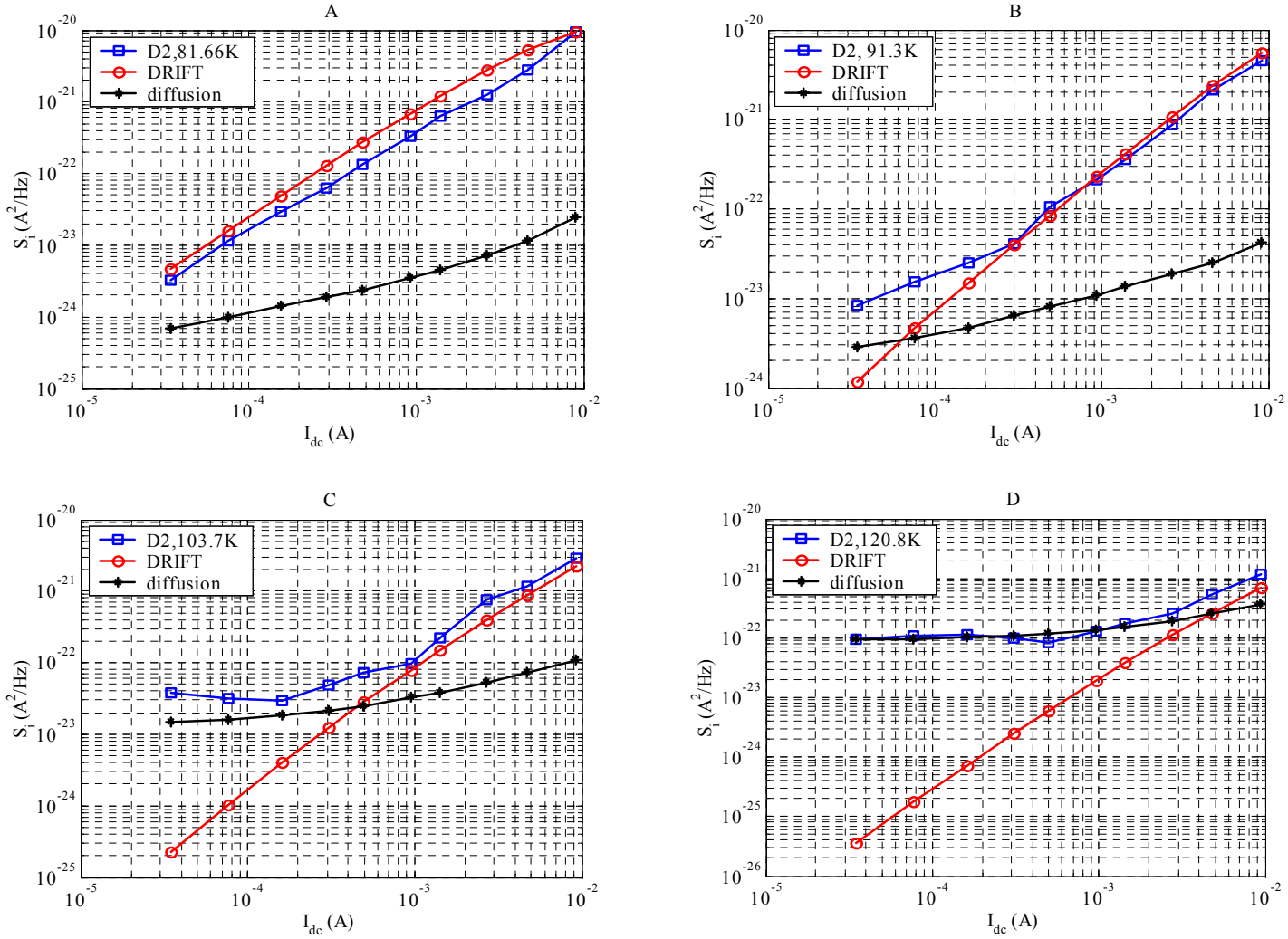

Figure 63 Comparison of theory and data for Device 2. The value of *C* is that derived from the drift model. A) 81.66 K B) 91.3 K C) 103.7 K D) 120.8 K

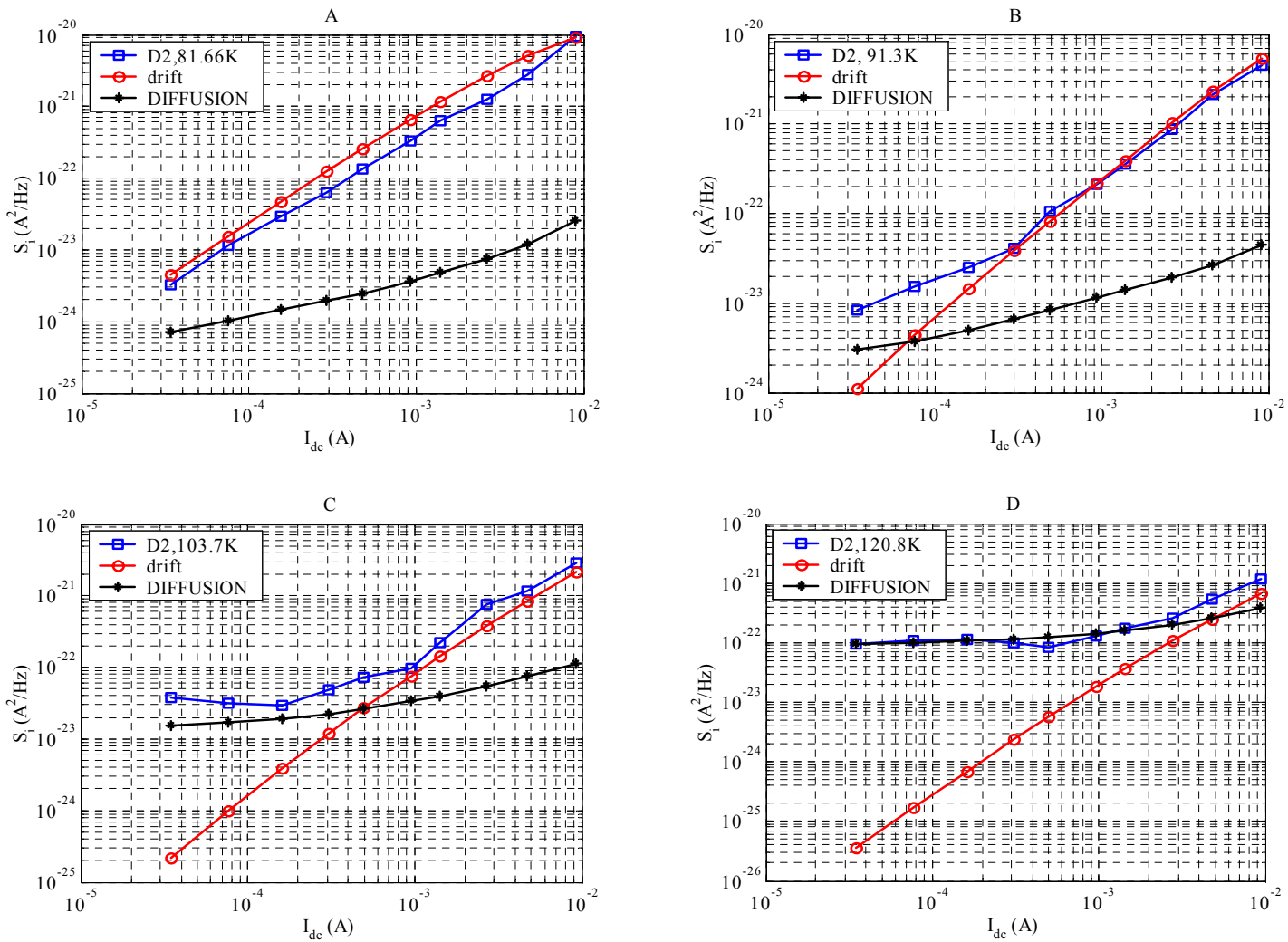

Figure 64 Comparison of theory and data for Device 2. The value of *C* is that derived from the diffusion model. A) 81.66 K B) 91.3 K C) 103.7 K D) 120.8 K

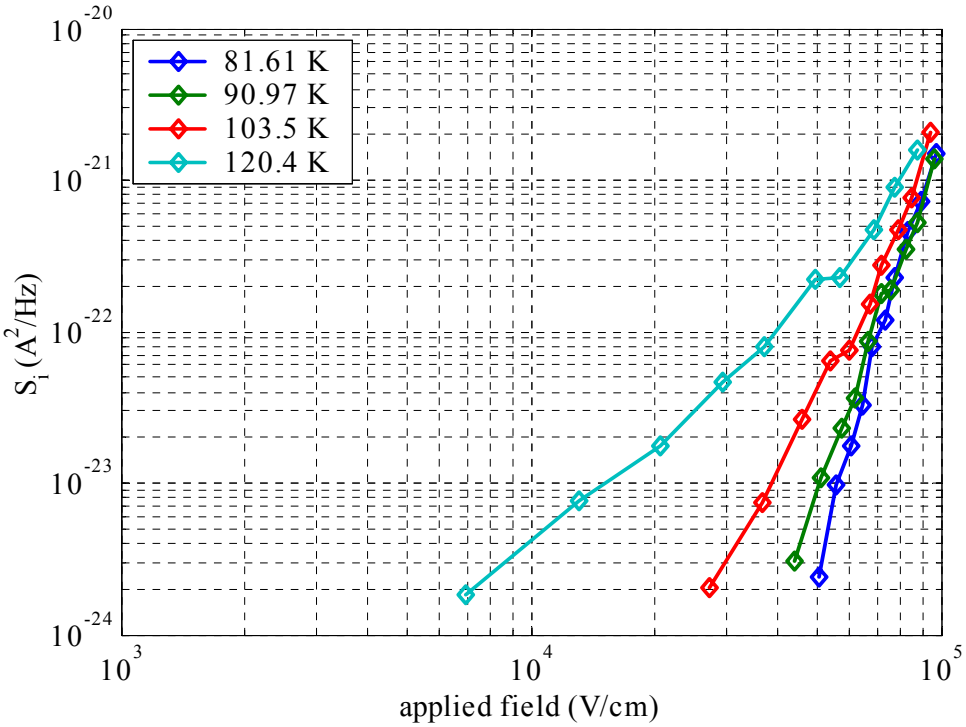

Figure 65 Current noise spectral density versus applied electric field for Device 3 at four temperatures.

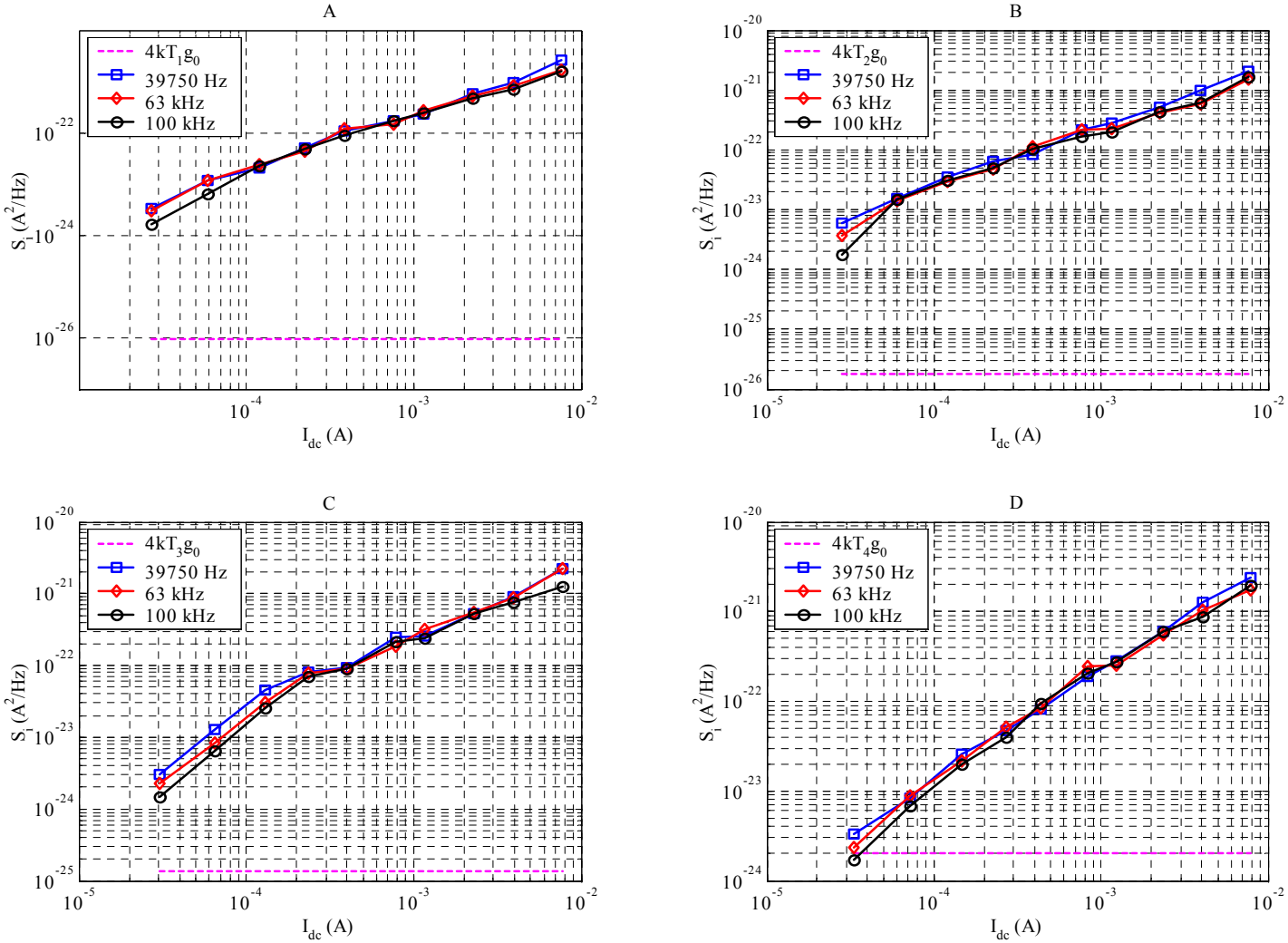

Figure 66 Current noise spectral density versus bias current for Device 3 at high frequency. A) 81.61 K B) 90.97 K C) 103.5 K D) 120.4 K

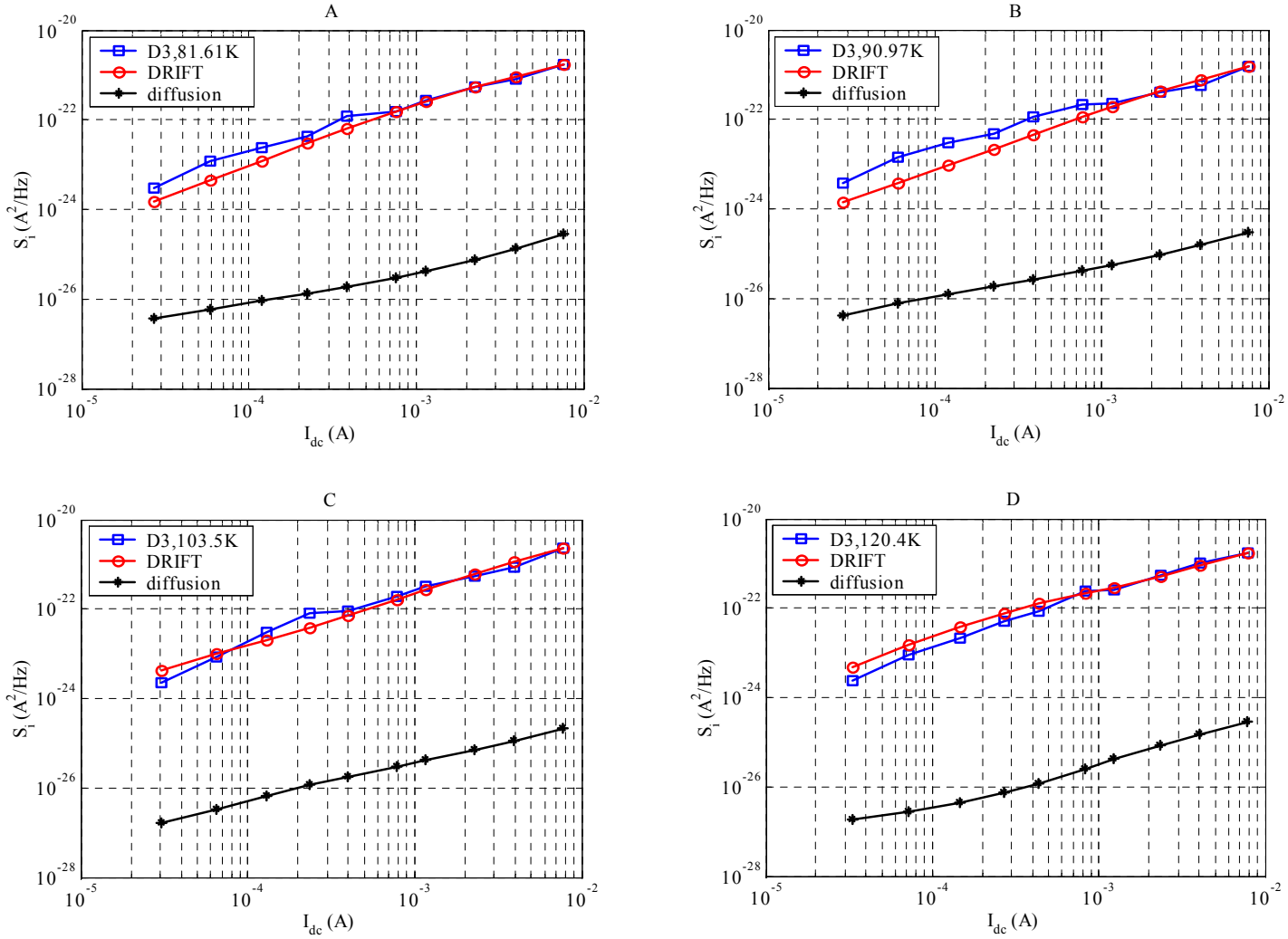

Figure 67 Comparison of theory and data for Device 3. The value of *C* is that derived from the drift model specifically for each temperature. A) 81.61 K B) 90.97 K C) 103.5 K D) 120.4 K

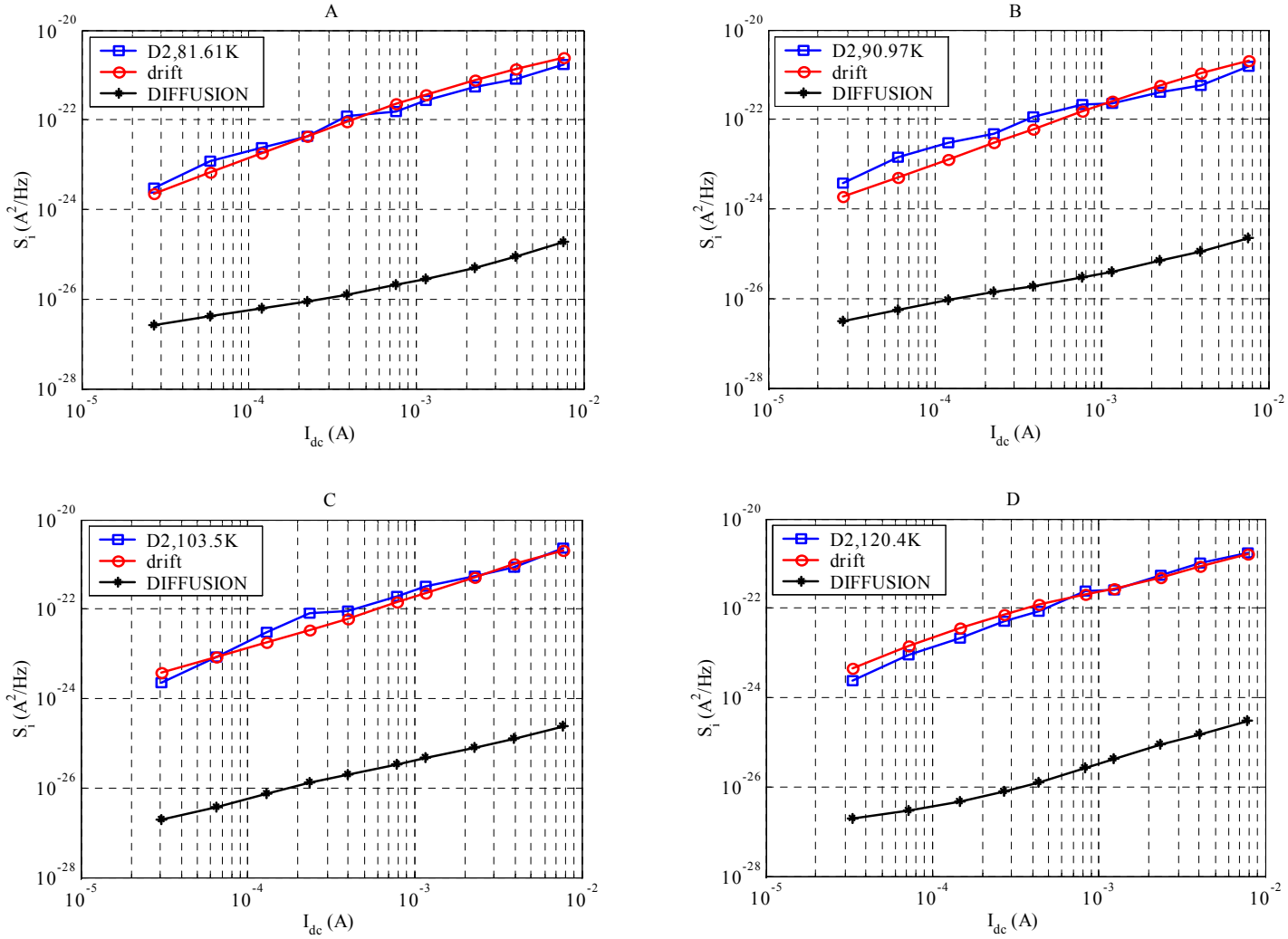

Figure 68 Comparison of theory and data for Device 3. The value of *C* is that derived from the diffusion model specifically for each temperature. A) 81.61 K B) 90.97 K C) 103.5 K D) 120.4 K

CHAPTER 7
FLICKER NOISE

Introduction

Flicker noise is a general term that describes any noise whose spectrum has a frequency dependence of $1/f^{\gamma}$ in which γ has a value close to one. It is a pervasive phenomenon, manifesting in many different systems. The system of interest to this research is that involving semiconductors. To date no definitive theory has been formulated though not from lack of hypotheses.

In the realm of resistive components, of which some semiconductor devices are a subset, some prevailing features have been defined and studied [26]. First there must be other frequency dependences besides $1/f$ exhibited by the device. Also, providing a constant current to the device results in an open circuit voltage spectrum that varies as I_{dc}^2 provided that the resistance fluctuations, $\delta R(t)$, are independent of the DC current, I_{dc}. Finally, the voltage noise spectral density, $S_V(f)$, is usually proportional to the device resistance, R_o. Van der Ziel concludes that the ultimate expression for $1/f$ noise in resistors is

$$S_V(f) = \frac{KV_o^2 R_o}{f} \tag{7.1}$$

where K is a constant associated with the material in question.

Theory

The following discussion and derivation of equations useful in the evaluation of flicker noise is a paraphrasing of a portion of van der Ziel [26]. The discussion begins with the basic equation for a resistor made from an n-type semiconductor

$$R = \frac{L}{A}\frac{1}{q\mu n} \tag{7.2}$$

where R is the value of resistance, L is the resistor length, A is the resistor area, q is the magnitude of the electric charge, μ is the electron mobility, and n is the density of mobile electrons. Using the definition of electron density, an equivalent expression is obtained

$$R = \frac{L^2}{q\mu N} \tag{7.3}$$

where N is the number of mobile electrons.

A fluctuation in R is only possible if μ and/or N fluctuate. Fluctuation in number is depicted by δN and results in number fluctuation noise. Fluctuation in mobility is depicted by $\delta\mu$ and results in mobility fluctuation noise. With the overbar denoting average values, the fluctuation in R can be represented as

$$\frac{\delta R}{\overline{R}} = -\frac{\delta N}{\overline{N}} - \frac{\delta\mu}{\overline{\mu}} \tag{7.4}$$

Further, assuming that δN and $\delta\mu$ are independent, then

$$\frac{S_R(f)}{\left(\overline{R}\right)^2} = \frac{S_N(f)}{\left(\overline{N}\right)^2} + \frac{S_\mu(f)}{\left(\overline{\mu}\right)^2} = \frac{S_V(f)}{\left(\overline{V}\right)^2} \tag{7.5}$$

This equation shows the possibility that both number and mobility fluctuation noise may be present concurrently, but does not preclude the dominance of one over the other.

Ignoring, for the moment, the mobility fluctuation noise contribution, the number fluctuation noise may be modeled as

$$\frac{S_V(f)}{\left(\overline{V}\right)^2} = \frac{\alpha'}{f\overline{N}}, \quad \alpha' = \frac{\beta}{\ln\left(\tau_1/\tau_0\right)} \tag{7.6}$$

where β is defined by Klaasen [29] using $\overline{\Delta N^2} = \beta\overline{N}$ and $ln(\tau_1/\tau_0)$ results from the postulation of a wide distribution of time constants.

In a similar fashion, ignoring the contribution of number fluctuation noise, mobility fluctuation noise may be modeled as

$$\frac{S_V(f)}{\left(\overline{V}\right)^2} = \frac{\alpha}{f\overline{N}}, \quad \alpha = \frac{\alpha_a^2}{\ln\left(\tau_1/\tau_0\right)} \tag{7.7}$$

where α_a^2 is a material dependent constant with a value less than one and $ln(\tau_1/\tau_0)$ is as described above.

These two models have the same functional form as one presented by Hooge in 1969 [28] that is based on data from many materials,

$$\frac{S_I(f)}{\left(\overline{I}\right)^2} = \frac{S_V(f)}{\left(\overline{V}\right)^2} = \frac{\alpha_H}{f\overline{N}} \tag{7.8}$$

where α_H was postulated to be a universal, dimensionless constant and weakly dependent on temperature. Though no longer deemed a universal constant, the Hooge parameter, α_H, is still considered to be useful in the analysis of flicker noise, primarily as a figure of merit.

In order for number fluctuations to manifest as *1/f*-like noise, there must be a continuous distribution of time constants associated with the generation and recombination of carriers. There are three postulated causes of this distribution in time

constants. First, that electrons interact with traps via tunneling. Second, that electrons interact with acoustical phonons. And third, that there is a distribution of activation energies within the device. The latter cannot explain electron interaction with traps in the forbidden energy gap of semiconductors.

Noise models postulated for mobility fluctuation *1/f*-like noise include carrier interaction with slowly fluctuating longitudinal phonons and slow fluctuations in the free path length, l, of the carriers. The former leads to a distribution of time constants but cannot account for the observed ultra-low frequency *1/f*-like noise. The latter model may be explained in two ways. First, with the mobility proportional to the free path length, perturbations in l result in perturbations in μ.

$$\frac{\delta\mu}{\bar{\mu}} = \frac{\delta l}{\bar{l}} \tag{7.9}$$

Converting to noise spectral density results in

$$\frac{S_I(f)}{\left(\bar{I}\right)^2} = \frac{S_\mu(f)}{\left(\bar{\mu}\right)^2} = \frac{S_l(f)}{\left(\bar{l}\right)^2} = \frac{\alpha_H}{f\bar{N}} \tag{7.10}$$

where α_H is an adjustable parameter and all other variables are as previously defined. And second, by viewing the inverse proportionality of the free path length with the scattering cross section, σ, perturbations in l result in perturbations in σ, which means perturbations in μ.

$$\frac{\delta\mu}{\bar{\mu}} = -\frac{\delta\sigma}{\sigma} \tag{7.11}$$

Converting to noise spectral density results in

$$\frac{S_I(f)}{\left(\overline{I}\right)^2} = \frac{S_\mu(f)}{\left(\overline{\mu}\right)^2} = \frac{S_\sigma(f)}{\left(\overline{\sigma}\right)^2} = \frac{\alpha_H}{f\overline{N}} \tag{7.12}$$

where α_H is an adjustable parameter. It now remains to apply the line of reasoning presented in van der Ziel to the QWIPs in this research.

As described above, a fundamental characteristic of *1/f*-like noise is its I^2 dependence. In addition, when this noise is presumed to be a manifestation of mobility fluctuations, if there is any DC current that does not contain a mobility term it stands to reason that it must be removed from the total current prior to analysis. The current noise spectral density is then plotted versus the relevant component of current to determine whether there is a squared dependence.

As discussed in chapter 4 of this work, current in these devices contain two components, thermionic emission and tunneling. Recall that tunneling current is represented by

$$I_{tun} = CV_p^2 \exp\left(\frac{-B}{V_p}\right) \tag{7.13}$$

with

$$B = \frac{4}{3}\frac{\sqrt{2m^*}}{q\hbar} L_b \phi_t^{3/2} \tag{7.14}$$

and notice that there is no dependence of the current on mobility. This precludes any contribution by this current component to mobility fluctuation noise.

In contrast, thermionic emission current has an explicit dependence on both electron density and electron mobility. Thermionic emission current in an n-type semiconductor is represented by

$$I_{TE} = q\mu_n n\mathscr{E} A \tag{7.15}$$

where q is the magnitude of the electric charge, μ_n is the mobility of continuum electrons, n is the density of mobile electrons, $\mathscr{E}$ is the electric field, and A is the device area. For a given bias, assuming mobility fluctuations dominate, then a change in current is generated by a change in mobility or

$$\Delta I_{TE} = \left(qn\mathscr{E} A\right)\Delta\mu_n \tag{7.16}$$

where the capital delta, Δ, denotes a change in the quantity. Translating this into noise spectral density results in

$$S_I = \left(qn\mathscr{E} A\right)^2 S_\mu \tag{7.17}$$

The quantity inside the parenthesis is the thermionic emission current divided by the mobility. Algebraic manipulation results in

$$\mathrm{S_I} = \left(I_{TE}^2\right)\frac{S_\mu}{\mu^2} \tag{7.18}$$

and substituting for the fraction on the right hand side results in

$$S_I = \left(I_{TE}^2\right)\frac{\alpha_H}{fN} \tag{7.19}$$

with all variables previously defined. Equation (7.19) explicitly shows the expected I^2 dependence with the current restricted to only the thermionic emission component.

Using the properties of logarithms and the equation for a line, $y = mx + b$, equation (7.19) becomes

$$\ln\left(S_I\right) = 2\cdot\ln\left(I_{TE}\right) + \ln\left(\frac{\alpha_H}{fN\left(T\right)}\right) \tag{7.20}$$

which results in

$$m = 2 \text{ and } b = \ln\left(\frac{\alpha_H}{fN(T)}\right) \tag{7.21}$$

where m is the slope of the line and b is the y-axis intercept. In addition, α_H and f are temperature independent but N is a strong function of temperature, T. The temperature dependence is exponential,

$$N(T) = N_0 \exp\left(-\frac{E_{act}}{k_b T}\right) \tag{7.22}$$

where N_0 is the number of electrons available for activation from a single well, E_{act} is the activation energy, k_b is Boltzmann's constant, and T is temperature in Kelvin. Making the substitution into the equation for b results in

$$b = \ln\left(\frac{\alpha_H}{fN_0}\right) + \frac{E_{act}}{k_b T} \tag{7.23}$$

with all variables as defined previously.

The value for b is determined by first plotting the current noise spectral density for a single period versus the thermionic emission current, at a particular frequency and temperature with both axes logarithmic, then finding the y-axis intercept for a line of slope two that best fits the data. Grouping these intercepts by frequency, they are then plotted versus 1000/T. Finally the slope and y-axis intercept of the resulting line, found in the least squares sense, are used to determine the activation energy and the Hooge parameter for each device.

An additional figure of merit used for devices with flicker noise is the corner frequency. The corner frequency is defined by where the flicker noise and the diffusion noise intersect. To predict the corner frequencies for these devices, the GR model

equation defined for the drift regime of operation is equated with the flicker noise equation and solved for frequency.

The relevant equations are

$$M \cdot S_{i,1/f} = \frac{\alpha_H I_{TE}^2}{f_c N(T)} \tag{7.24}$$

where M is the number of periods and f_c is the corner frequency and

$$S_{i,drift} = \frac{4I_d^2}{\overline{G}} \tag{7.25}$$

where all other variables are as previously defined. Recall that multiplying the current noise spectral density by the number of barriers results in a value that represents a single period of the device. Making appropriate substitutions and solving for f_c results in

$$f_c = \frac{\alpha_H I_{TE}^2 C}{4I_d^2 N_d} \tag{7.26}$$

with N_d the doping density in the quantum wells. Recall that the fitting parameter C is postulated to be single valued for a device. This was born out for D2 and not for D3. Under conditions that the dark current wholly consists of a thermionic emission component, equation (7.26) simplifies to

$$f_c = \frac{\alpha_H C}{4N_d} \tag{7.27}$$

with all variables previously defined.

Experimental Data

Device I

The low frequency noise of D1 has been evaluated separately than that of D2 and D3. This is because of the random telegraph signal noise observed during measurements. Refer to Chapter 8 of this work for details.

Device II

Given the above line of reasoning, and including only the bias points that exhibit a *1/f*-like frequency characteristic, double logarithmic plots of current noise spectral density versus thermionic emission current were generated at each of four frequencies per temperature. The frequencies are 25 Hz, 45 Hz, 79.375 Hz, and 141.25 Hz. The y-axis intercept, *b* in equation (7.21), is calculated then plotted at a given frequency versus 1000/T, Figure 69. For each plot there are two possible 'best fit' lines shown. This allows determination of the range of values able to be obtained from the four data points. The legends for these plots give values for the slope and the y-axis intercept, *y(0)*, which are used in determining the activation energy and the Hooge parameter.

The calculated values for each frequency and each line are given in Table 27. The values for this device may be represented by the mean of these values which would give an activation energy of 94.5 meV and a Hooge parameter of $9.66 \cdot 10^{-9}$ for the solid (red) line and an activation energy of 77.8 meV and a Hooge parameter of $8.89 \cdot 10^{-8}$ for the dashed (black) line.

To see if the result is realistic the energy picture must be revisited. Recall that this is the simplest device with a single kind of well and a single kind of barrier. Material parameters dictate the energy distance from the conduction band edge of the barrier to the

conduction band edge of the quantum well. That distance in D2 is calculated as 193 meV. Using the results of simulation, the ground state energy in the quantum well is about 75.7 meV above the conduction band edge of the quantum well. Therefore, at equilibrium the activation energy is estimated to be 117.3 meV. Assuming a constant electric field, the range of electric field applied to D2 fell between $3.6 \cdot 10^3$ V/m and $2.4 \cdot 10^6$ V/m. This results in a range of Schottky type barrier lowering between 0.6 meV and 16.5 meV. The predicted tunneling barrier height is not included since the activation energy is calculated without the inclusion of tunneling current. This results in a predicted activation energy in the range between 100.8 meV and 116.7 meV. Taking into account that the latter values are a rough estimate, the extracted results are reasonable. Using the mean value of each α_H and substituting into equation (7.19), the number of mobile electrons, N, per period are calculated. The results give a range of values for all temperatures and biases between approximately 200 and 20,000 for the red (solid) line and between approximately 2000 and 200,000 for the black (dashed) line. Using only the thermionic emission current to calculate the DC resistance of the device, then calculating the electron mobility results in a range between approximately 550 and 4000 cm^2/Vs for the red (solid) line and between approximately 60 and 450 cm^2/Vs for the black (dashed) line. Neither set of numbers can be definitively argued as invalid. Therefore neither activation energy and Hooge parameter pair can be definitively argued as valid. At this point all that can be said is that the range of values obtained are reasonable.

The outcome of the corner frequency calculations are depicted graphically in Figure 70 for the red (solid) line and in Figure 71 for the black (dashed) line. Each graph depicts the corner frequencies obtained from the data and from equation (7.26) at a single

temperature. In Figure 70, the predicted values are within about an order of magnitude of the data at each temperature. In addition, increasing temperature seems to bring about an increase in corner frequency. In Figure 71, the predicted values consistently overestimate the data by anywhere from one to two orders of magnitude.

Table 27 Calculated values of activation energy and Hooge parameter by frequency and fit for Device 2.

Frequency (Hz)	E_{act} (meV) (solid)	α_H (solid)	E_{act} (meV) (dashed)	α_H (dashed)
25	94.2	$7.83 \cdot 10^{-9}$	73.3	$1.24 \cdot 10^{-7}$
45	90.5	$1.47 \cdot 10^{-8}$	75.0	$1.13 \cdot 10^{-7}$
79.375	97.2	$6.68 \cdot 10^{-9}$	81.0	$5.65 \cdot 10^{-8}$
141.25	96.1	$9.46 \cdot 10^{-9}$	81.9	$6.20 \cdot 10^{-8}$

Device III

Following the same analysis technique as for D2, the plots of the intercepts versus 1000/T are found in Figure 72. Data for the same four frequencies are plotted. The legends for each of these plots contain the same information as described above. Table 28 contains a summary of the resulting calculations. The mean activation energy calculated from the red (solid) line is 219.9 meV and from the black (dashed) line is 141.2 meV. The mean Hooge parameter calculated from the red (solid) line is $2.27 \cdot 10^{-12}$ and from the black (dashed) line is $1.22 \cdot 10^{-8}$.

Evaluating the calculated activation energy for this device is not as straight forward as it was for D2 since the energy band configuration is more complex. Assuming that the 20 Å barriers are effectively transparent to the mobile electrons simplifies the energy picture enough that the evaluation is tractable. In addition, the effects of Schottky type barrier lowering become negligible before 20 Å is reached, so do not need to be accounted for in this device. What remains is the tunneling barrier height and any band bending effects due to bias. Figure 73 is a stylized drawing of D3 at equilibrium with the

20 Å barriers removed. Notice that the calculated activation energy from the red (solid) line falls between the two effective barrier heights when measured from the ground state energy with no correction for tunneling barrier height. This is reasonable since the energy picture has been simplified and the tunneling current is not part of the activation energy calculation. However, the calculated activation energy from the black (dashed) line is about 72 meV below the lowest barrier as seen in Figure 73. There appears to be a significant deviation in the results obtained from the two 'best fit' lines.

Table 28 Calculated values of activation energy and Hooge parameter by frequency for Device 3.

Frequency (Hz)	E_{act} (meV) (solid)	α_H (solid)	E_{act} (meV) (dashed)	α_H (dashed)
25	220.3	$2.12 \cdot 10^{-12}$	149.7	$3.94 \cdot 10^{-9}$
45	219.9	$2.27 \cdot 10^{-12}$	143.3	$7.99 \cdot 10^{-9}$
79.375	221.2	$2.05 \cdot 10^{-12}$	138.2	$1.44 \cdot 10^{-8}$
141.25	218.4	$2.64 \cdot 10^{-12}$	133.6	$2.23 \cdot 10^{-8}$

Using each mean Hooge parameter in equation (7.19) and solving for *N* results in a range of mobile electrons per period for all temperatures and biases of about 10^{-4} to 1 for the red (solid) line and about 1 to 6500 for the black (dashed) line. Even multiplying by the number of periods the former results are suspect. This would lead to the conclusion that the 'best fit' depicted by the red (solid) line is actually outside the range of possibility provided the model used is applicable to the operating conditions of this device. Turning to the latter result and again using solely the thermionic emission current to determine the DC resistance, the electron mobility is calculated as between about 220 and 22,000 cm^2/Vs.

The outcome of the corner frequency calculations are given graphically in Figure 74 for the red (solid) line and in Figure 75 for the black (dashed)line. They were obtained in the same manner as done for D2 except that since the fitting parameter, *C*,

was shown to have a strong temperature dependence for this device, a different value was used at each temperature.

With the exception of at 81.61 K, the corner frequency predicted by equation (7.26) using the red (solid) line values consistently under estimates the data. At 81.61 K the two sets of values cross in the vicinity of 1 mA bias, with the prediction greater than the data below and less than the data above. Using the black (dashed) line values results in vastly overestimating the corner frequency, in some places by as much as four orders of magnitude. This is similar to what was seen for D2.

Discussion

Published Hooge parameter values were sought as a check on those calculated in this study. Several researchers have been working in similar compound semiconductor material systems as those used for these QWIPs. Unfortunately, there are not enough similarities to comfortably allow comparisons that could definitively confirm or refute the validity of the values calculated in this study. Hooge and Tacano [30] looked at homogeneous n-type GaAs. While the QWIPs under study have degenerately doped n-type GaAs contacts the noise is believed to be generated in the barriers. The barriers are AlGaAs with a small percentage of Al but are not doped, and the wells are n-type InGaAs with a small percentage of In. Tacano, Tanoue, and Sugiyama [31] obtained data for InP, GaAs, and InGaAs heterostructures.

Data from papers presented at the 15th International Conference on Noise in Physical Systems and *1/f* Fluctuations in 1999 are also from similar material systems but are arguably not comparable. Specifically, Tacano et al. [32] look at InAs channels, Sugiyama et al. [33] look at InGaAs quantum wires, and Berntgen et al. [34] look at

InGaAs 2D electron gas quantum well channels. In any case, the Hooge parameters varied between 10^{-2} and 10^{-7}. The parameters extracted via this study are two to five orders of magnitude smaller than the lowest value reported. This may simply be that only the thermionic emission current was used for calculation in devices that show varying degrees of a combination of both tunneling and thermionic emission currents. Or it may indicate that the model needs to be adjusted due to the geometry of the devices.

.

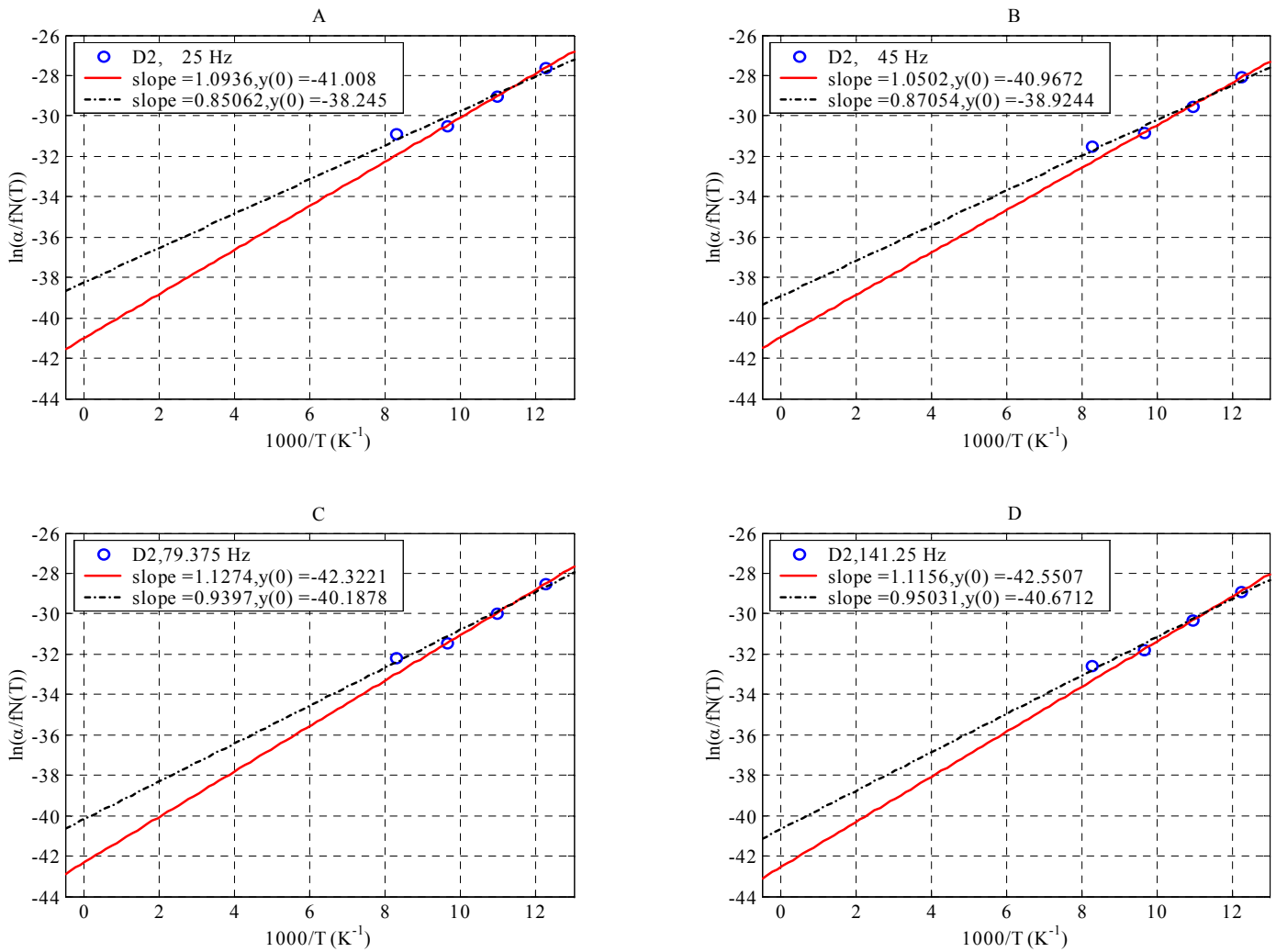

Figure 69 Graph of calculation results used to obtain α_H for Device 2 including two possible line fits. A) 25 Hz B) 45 Hz C) 79.375 Hz D) 141.25 Hz

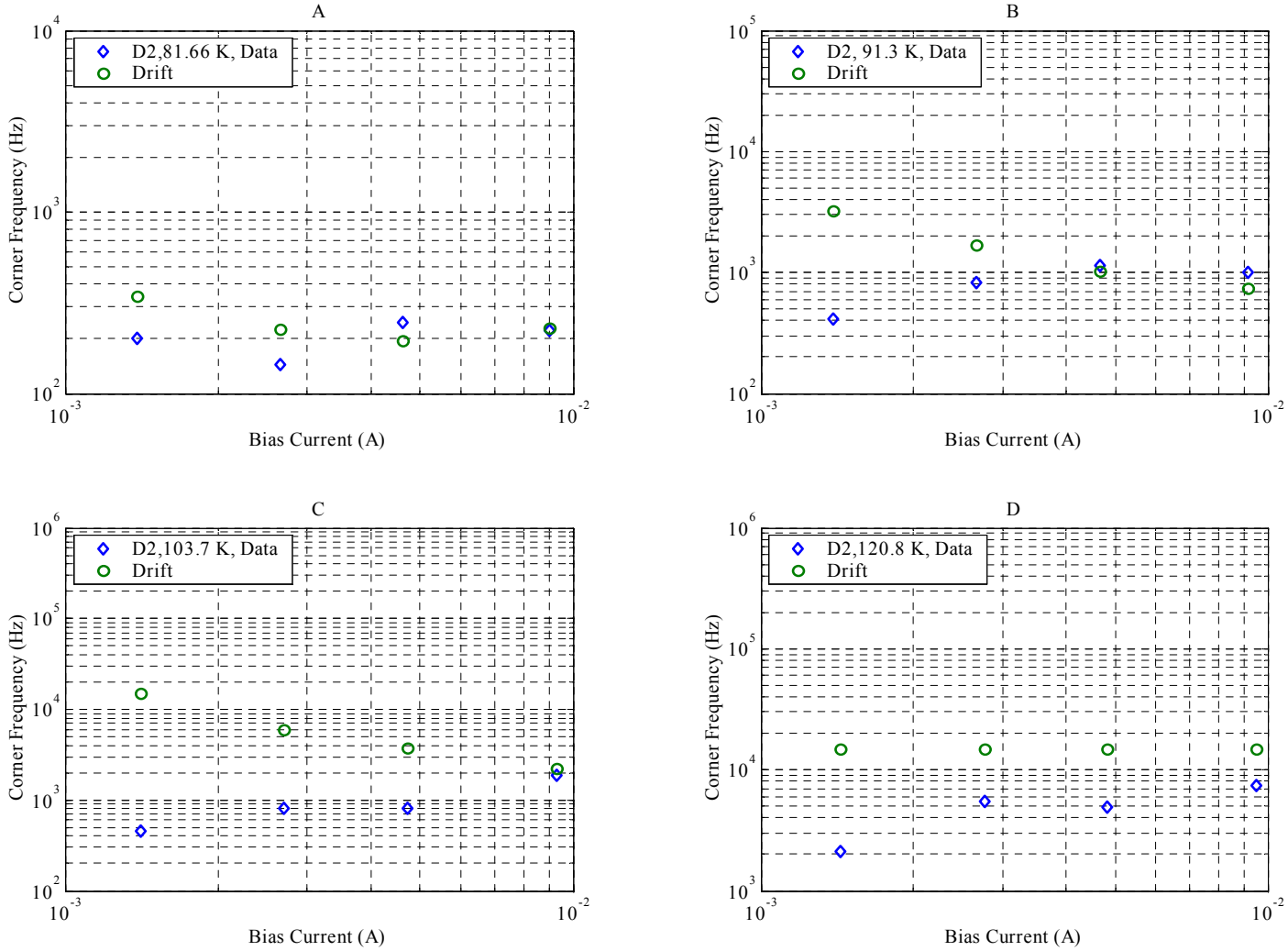

Figure 70 Corner frequencies obtained from data and the drift equation for Device 2 (solid line). A)81.66 K B) 91.3 K C) 103.7 K D) 120.8 K

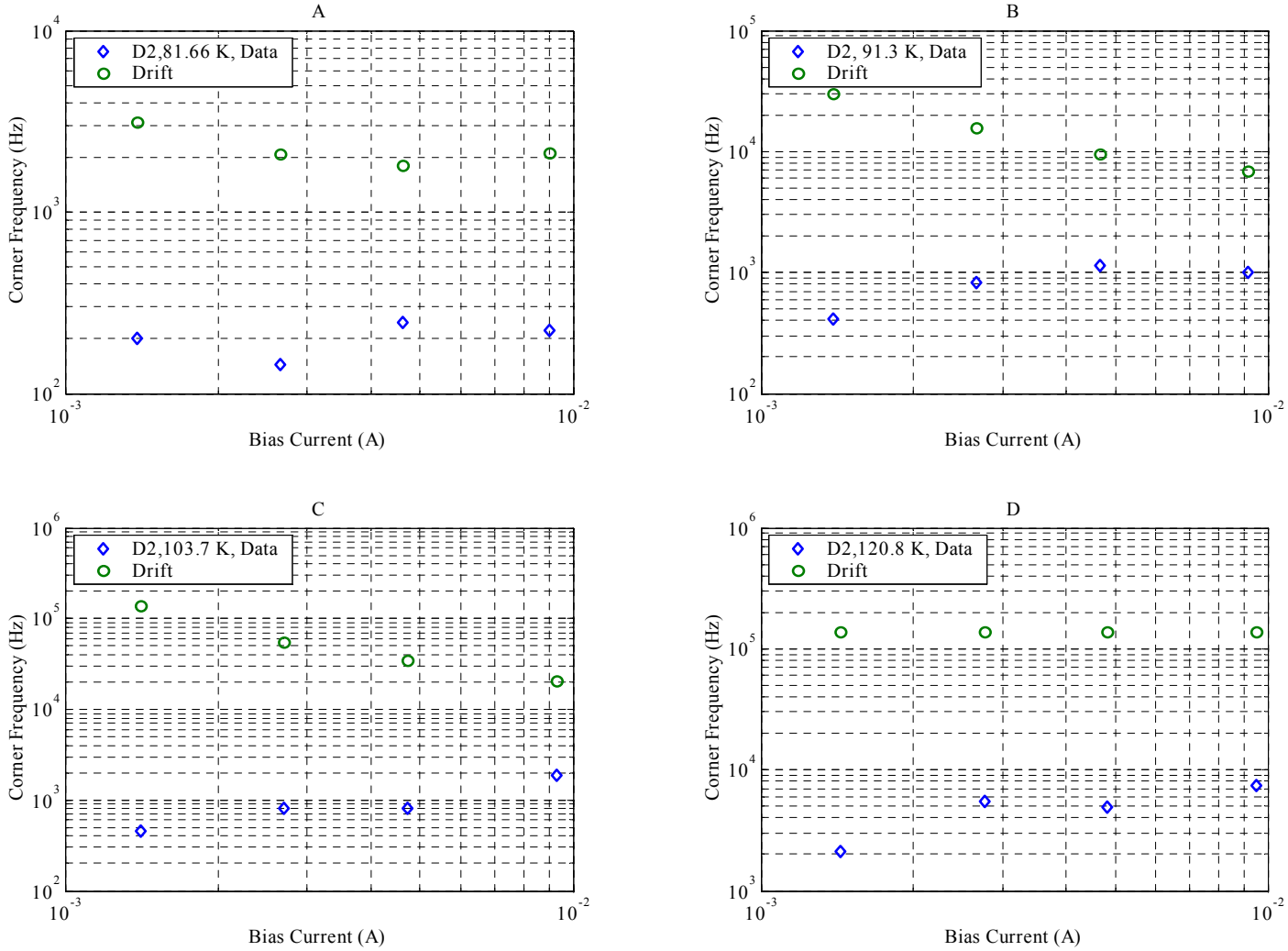

Figure 71 Corner frequencies obtained from data and the drift equation for Device 2 (dashed line). A)81.66 K B) 91.3 K C) 103.7 K D) 120.8 K

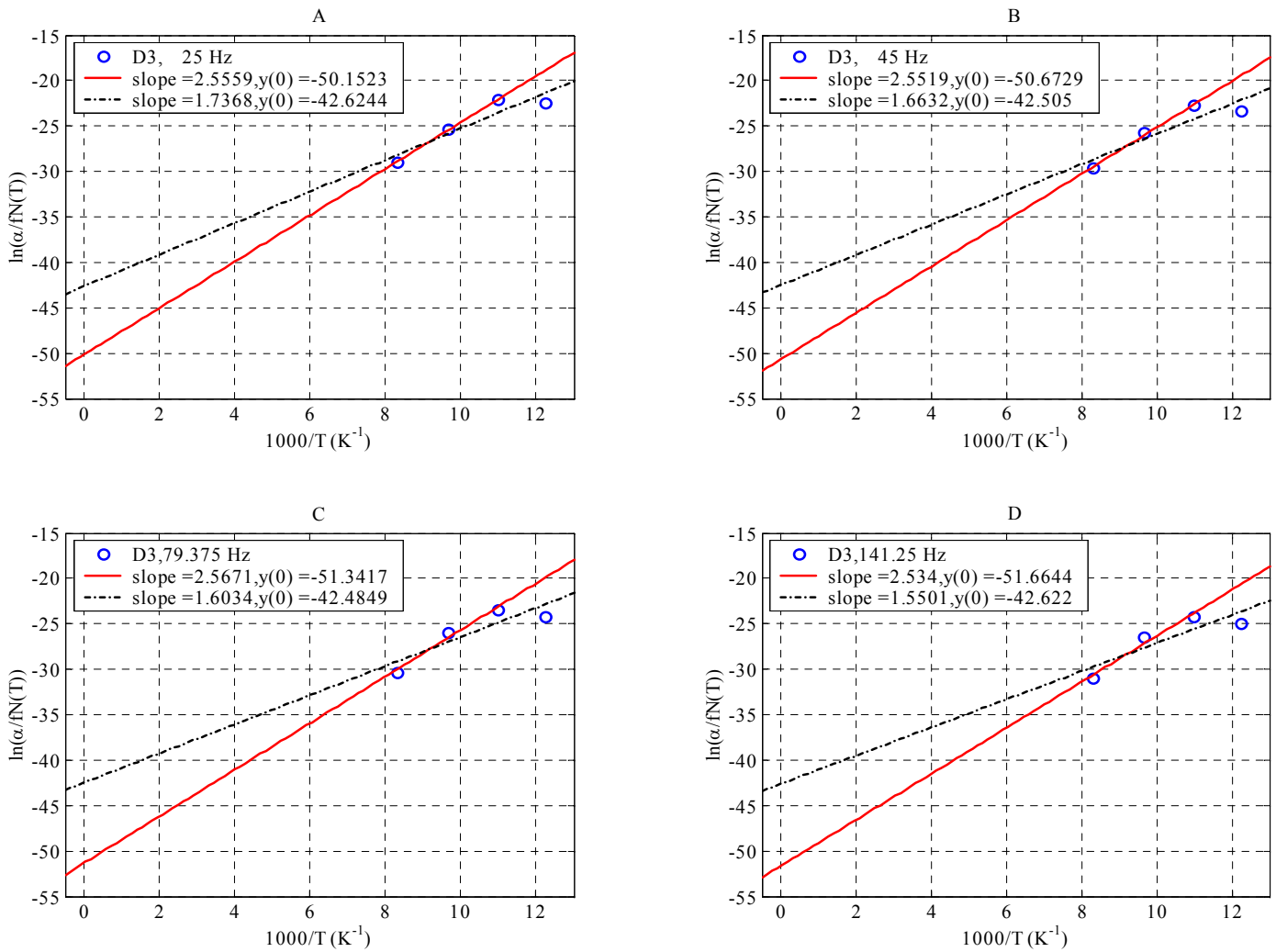

Figure 72 Graph of calculation results used to obtain α_H for Device 3 including two possible line fits. A) 25 Hz B) 45 Hz C) 79.375 Hz D) 141.25 Hz

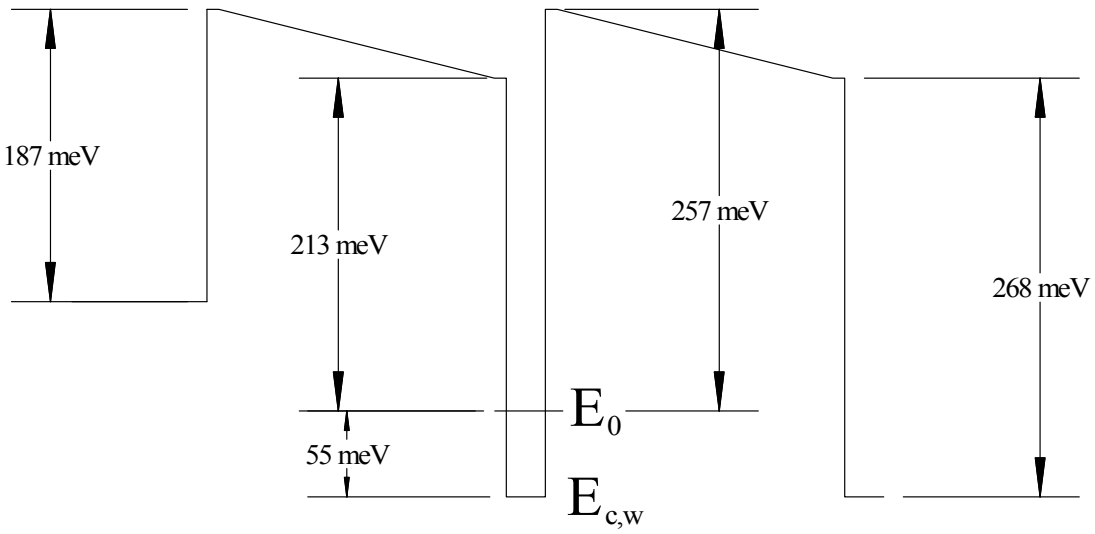

Figure 73 Relevant energy distances for Device 3, assuming that the 20 Å barriers are transparent.

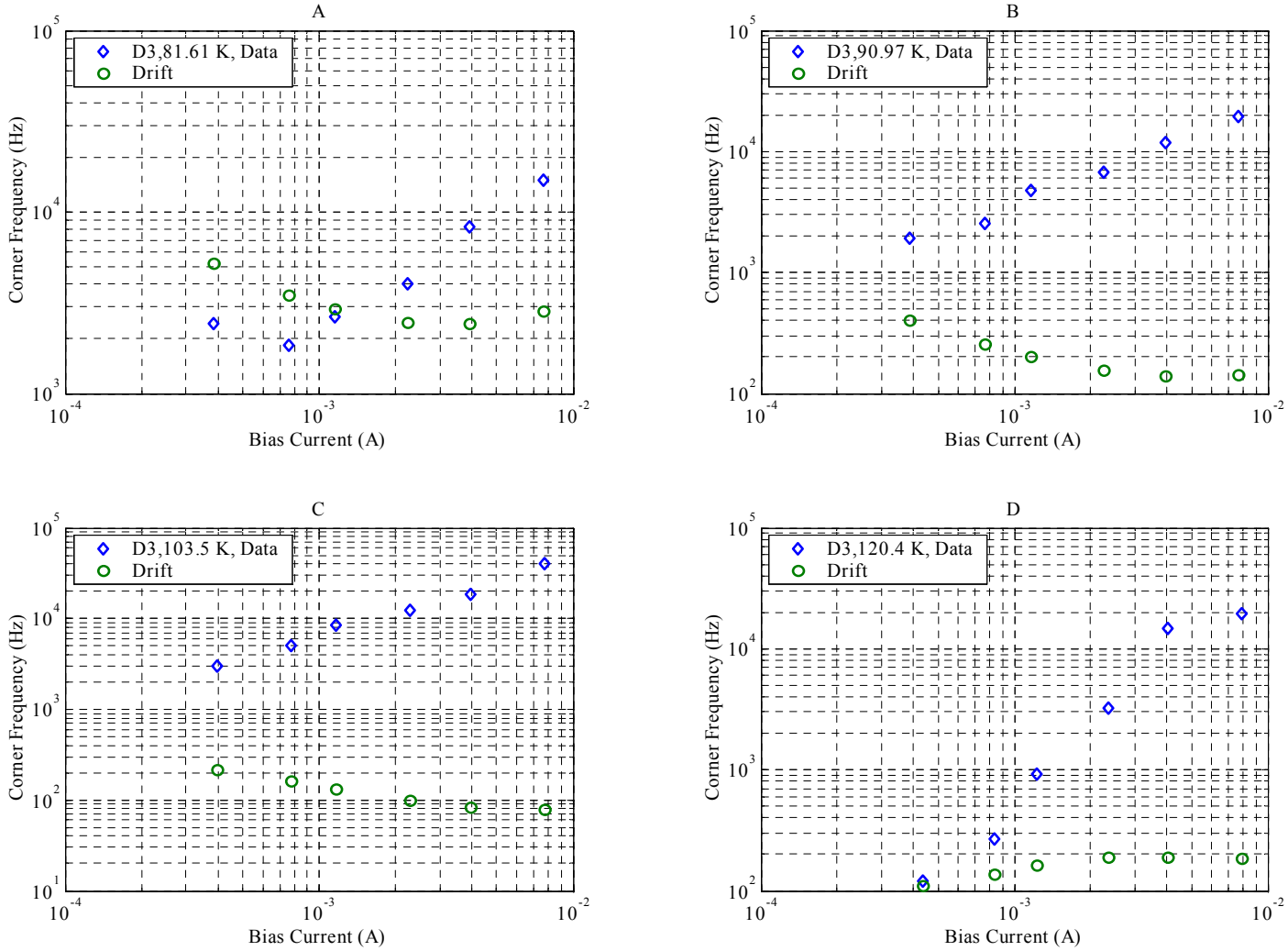

Figure 74 Corner frequencies obtained from data and the drift equation for Device 3 (solid line). A)81.61 K B) 90.97 K C) 103.5 K D) 120.4 K

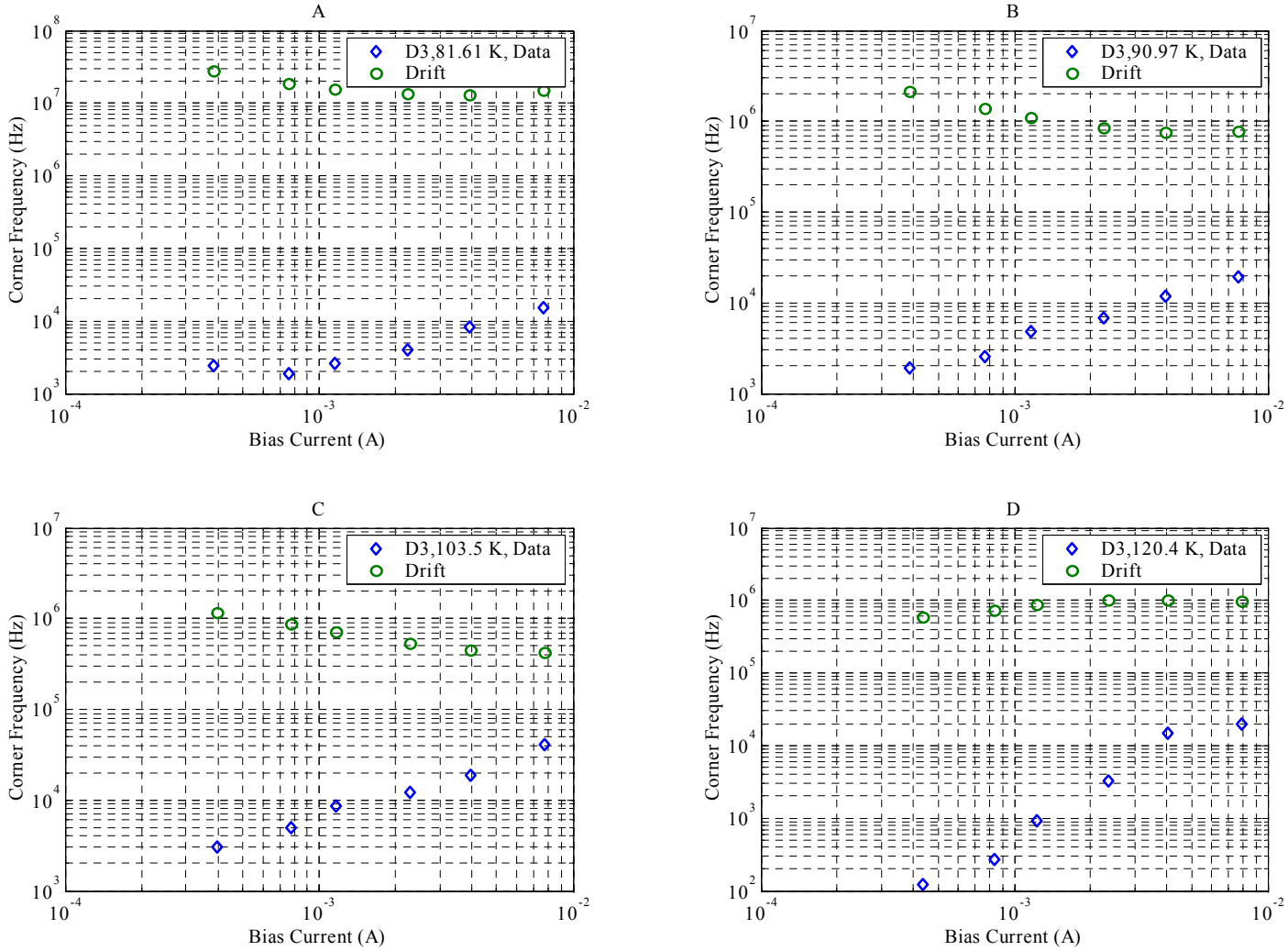

Figure 75 Corner frequencies obtained from data and the drift equation for Device 3 (dashed line). A)81.61 K B) 90.97 K C) 103.5 K D) 120.4 K

CHAPTER 8
RANDOM TELEGRAPH SIGNAL NOISE

Given the possibility that the performance of a device will be limited by noise, it becomes important to study all noise sources in order to better optimize a device and gain understanding of how the device works. Therefore, this chapter will discuss how to determine charge transport and defect characteristics from the noise phenomenon known as random telegraph signal (RTS). Only Device I was analyzed in this manner since it was the only one of the three devices that exhibited clear RTS.

RTS manifests in the time domain as pulses of various duration and, in this case, various heights [35]. In the setup used the device was current biased so the RTS showed up as a change in voltage. Typical time domain data are shown in Figure 76. Since the device shows Ohm's law behavior in the bias ranges tested, a change in voltage occurs due to a change in resistance.

$$\Delta V_x = \overline{I} \cdot \Delta R_x \tag{8.1}$$

where Δ denotes a change in a quantity, V_x is voltage, $\overline{I}$ is average current, and R_x is resistance.

The change in resistance is caused by a unit change in the number of electrons in the conduction band. It is observable due to the small numbers of carriers contributed locally by each well to the continuum states coupling the quantum wells.

Since the device was negatively current biased a negative voltage transition means an increase in magnitude. Resistance increased by means of a reduction of the number of

electrons in the conduction band. In other words, a negative voltage transition indicates the capture of an electron and a positive voltage transition indicates the emission of an electron. Therefore, the time width of a negative-going voltage pulse is the electron emission time, τ_e.

It is assumed that the distribution of emission times is Poisson-like [35]. This is confirmed by semi-logarithmic histogram analysis of emission time data parameterized by pulse height. In Figure 77, the bars represent measured data and the line is a best fit to the data using the following equation, where t is time, c is a constant, and τ_e is the pulse width or emission time [35].

$$\frac{\#\ \text{pulses}}{time} = \frac{c}{\tau_e}\exp\left(\frac{-t}{\tau_e}\right) \tag{8.2}$$

Plotting the emission times associated with each pulse height versus 1000/T enabled calculation of activation energies associated with traps most likely located in the barriers. There were two distinct pulse heights over the temperature range studied, and two corresponding distinct activation energies of 55.9 meV and 80.8 meV, Figure 78. The actual pulse heights increased with decreasing temperature. This is as expected since ΔV is inversely proportional to both number of carriers and electron mobility, which will be shown below.

Noise measurements on QWIP structures at low bias and for similar temperature ranges [36] have shown that the charge carriers, upon thermal excitation from the quantum wells, travel on average to the nearest neighboring quantum well where they subsequently recombine. This recombination process is triggered by carrier-impurity scattering in the doped well regions. As a result a low bias QWIP model is proposed

consisting of a series combination of well-barrier-well units. Each unit has a local resistance associated with it dictated in part by the local number of mobile carriers. The voltage pulses are attained by a unit change in number of carriers in one of these local resistances and are distinct due to the differences in barrier profiles.

In an ideal trap free device all carrier transitions between bound and continuum states would occur at the quantum wells. Since the wells are doped they can be treated as reservoirs of electrons and can be thought of as contacts feeding the barrier regions. At low temperatures the time the electrons spend in the wells is long compared to intra-well scattering times so that the electrons fully thermalize and lose any statistical information from their previous continuum state trajectory. This ensures that the well-barrier-well sections can be treated as statistically independent units. In our case, measured RTS events indicate that the device has localized defect centers in the barriers.

Since each well has a distinct bound-to-continuum energy difference the number of carriers contributed locally varies with well region. Thus the well-barrier-well regions are expected to have three distinctly different resistances and, by extension, ΔV's. Being in a linear mode of operation, the equation for the resistance of each well-barrier-well section is

$$R_x = \frac{L_b^2}{q \cdot \mu_n \cdot N_x} \tag{8.3}$$

where $x = a$, b, or c depending on the particular well region, q is magnitude of the electric charge, μ_n is the continuum state electron mobility, L_b is the barrier width, and N_x is the number of carriers in the conduction band section. The total DC resistance $\overline{R}$ is 20 times the sum of the three 'local' resistances.

$$\overline{R} = \frac{20 \cdot L_b^2}{q \cdot \mu_n} \cdot \left(\frac{1}{N_a} + \frac{1}{N_b} + \frac{1}{N_c} \right) \tag{8.4}$$

An RTS pulse is generated by capture and emission of a single electron. Thus an equation for each event can be constructed and solved for the voltage transition, ΔV.

Case I: N_x electrons are in the continuum of a particular well-barrier-well section, x.

$$V_I = \overline{I} \cdot \left(R_I + R_{bg} \right) \text{ where } R_I = \frac{L_b^2}{q \cdot \mu_n \cdot N_x}.$$

Case II: An electron is captured.

$$V_{II} = \overline{I} \cdot \left(R_{II} + R_{bg} \right) \quad \text{where } R_{II} = \frac{L_b^2}{q \cdot \mu_n \cdot \left(N_x - 1 \right)}$$

R_{bg} represents the resistance of the 59 other 'local' resistances not undergoing electron capture. The RTS voltage difference ΔV is given by

$$\Delta V_x = V_{II} - V_I = \frac{\overline{I} \cdot L_b^2}{q \cdot \mu_n \cdot \left(N_x^2 - N_x \right)} \tag{8.5}$$

There are now four equations, (8.4) and (8.5), (with $x = a$, b, or c), in four unknowns, μ_n, N_a, N_b, and N_c. Since there were only two distinct ΔV's, N_c was assumed to be the arithmetic mean of N_a and N_b. This approximation derives from the fact that all three wells are close in energy barrier height and doping so their contributions of mobile carriers will be similar. Using the known parameters and assuming position independent continuum state electron mobility, values were obtained for N_a, N_b, and μ_n via numerical analysis and are shown in Table 29.

The low numbers of carriers listed in Table 29 corroborate the RTS model of an electron being trapped in a particular section of the device causing a locally significant change in resistance while the other device sections operate near steady state condition.

The mobility values resulting from the RTS model analysis are of the same order of magnitude as that published for electrons in undoped bulk GaAs for the same temperature range [37]. This is not surprising since the Al mole fraction of the undoped barrier regions is only 7%.

Table 29 Mobility and average number of charge carriers.

T (K)	$\mu_n x10^5$ (cm^2/Vs)	N_a	N_b	N_c
132.3	3.97	3.29	2.32	2.81
130.0	3.67	3.41	2.34	2.88
127.7	3.47	3.46	2.35	2.91
125.4	3.31	3.43	2.32	2.87
123.1	2.79	3.73	2.46	3.10
120.8	2.63	3.72	2.38	3.05
118.4	2.23	3.82	2.55	3.18

Of note is the difference between the expected trend of mobility changes with temperature and the calculated mobility trend in the barriers. In polar optical phonon scattering limited bulk GaAs, the mobility decreases exponentially with increasing temperature [37]. The trend is opposite for the mobility calculated using RTS data. This can be attributed to the fact that electron transport through the 450-Å QWIP barriers is nearly ballistic at the temperatures investigated. As a result the initial kinetic energy of a nearly ballistic flight, following the release of an electron from a quantum well or defect center, in large part determines the average electron velocity and thus mobility. This initial energy will increase with temperature, resulting in an increase in overall mobility with temperature. Each activation energy is associated with the trapping and de-trapping of electrons in defect centers in the barrier regions. Note that the total number of electrically active defects is small since no overlapping RTS pulses are observed.

RTS was observed in the temperature range 115-133 K at low constant current bias. It consisted of pulses with two distinct heights and emission times. Activation energies

were calculated from the data that likely correspond to traps in the barrier regions of the device. A method was proposed by which the continuum state electron mobility and number of charge carriers could be derived from the time data.

The criterion for RTS coupling out to the contacts includes two conditions. One is that the overall number of carriers be small enough that the change in voltage be of observable magnitude. The second is that the number of electrically active traps is small so that trapping and de-trapping events do not overlap in time.

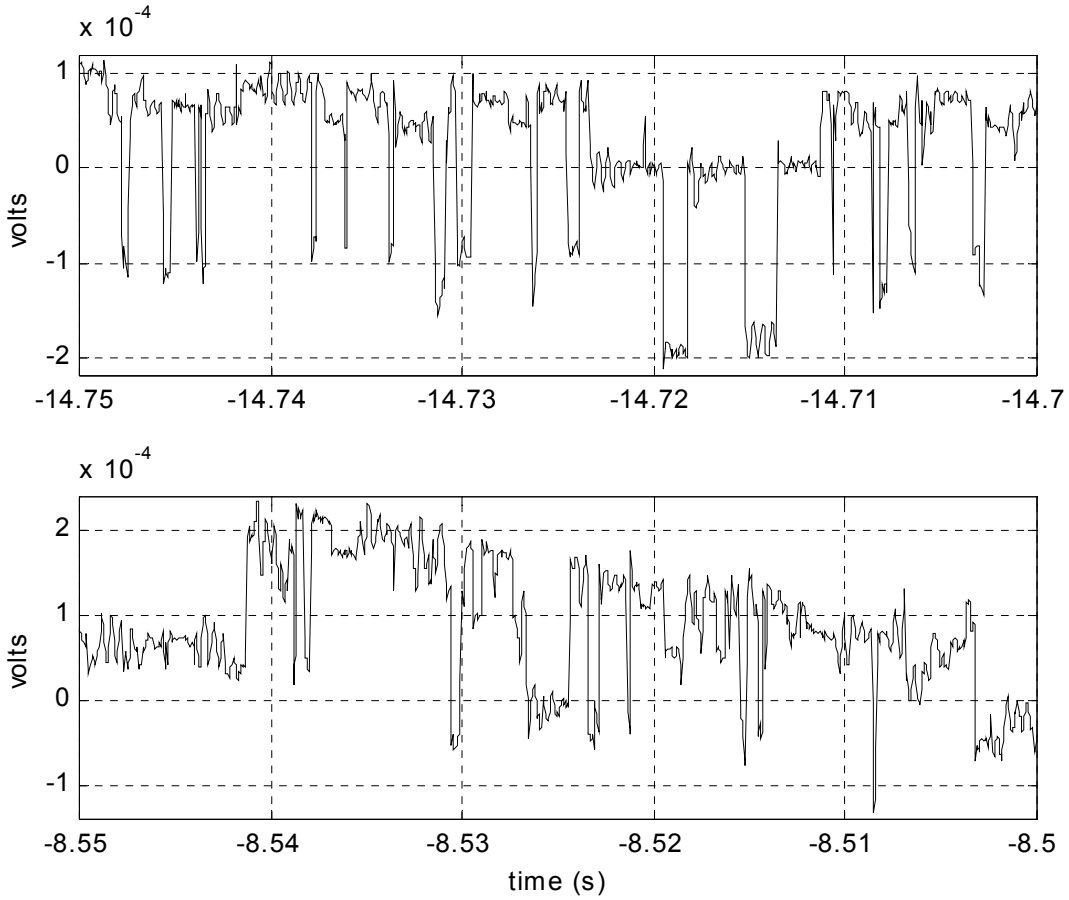

Figure 76 Two 50 ms segments of Device 1 output at low bias and 132.3 K.

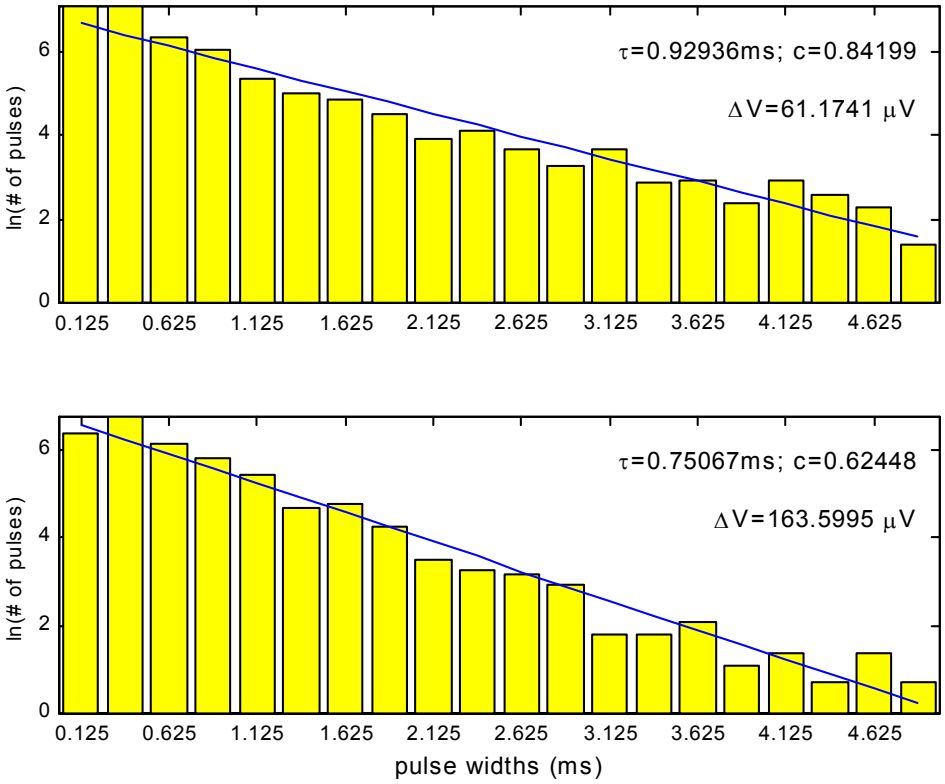

Figure 77 Histogram of τ_e data for two pulse heights at 130.0 K. The *x*-axis represents pulse widths. Each number is the center of a bin 250 μs wide.

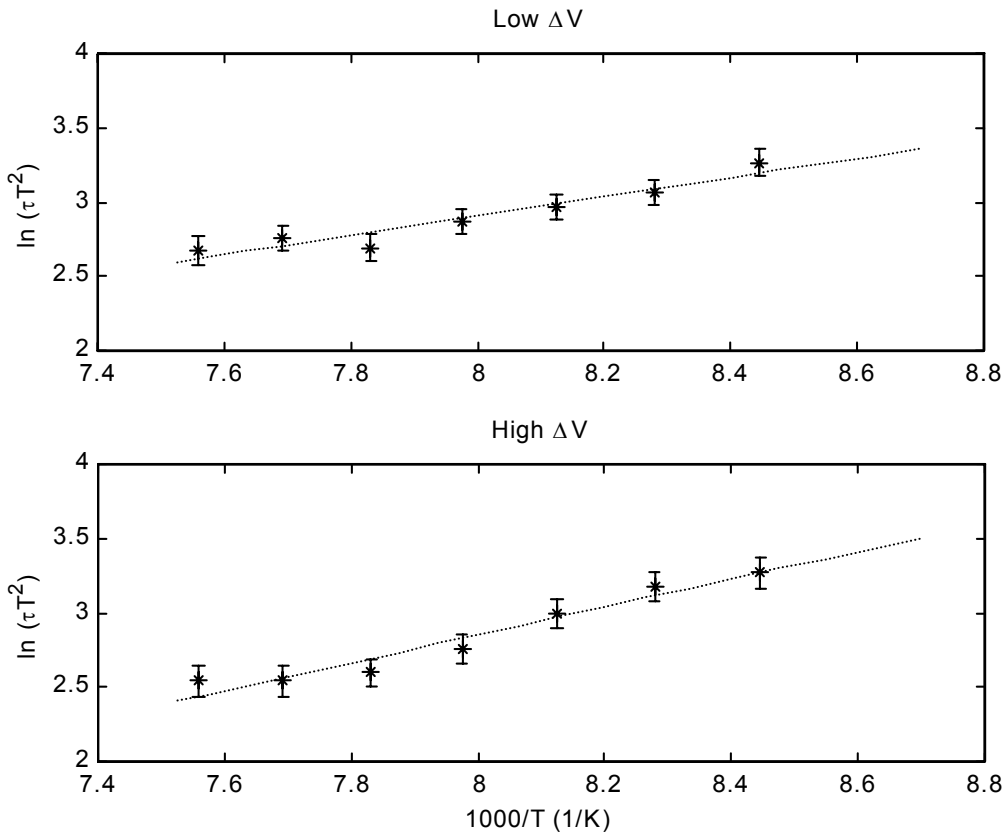

Figure 78 Activation energies are determined by the slopes of these $ln(\tau T^2)$ versus *1000/T* plots. Error bars represent a 70% confidence interval for the least squares fit dashed line.

CHAPTER 9
CONCLUSION

Each of three devices were submitted to an array of measurements under various controlled conditions. The measurements included IV characteristic, noise spectral density, and time domain waveforms. The controlled conditions encompassed temperature and bias. The goal was to begin to uncover the inner workings of QWIPs to the extent that it would be possible to accurately predict key operational parameters from a knowledge of the material system and device morphology. In addition, a deeper understanding of the physics may enable optimization such that high temperature operation would be realizable.

To that end, existing models for IV characteristics and noise in QWIPs were applied to these devices. This does not constitute duplication since the QWIPs in this study have distinctly different morphologies than those from which the models were obtained.

IV Characteristic

Each device demonstrated at least one regime of operation that was accurately predicted by either the thermionic emission model or the Fowler-Nordheim tunneling model. For Device 1 there is a region of bias where these models overestimate the measured current. Perusal of the energy band diagram under bias reveals that conditions exist whereby fewer electrons than predicted are able to contribute to current. This is due to the fact that neither model makes allowances for an asymmetric energy configuration of the type seen in Device 1.

In the case of Device 2 an accurate prediction through the entire bias range studied could only be obtained by the sum of the currents developed by each mechanism. This result leads to speculation that both mechanisms are present but only dominate at either end of the bias range. This not unreasonable since this device is the least complicated of the three and has the closest configuration to devices used to obtain the models. In Device 3 however, there is a wide bias region for which neither mechanism is predictive nor is the sum of the two mechanisms. In this case the current is underestimated. Again a look at the energy band configuration is instructive. One possibility is the quasi-confined states formed in the barrier region which may provide a resonant tunneling path. Another possibility is that the four excited states that are there by design may require explicit inclusion into any IV model that would afford accurate prediction.

Noise

In general it appears that simple morphology equates with low noise. This makes intuitive sense. The fewer materials, layers, periods, etc. the fewer sites expected to generate adverse signal. There is a point of diminishing returns, however. The beauty of QWIPs is their diversity. That diversity comes at the price of unexpected and uninvited noise behavior. Or does it.

Device 1 targets three infrared wavelengths. This allows detection of a much broader spectrum with a single device, a potentially money saving configuration. The increased complexity required to obtain that performance is expected to produce a noisier device. Using the dark current as a measure of the expected noise, models would predict a higher current than measured which correlates with a prediction of more noise. Therefore, in the region of bias that the current is overestimated the noise is below that expected, resulting in better detectivity.

The point is that the correlation between noise behavior and simplicity is neither straightforward nor simple. This work reinforces that point as well as providing some clues as to modeling of noise behavior in QWIPs.

Thermal Noise

As mentioned previously, all devices have thermal noise. Whether and to what extent this affects overall device behavior depends on temperature and what other noise mechanisms are active. Of the three devices studied only Device 2 reached the thermal noise floor within the biases and temperatures measured. This is valuable since the lack of high frequency excess noise provides a baseline. It also reinforces the idea that complexity is not the sole dictator of noise behavior.

Generation-Recombination Noise

Generation-recombination events may become evident primarily in two ways. At frequencies more than a decade below the inverse of its time constant, evidence of GR events is seen by excess noise independent of frequency. In other words it significantly adds to the thermal noise. If the inverse of the time constant is within the frequency range measured, then GR events are evidenced by a Lorentzian frequency spectrum in which the corner frequency is the inverse of the relevant time constant. In any event, noise measurements covering a variety of temperatures and biases will contain information regarding the cause of the GR events.

In Device 1 the frequency range measured was inadequate for discerning the presence or absence of high frequency GR noise. At low frequencies there was no spectral evidence of GR noise, i.e., no obvious Lorentzian frequency spectrum. Therefore another model was pursued.

For Device 2 there was excess noise at high frequencies that was independent of frequency, primarily for high biases. Using the foundation of analysis from previous work, the noise was able to be predicted within a close margin. As well, indications were that the bias and temperature range measured contained a transition region between two mechanisms of coupling the GR events to the external circuit. This could prove useful for optimizing the operating conditions.

In Device 3 the excess high frequency noise was also analyzed using the GR technique. For this device, the fitting parameter proved to be strongly temperature dependent which goes against the formulation of the model. However, including the derived temperature dependence resulted in a close fit to the data. Further study is required to determine whether this model can be modified or a new model is required.

Flicker Noise

The obscure causes of flicker noise provide latitude and restriction simultaneously. That it is seen in a myriad of physical systems, many outside the purview of semiconductor devices, speaks to the potential for myriad causes. It is therefore not surprising that several theories have been formulated with no definitive single solution. That being said, for this work some strongly defensible assumptions were made about the cause of the flicker noise observed in these devices with promising results.

The existence of strong random telegraph signal noise in Device 1 precluded analysis of the low frequency noise data from the perspective of flicker noise. For Device 2 the results of the analysis are encouraging. Using an extension of the mobility model for *1/f*-like noise, a reasonable Hooge parameter and activation energy were extracted. When compared with many devices the Hooge parameter obtained is quite small. However this can be explained by the inclusion of only the thermionic emission

current component rather than the total current. For Device 2 a weak effect was expected since the thermionic emission model provides good agreement with data through most of the temperatures and biases measured.

The exclusion of tunneling current had a larger impact on the Hooge parameter for Device 3. An expected result due to the strong presence of tunneling current, which is independent of mobility, and the presence of a current mechanism other than the two modeled, whose mobility dependence is unknown. The calculated activation energy is also reasonable when compared with results from simulations.

Comparison of the two Hooge parameters with those found in the literature results in the conclusion that these QWIPs are 'quiet' devices, at least from the perspective of mobility fluctuation noise. Interpretation of the corner frequencies extracted from the data is difficult without knowledge of the operating frequencies. For Device 2, low temperature operation results in a low corner frequency. Temperature increase results in an increase in the corner frequency by about two orders of magnitude. The trend is the opposite for Device 3 though at high bias there is little change across temperatures. In either device the range of corner frequencies varied from about 100 Hz to about 20 kHz.

Random Telegraph Signal Noise

Device 1 exhibited strong RTS noise, especially within a temperature range from 115 K to 135 K. Analysis resulted in extracting plausible transport parameters. Special conditions must be met in order to couple RTS to the external circuit. These conditions, primarily the low number of mobile electrons, are what allow the analysis.

At no temperature or bias did Device 2 exhibit RTS noise. For Device 3, there was some anomalous voltage pulses at some biases and temperatures but they could not be

clearly defined as RTS noise. Thus neither device could be analyzed in the same manner as Device 1.

Future Work

There are a number of avenues available to extend this work. Where the IV characteristic models were inadequate predictors further work is suggested regarding the effects of energy band relationships under bias. For example, it may be possible to quantify and model how the energy band configuration in Device 1 reduces the current at some biases. Also, the model inaccuracies seen in Device 3 may be incorporated by a more predictive model for all QWIPs or a model geared toward the particular energy band relationships seen there.

Another avenue may be determining a model or models that do not rely on the device being in a linear mode of operation. This could be accomplished by adding a component to the existing models that accounts for the non-linearity or by deriving a completely new model. Still in the noise realm, a deeper understanding of the fitting parameter used for the GR noise analysis could be pursued. It may be possible to obtain a model for the capture cross section that is able to be generalized. Or the temperature and/or bias dependence of the fitting parameter may be pursued to the same end.

In short, the use of noise measurements in QWIPs, as done in this work, is a viable route for further understanding of many aspects of device behavior and may be an avenue necessary for optimization.

LIST OF REFERENCES

[1] S. S. Li, "Recent progress in quantum well infrared photodetectors and focal plane arrays for IR imaging applications," *Materials Chemistry and Physics*, vol. 50, pp. 188-194, 1997.

[2] E. Rosencher, F. Luc, P. Bois, and S. Delaitre, "Injection mechanism at contacts in a quantum-well intersubband infrared detector," *Applied Physics Letters*, vol. 61, pp. 468-470, 1992.

[3] M. O. Manasreh, *Semiconductor Quantum Wells and Superlattices for Long-Wavelength Infrared Detectors*. Boston: Artech House, 1993.

[4] C. R. Pollock, *Fundamentals of Optoelectronics*. Chicago: Irwin, 1995.

[5] B. F. Levine, C. G. Bethea, G. Hasnain, J. Walker, and R. J. Malik, "High-detectivity D*=1.0 × 1010 cm /W GaAs/AlGaAs multiquantum well =8.3 μm infrared detector," *Applied Physics Letters*, vol. 53, pp. 296-298, 1988.

[6] M. A. Kinch and A. Yariv, "Performance limitations of GaAs/AlGaAs infrared superlattices," *Applied Physics Letters*, vol. 55, pp. 2093-2095, 1989.

[7] B. F. Levine, C. G. Bethea, G. Hasnain, V. O. Shen, E. Pelve, R. R. Abbott, and S. J. Hsieh, "High sensitivity low dark current 10 micron GaAs quantum well infrared photodetectors," *Applied Physics Letters*, vol. 56, pp. 951-853, 1990.

[8] S. R. Andrews and B. A. Miller, "Experimental and theoretical studies of the performance of quantum-well infrared photodetectors," *Journal of Applied Physics*, vol. 70, pp. 993-1003, 1991.

[9] K. K. Choi, C. Y. Lee, M. Z. Tidrow, W. H. Chang, and S. D. Gunapala, "Performance assessment of quantum well infrared photodetectors," *Applied Physics Letters*, vol. 65, pp. 1703-1705, 1994.

[10] K.-K. Choi, B. F. Levine, C. G. Bethea, J. Walker, and R. J. Malik, "Multiple quantum well 10 μm GaAs/AlxGa1 – xAs infrared detector with improved responsivity," *Applied Physics Letters*, vol. 50, pp. 1814-1816, 1987.

[11] E. Pelvé, F. Beltram, C. G. Bethea, B. F. Levine, V. O. Shen, S. J. Hsieh, and R. R. Abbott, "Analysis of the dark current in doped-well multiple quantum well AlGaAs infrared photodetectors," *Journal of Applied Physics*, vol. 66, pp. 5656-5658, 1989.

[12] K. Brennan and Y. Wang, "Analysis of the two-dimensional dark currents in quantum well devices," *Applied Physics Letters*, vol. 57, pp. 1337-1339, 1990.

[13] G. M. Williams, R. E. DeWames, C. W. Farley, and R. J. Anderson, "Excess tunnel currents in AlGaAs/GaAs multiple quantum well infrared detectors," *Applied Physics Letters*, vol. 60, pp. 1324-1326, 1992.

[14] H. C. Liu, A. G. Steele, M. Buchanan, and Z. R. Wasilewski, "Dark current in quantum well infrared photodetectors," *Journal of Applied Physics*, vol. 73, pp. 2029-2031, 1993.

[15] J. Chu, S. S. Li, and A. Singh, "Investigation of broad-band quantum-well infrared photodetectors for 8-14-mu m detection," *IEEE Journal of Quantum Electronics*, vol. 35, pp. 312-319, 1999.

[16] L. Jiang, S. S. Li, M. Z. Tidrow, W. R. Dyer, W. K. Liu, J. M. Fastenau, and T. R. Yurasits, "Three-stack, three-color quantum-well infrared photodetector for mid-, long-, and very long-wavelength infrared detection," *Applied Physics Letters*, vol. 79, pp. 2982-2984, 2001.

[17] M. S. Lundstrom, P. Dodd, M. Stettler, T. Herman, and B. Barrett, "Fish1D," , 1.0, 2.0, 2.1, 2.2, 2.3, 2.4 ed. West Lafayette, IN: Purdue Research Foundation, 1986.

[18] -. Ioffe Institute, "New Semiconductor Materials. Characteristics and Properties," . St. Petersburg, Russian Federation: Ioffe Physico-Technical Institute, 1998.

[19] O. Madelung, W. von der Osten, and U. Rossler, *Crystal and Solid State Physics: Semiconductors: Intrinsic Properties of Group IV Elements and III-V, II-VI and I-VII Compounds*, vol. Group III, Volume 22, Subvolume a. New York: Springer-Verlag.

[20] P. P. Silvester and R. L. Ferrari, *Finite Elements for Electrical Engineers*, 3rd ed: Cambridge University Press, 1996.

[21] S. Datta, *Quantum Phenomena*, vol. 8. Reading, Mass.: Addison-Wesley, 1989.

[22] M. A. Morrison, *Understanding Quantum Physics: A User's Manual*. Englewood Cliffs, NJ: Prentice Hall, 1990.

[23] A. van der Ziel, *Solid State Physical Electronics*, 3d ed. ed. Englewood Cliffs, N.J.: Prentice Hall, 1976.

[24] D. C. Wang, "Noise characterization and device modeling of quantum well infrared photodetectors.," in *Doctoral Dissertation for Electrical and Computer Engineering*. Gainesville, FL: University of Florida, 1996, pp. 119.

[25] C.-T. Sah, *Fundamentals of Solid State Electronics*. River Edge, NJ: World Scientific, 1991.

[26] A. van der Ziel, *Noise in Solid State Devices and Circuits*. New York: John Wiley & Sons, 1986.

[27] H. Nyquist, "Thermal Agitation of Electric Charge in Conductors," *Physical Review*, vol. 32, pp. 110-113, 1928.

[28] F. N. Hooge, "1/F Noise Is No Surface Effect," *Physics Letters A*, vol. A 29, pp. 139, 1969.

[29] F. M. Klaassen, "Characterization of Low 1/F Noise in Mos Transistors," *IEEETransactions On Electron Devices*, vol. ED18, pp. 887, 1971.

[30] F. N. Hooge and M. Tacano, "Experimental studies of 1/f noise in n-GaAs," *Physica B: Condensed Matter*, 1993.

[31] M. Tacano, H. Tanoue, and Y. Sugiyama, "Dependence of Hooge parameter of compound semiconductors on temperature," *Japanese Journal of Applied Physics, Part 2 (Letters)*, vol. 31, pp. L316-L319, 1992.

[32] M. Tacano, M. Ando, I. Shibasaki, S. Hashiguchi, J. Sikula, and T. Matsui, "Dependence of Hooge parameter of InAs heterostructure on temperature," presented at 15th International Conference on Noise in Physical Systems and 1/f Fluctuations, Hong Kong, 1999.

[33] Y. Sugiyama, T. Sugaya, S. Kim, T. Nakagawa, M. Ogura, and M. Tacano, "Fabrication of InGaAs quantum wires and their low frequency noise characteristics," presented at 15th International Conference on Noise in Physical Systems and 1/f Fluctuations, Hong Kong, 1999.

[34] J. Berntgen, A. Behres, J. Kluth, K. Heime, W. Daumann, U. Auer, and F.-J. Tegude, "Hooge parameter of InGaAs bulk material and InGaAs 2DEG quantum well structures lattice matched to InP," presented at 15th International Conference on Noise in Physical Systems and 1/f Fluctuations, Hong Kong, 1999.

[35] M. J. Kirton and M. J. Uren, "Noise in solid-state microstructures: A new perspective in individual defects, interface states and low-frequency (1/f) noise," *Advances in Physics*, vol. 38, pp. 367-468, 1989.

[36] D. C. Wang, G. Bosman, and S. S. Li, "Noise characterization and device parameter extraction of a p-type strained layer quantum-well infrared photodetector," *Journal of Applied Physics*, vol. 79, pp. 1486-1490, 1996.

[37] G. E. Stillman, C. M. Wolfe, and J. O. Dimmock, "Hall coefficient factor for polar mode scattering in n-type GaAs.," *Journal of Physics and Chemistry of Solids*, vol. 31, pp. 1199-1204, 1970.

BIOGRAPHICAL SKETCH

Lisa Kore began life in Denver, Colorado, in 1958. She traversed the country getting a B.S. in psychology at Heidelberg College (Ohio) in 1980, a B.S. in electrical engineering in 1995, and an M.S in electrical engineering in 1997. The latter two were both achieved at the University of Florida. She spent a few years in between, in South Dakota, working as an electronic technician in the U.S. Air Force. She has begun a teaching career at the University of North Florida during the completion of her doctoral work. She plans to continue as a professor with the hopes of returning to her native Colorado.